Vol. 2, No. 1, March 2026
jams.hsu.ac.ir

JOURNAL OF APPLIED MATERIAL SCIENCE

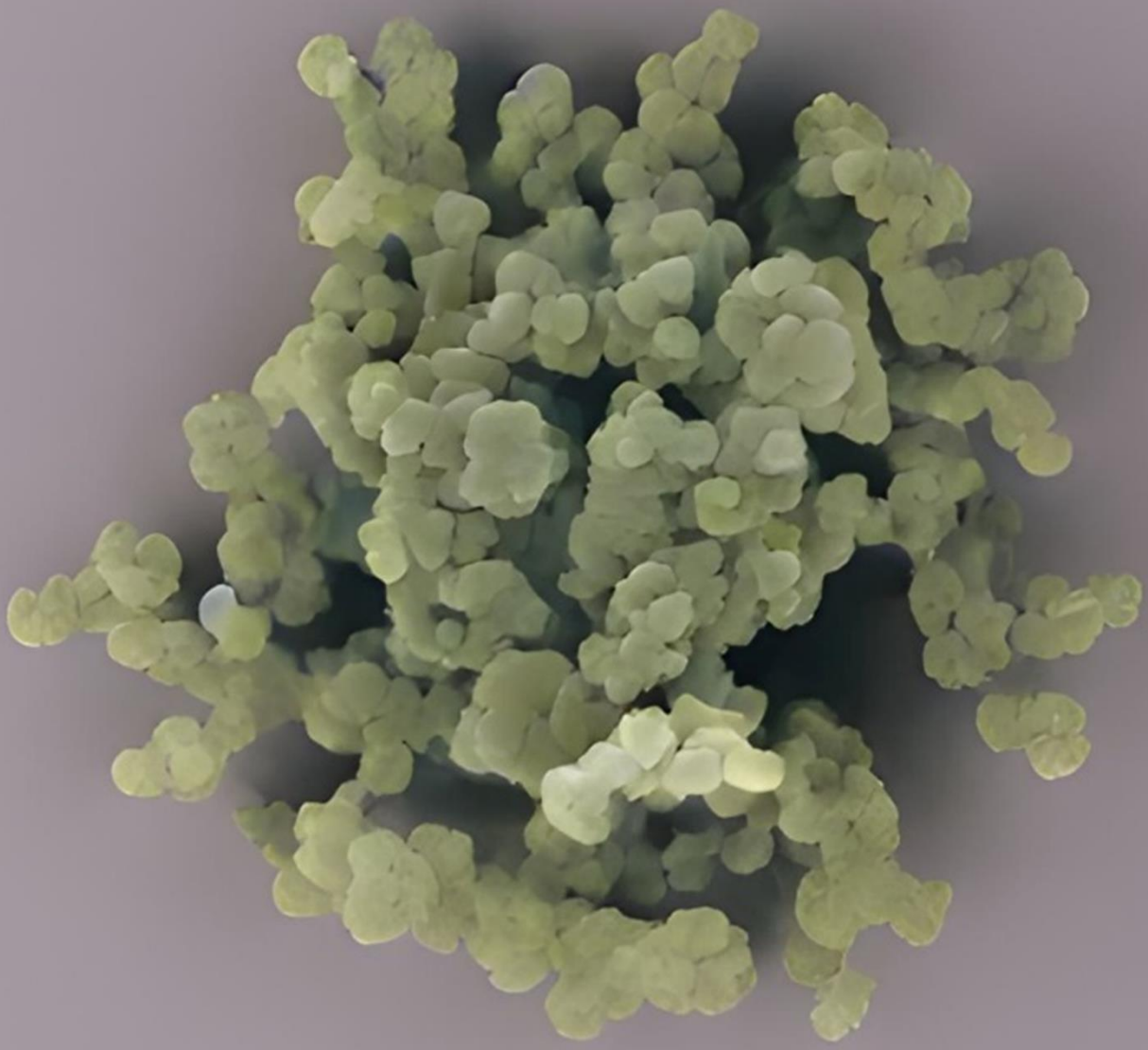

Hakim Sabzevari University

JOURNAL OF
APPLIED
MATERIAL
SCIENCE
jams.hsu.ac.ir

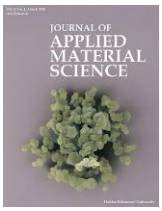

Contents

Volume 2, No. 1, March 2026

Editorial 260101

Aims and scope of the journal, a brief submission guideline, and the list of the editorial board.

Ahmad Allahbakhsh

doi: 10.22034/jams.2026.260101

Mechanical Characterization of Aluminum 6013-Red Mud Particulate Composites for Sustainable Structural Applications 260102

Chandrashekara et al. reinforced aluminum 6013 with red mud using liquid melt metallurgy. The results indicated that increasing the content of red mud improved various mechanical properties, including ultimate tensile strength, compressive strength, elongation, and hardness of aluminum 6013. These enhancements were attributed to factors such as particle distribution and grain refinement. The findings underscore the potential of red mud as a sustainable reinforcement material, promoting environmental sustainability in structural applications.

Chandrashekara K.N., Sreenivasa K., Krupakara Palur Venkataswamy Setty

doi: 10.22034/jams.2026.260102

Photoelectrochemical Hydrogen Generation from Seawater Using Modified g-C_3N_4/NiO Photo-electrode Heterojunction 260103

Bhattacharjee et al. studied the process of seawater splitting for hydrogen production using a nickel oxide (NiO)/iron-doped graphitic carbon nitride (Fe/g-C_3N_4/NiO) photoelectrode in combination with polyvinyl alcohol membranes, along with a molecular sensitizer. The proposed approach has the potential to promote sustainable green hydrogen production from seawater.

Jyoti Bhattacharjee, Preetam Datta, Abdul Aziz Shaikh, Akash Sathianarayanan, Milan Kumar Mandal, Subhasis Roy

doi: 10.22034/jams.2026.260103

© 2026 *J. Appl. Mater. Sci.* This material is licensed under a Creative Commons Attribution 4.0 International License.

Thermophysical Study of Chitosan-Starch-Glutaric Acid Film in Acetic Acid-Water Mixtures 260104

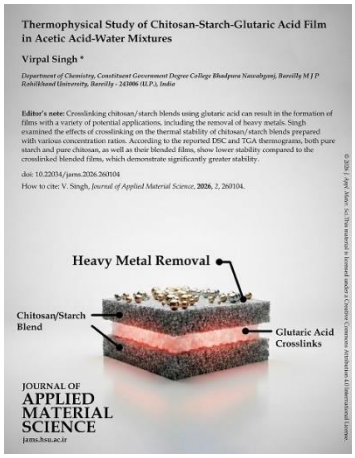

In this study, Singh examined the effects of crosslinking on the thermal stability of chitosan/starch blends prepared with various concentration ratios. According to the reported DSC and TGA thermograms, both pure starch and pure chitosan, as well as their blended films, show lower stability compared to the crosslinked blended films, which demonstrate significantly greater stability.

Virpal Singh

doi: 10.22034/jams.2026.260104

Photocatalytic Degradation of MB-Dye by CZTS Catalyst 260105

Illiyas and Preetha developed copper zinc tin sulfide (CZTS) thin films using the spin coating technique and assessed their photocatalytic activity with a solution of methylene blue (MB) dye. The study found apparent rate constants of 0.00562 min^{-1} for a 2 cm^2 catalyst and 0.00674 min^{-1} for a 4 cm^2 catalyst, with degradation rates of about 46% and 60% after 120 minutes, respectively. These results highlight that photocatalytic degradation efficiency is influenced by both the thin film's surface area and the irradiation time.

C.T. Illiyas, K.C. Preetha

doi: 10.22034/jams.2026.260105

Toxic and Growth Effects of Ag-TiO_2 Nanoparticles on *Etroplus suratensis* Fingerlings with Statistical Application 260106

Pandion et al. assessed the impact of dietary exposure to Ag-TiO_2 nanoparticles on the growth performance of *Etroplus suratensis* fingerlings. The findings demonstrate that Ag-TiO_2 nanoparticles exert concentration-dependent effects on these fish, with extended exposure to elevated concentrations adversely affecting growth and survival rates.

Kumar Pandion, Aarrthy M. Arunachalam, Archana Sharma, Kantha Deivi Arunachalam

doi: 10.22034/jams.2026.260106

© 2026 *J. Appl. Mater. Sci.* This material is licensed under a Creative Commons Attribution 4.0 International License.

Evaluation of Urease Activity Assessed on Urea Concentration Using Tannic Acid-Silver Nitrate Colorimetric Method **260107**

Imohiosen et al. explored how urea concentration affects urease activity using a colorimetric method with tannic acid and silver nitrate. Low concentrations limited enzyme activity, while an optimal concentration of 3.00 mM produced the highest absorbance, indicating maximum activity. Concentrations above 4.00 mM decreased absorbance, likely due to pH shifts. Low urea levels showed sharp SPR peaks at 414 nM, whereas higher levels produced broader peaks, suggesting substrate inhibition. These findings support the development of a sensitive urea biosensor.

Ojeaga Imohiosen, Adamu Makanta Salihu, Matthew Onyema Agu, Sanusi Abubakar

doi: 10.22034/jams.2026.260107

ABOUT COVER

Polymeric aerogels made from resins can serve as precursors for developing carbon aerogels, which have the potential to revolutionize porous materials for various advanced applications. The cover features a colored, processed SEM image of a novolac-derived carbon aerogel with a high level of microporosity and exceptionally low thermal conductivity.

(Note: The covers of this journal are created in part using artificial intelligence (AI) technologies, with direct human supervision. AI and AI-assisted technologies are permitted only for generating graphical abstract suggestions. If such technologies are used in the manuscript preparation, it must be clearly disclosed in the Acknowledgments section.)

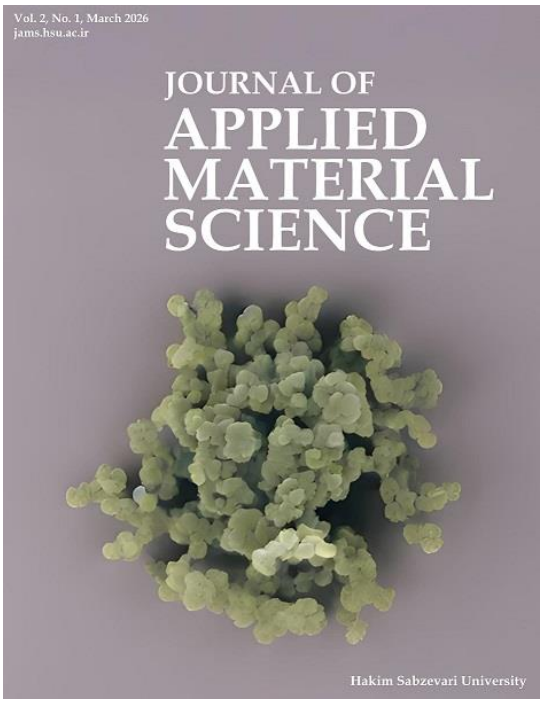

© 2026 *J. Appl. Mater. Sci.* This material is licensed under a Creative Commons Attribution 4.0 International License.

jams.hsu.ac.ir JOURNAL OF APPLIED MATERIAL SCIENCE

Journal of Applied Material Science:

One year of *open-access*, a platform to publish scientific developments in all aspects of material science under the *highest publication standards* and *the fastest peer-review process*

We began our journey on March 1st, 2025, and after a successful year of publication, we are excited to continue this path for the benefit of our authors and readers. The Journal of Applied Material Science publishes original research in the form of ***communications*** and ***full papers***, as well as ***reviews***, invited ***mini-reviews***, and invited research news. Publication in this journal is **entirely free of charge**, and all accepted papers will be available online immediately after typesetting. Dr. Ahmad Allahbakhsh, along with an international team of editors, leads the journal to meet the highest publication standards. We are looking forward to receiving your submissions.

Editor-in-Chief: Dr. Ahmad Allahbakhsh (Hakim Sabzevari University)

Director in charge: Prof. Gholamali Farzi (Hakim Sabzevari University)

International Editorial Board Members:

Prof. Ahmad Reza Bahramian (Tarbiat Modares University),
Prof. Mohammadhosein (Momo) Safari (Hasselt University),
Prof. Denis Rodrigue (Laval University),
Prof. Ursula Windberger (Medical University of Vienna),
Prof. Gholamali Farzi (Hakim Sabzevari University),
Prof. Sabu Thomas (Mahatma Gandhi University),
Dr. Hamidreza Oveisi (Hakim Sabzevari University),
Prof. Manoj Balachandran (CHRIST University),
Prof. Raffaella Mancuso (University of Calabria),
Dr. Ahmad Allahbakhsh (Hakim Sabzevari University)

Journal of Applied Material Science is an open-access journal, which means that all content is freely available without charge to the users and institutions. Users are allowed to read, download, copy, distribute, print, search, or link to the full texts of the articles, or use them for any other lawful purpose, without asking prior permission from the publisher or the author. This is in accordance with the BOAI definition of open access. Authors are free to deposit a copy of their paper (Published version, Version of Record) in an institutional or other repository of their choice.

To submit a manuscript: Please consult the **aim and scope** of the journal at: https://jams.hsu.ac.ir/journal/aim_scope

Guide for Authors is available at: https://jams.hsu.ac.ir/journal/authors.note

To **submit** your paper, please visit: https://jams.hsu.ac.ir/author

https://doi.org/10.22034/jams.2026.260101
J. Appl. Mater. Sci., **2026**, *2*, 260101.
© 2026 *J. Appl. Mater. Sci.* This material is licensed under a Creative Commons Attribution 4.0 International License.

Mechanical Characterization of Aluminum 6013-Red Mud Particulate Composites for Sustainable Structural Applications

Chandrashekara K.N. [a,*], Sreenivasa K. [a], Krupakara Palur Venkataswamy Setty [b]

[a] *S J C Institute of Technology, Chickballapur-562101, Karnataka, India*

[b] *Cambridge Institute of Technology North Campus, Devanahalli, Bangalore Rural -562110, India*

Editor's note: Red mud, a by-product of the Bayer process, is an abundant and eco-friendly material that can serve as a low-cost alternative for enhancing the mechanical and tribological properties of aluminum alloys. Chandrashekara K.N. et al. reinforced aluminum 6013 with red mud using liquid melt metallurgy. The results indicated that increasing the content of red mud improved various mechanical properties, including ultimate tensile strength, compressive strength, elongation, and hardness of aluminum 6013. These enhancements were attributed to factors such as particle distribution and grain refinement. The findings underscore the potential of red mud as a sustainable reinforcement material, promoting environmental sustainability in structural applications.

doi: 10.22034/jams.2026.260102

How to cite: C. K.N. et al. *Journal of Applied Material Science*, **2026**, *2*, 260102.

JOURNAL OF
APPLIED
MATERIAL
SCIENCE
jams.hsu.ac.ir

© 2026 *J. Appl. Mater. Sci.* This material is licensed under a Creative Commons Attribution 4.0 International License.

Journal of Applied Material Science **2026**, *2*, 260102
How to cite: C. K.N. et al., *Journal of Applied Material Science*, **2026**, *2*, 260102.
Journal homepage: **jams.hsu.ac.ir**

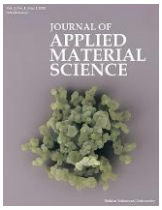

Original Research

Mechanical Characterization of Aluminum 6013-Red Mud Particulate Composites for Sustainable Structural Applications

Chandrashekara K. N. [a,*], Sreenivasa K. [a], Krupakara Palur Venkataswamy Setty [b]

[a] *S J C Institute of Technology, Chickballapur-562101, Karnataka, India*

[b] *Cambridge Institute of Technology North Campus, Devanahalli, Bangalore Rural -562110, India*

Abstract

In this study, the mechanical characteristics of aluminum 6013-red mud particulate composites were fabricated using the liquid melt metallurgy technique. Test samples were fabricated according to ASTM standards, and their mechanical properties, including ultimate tensile strength (UTS), compressive strength (CS), percentage elongation, and Brinell hardness, were systematically evaluated. The results revealed significant improvements in the mechanical behavior with increasing red mud content. UTS increased from 67.86 MPa for the base alloy to 142.20 MPa at 6 wt.% reinforcement, while compressive strength improved from 148 MPa to 182.42 MPa. The elongation percentage also increased from 44% to 72%, indicating enhanced ductility and strain hardening. Hardness values showed a steady increase from 54.92 BHN to 70.41 BHN with higher reinforcement. The observed enhancements are attributed to the uniform particle distribution, grain refinement, dislocation strengthening, and thermal mismatch effects between the matrix and reinforcement. These discoveries validate that red mud-reinforced aluminum 6013 composites are promising materials for structural applications in automotive, aerospace, and industrial sectors. Furthermore, this study highlights the sustainable use of red mud waste as an economical reinforcement material, contributing to the circular economy and environmental sustainability.

Keywords: Aluminum 6013 composites; Red mud particulates; Metal matrix composites; Mechanical properties; Industrial waste utilization; Sustainability.

1. Introduction

The demand for lightweight, high-performance, and sustainable materials has accelerated research into aluminum matrix composites (AMCs). These materials offer an exceptional strength-to-weight ratio, stiffness, and superior wear and corrosion resistance compared to conventional alloys [1-3]. Alongside mechanical performance, environmental sustainability and cost-effectiveness are becoming crucial. This has spurred interest in using industrial by-products and agricultural

* Corresponding author.
Email address: chandrasjcit2014@gmail.com (C. K.N.)

Received 2 November 2025
Revised 17 December 2025
Accepted 20 December 2025
Available online 1 January 2026

https://doi.org/10.22034/jams.2026.260102
© 2026 Authors. The authors retain copyright and full publishing rights under a CC BY 4.0 International License.

residues as reinforcements, promoting a circular economy while enhancing composite properties. Hybrid reinforcement strategies, combining natural fibers and industrial waste, have been shown to significantly improve tensile strength, hardness, and wear resistance, making AMCs suitable for automotive, aerospace, and defense applications [4, 5].

Conventional reinforcements such as SiC, B_4C, and Al_2O_3, while effective, are costly, restricting their industrial adoption [4, 6, 7]. In contrast, red mud, an abundant industrial by-product of the Bayer process, offers a low-cost, eco-friendly alternative, improving the mechanical and tribological performance of aluminum alloys [5, 8-10]. The mechanical performance of AMCs critically depends on uniform particle distribution and strong matrix–reinforcement bonding, which governs hardness, ductility, and wear resistance [6, 11, 12]. Evidence from studies on Al_{6061}, AA_{2017}, and hybrid Al_{7075} composites demonstrates that well-integrated reinforcements significantly enhance structural performance [10, 13, 14].

Although aluminum alloys such as Al_{6061} and Al_{7075} have been widely studied [15, 16], limited work has focused on Al_{6013} reinforced with red mud particulates. Al_{6013} offers good strength, corrosion resistance, and weldability [2, 3], while red mud, a major industrial waste, enhances mechanical properties through particle strengthening and grain refinement [8-10]. In this study, Al6013 was selected because its balanced properties and heat-treatable nature enable effective tailoring of mechanical behavior through particulate reinforcement, while the limited literature on sustainable reinforcements in Al6013-based composites highlights a clear research gap. This study aims to fabricate and characterize Al_{6013}–red mud composites produced by liquid metallurgy, evaluating the effect of red mud content on tensile, compressive, and hardness properties. The results are expected to identify an optimized, lightweight, and eco-friendly composite suitable for sustainable engineering applications [7, 9, 12].

To date, no systematic study has investigated the effects of red mud reinforcement on the mechanical behavior of Al6013-based composites. Given the promising results achieved in other Al alloys [10, 11, 13, 14], and considering Al6013's suitability for high-performance applications [2, 3], this study aims to explore the mechanical, microstructural, and tribological characteristics of Al6013/red mud composites fabricated through liquid metallurgy techniques.

2. Experimental

2.1. Materials

The base metal used in this investigation was Aluminum 6013 alloy, selected for its combination of good castability, mechanical strength, and tribological performance [15-17]. This alloy is particularly suitable for lightweight and durable components in structural and automotive applications. The detailed chemical composition is provided in Table 1.

The reinforcing material chosen was red mud, a fine, industrial by-product from alumina manufacture, with the size of the particle ranging between 50–80 µm [18]. This specimen was extracted from HINDALCO, Renukoot, India.

2.2. Composite preparation

The composites were fabricated using a liquid metallurgy route (stir casting), following methods adapted from Chandrashekara et al. [19, 20]. Stir casting is a cost-effective and scalable technique for producing particle-reinforced metal matrix composites. The Al 6013 alloy was melted in a graphite crucible using an electric resistance furnace at 750 ± 10°C [21]. Red mud particles were preheated to 300°C to remove moisture, and hexachloroethane was used for degassing the molten metal. Red mud was gradually introduced into the melt under continuous stirring at approximately 500 rpm for 10 minutes to achieve uniform particle distribution. The molten slurry was poured into preheated metal molds to produce castings. Three composite variants were prepared, containing 2, 4, and 6 wt.% red mud. The homogeneity of reinforcement was confirmed using scanning electron microscopy (SEM).

Table 1. Chemical composition of Al 6013 alloy (wt.%)

Element	Al	Mg	Si	Cu	Mn	Fe	Zn	Cr	Ti
Wt.%	94.8	0.80	0.60	0.60	0.20	0.50	0.25	0.10	0.10

© 2026 Authors. The authors retain copyright and full publishing rights under a CC BY 4.0 International License.

2.3. Measurements

After solidification, the composite castings were machined into standardized test specimens using CNC lathes. Only defect-free test bars were selected for mechanical testing. The following ASTM standards were followed: Tensile testing: ASTM E8/E8M, Compression testing: ASTM E9, Hardness testing: ASTM E10.

Tensile specimens were prepared with a 20 mm diameter, 120 mm overall length, 40 mm gauge length, and 12 mm gauge diameter. Tensile tests were conducted using an Instron 1175 universal testing machine at a crosshead speed of 0.5 mm/min, recording ultimate tensile strength (UTS) and elongation. Compression specimens were cylindrical (20 mm diameter, 20 mm height) and tested at 0.2 mm/min. Brinell hardness was measured using a 5 mm steel ball under a 500 kgf load for 30 seconds, taking multiple readings for each sample to obtain reliable averages.

3. Results and discussion

3.1. Microstructural Analysis

SEM analysis was conducted to evaluate the dispersion of red mud particles within the Al 6013 matrix and to identify any casting defects. Figures 1a–1d show micrographs of the unreinforced alloy and composites containing 2, 4, and 6 wt.% red mud. The base alloy exhibited a typical dendritic aluminum structure with intermetallic phases (Figure 1a). In the composites, red mud particulates were homogenously dispersed through the matrix (Figures 1b–d), with minimal agglomeration at lower reinforcement levels. Slight clustering was noted at 6 wt.% red mud, consistent with trends reported by Alaneme et al. [22]. No significant porosity or interfacial cracking was observed, indicating strong matrix-reinforcement bonding. The uniform particle distribution is attributed to effective stirring and preheating during fabrication, in line with previous work on ceramic-reinforced aluminum composites.

3.2. Tensile Properties

The outcomes of tensile tests are briefed in Table 2 and illustrated in Figure 2**.** Six samples were verified per composite type, and average values are reported. The ultimate strength (UTS) of the unreinforced Al 6013 alloy was 67.86 MPa. With the addition of 2 wt.% red mud, the UTS increased to 123.76 MPa, an 82% improvement. Further reinforcement with 4 wt.% and 6 wt.% red mud

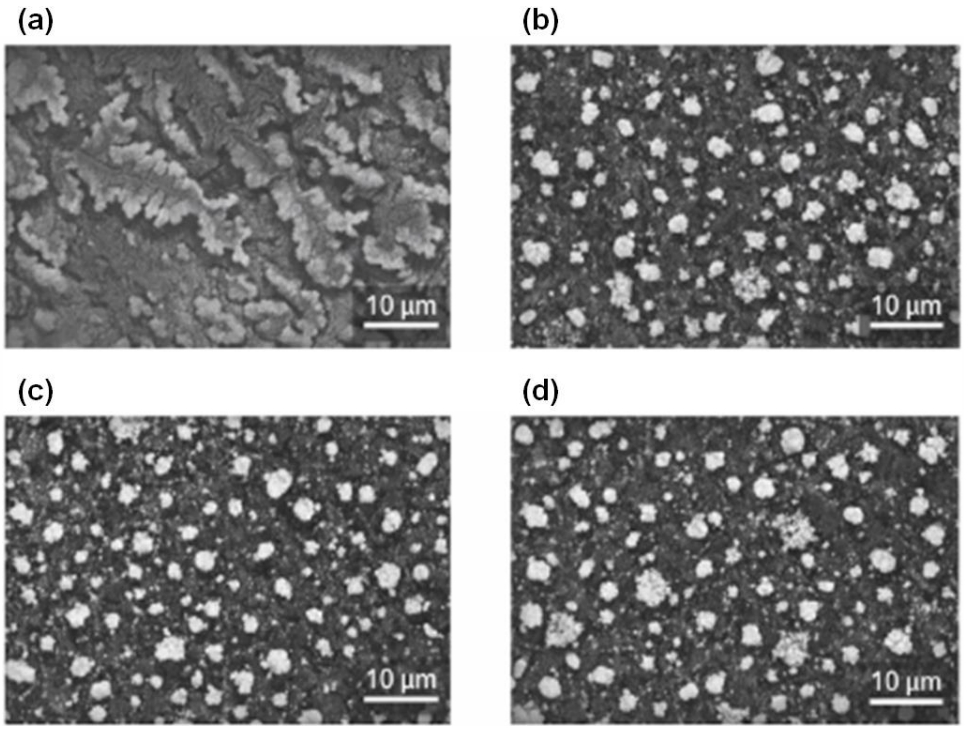

Figure 1. SEM images of: (a) Al 6013 alloy, and composites reinforced with (b) 2, (c) 4, and (d) 6 wt.% of red mud.

© 2026 Authors. The authors retain copyright and full publishing rights under a CC BY 4.0 International License.

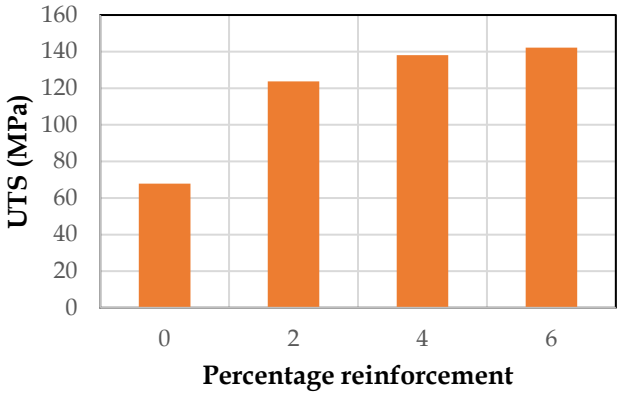

Figure 2. UTS values against reinforcement.

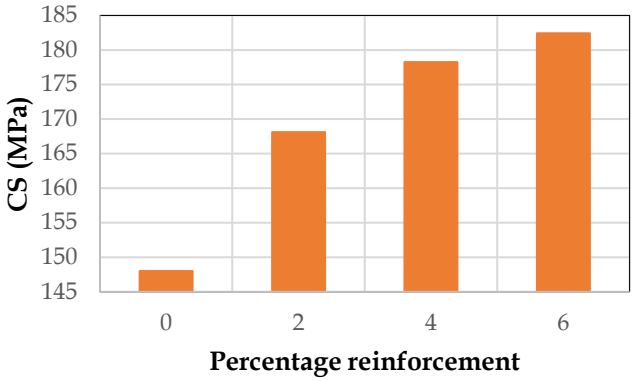

Figure 3. CS values against reinforcement.

led to UTS values of 138.10 MPa and 142.20 MPa, respectively. The improvement in tensile strength is attributed to the existence of rigid red mud particulates, which restrict dislocation motion and plastic flow; grain refinement caused by heterogeneous nucleation at ceramic interfaces; and enhanced dislocation density from the thermal mismatch between the aluminum matrix and ceramic particles [23]. These mechanisms are consistent with findings by Arzum Işıtan et al. [24], who described analogous behavior for Al 6013 reinforced with Al_2O_3 nanoparticles. A slight reduction in ductility was observed with increasing red mud content, which is a typical behavior in particle-reinforced metal matrix composites [23].

3.3. Compressive strength

The results of the compressive strength (CS) tests for Al 6013–red mud composites are shown in Table 3 and Figure 3. The average values reported were obtained from six specimens per composition. A noticeable improvement in CS was observed with increasing red mud content. The unreinforced Al 6013 alloy exhibited a CS of 148 MPa. The addition of 2 wt.% red mud raised this value to 168.1 MPa, while further increments to 4 wt.% and 6 wt.% resulted in strengths of 178.25 MPa and 182.42 MPa, respectively. This enhancement can be attributed to the load-bearing capacity provided by the rigid red mud particulates, which restrict matrix deformation under compressive loads. Moreover, the incorporation of these particles helps reduce casting defects such as microvoids and porosity, promoting a denser, more compact microstructure. Similar improvements in compressive strength with ceramic reinforcements in aluminum alloys have also been reported by Pruthviraj et al. [25].

3.4. Elongation behavior

The percentage elongation values of the Al6013–red mud composites are presented in Table 4 and Figure 4. A progressive increase in elongation was observed with increasing red mud content, which is unusual for ceramic particle–reinforced metal matrix composites, where ductility typically decreases due to particle-induced stress concentrations and embrittlement [26]. In this study, the enhanced elongation can be attributed to the uniform dispersion of fine red mud particulates, which promotes effective load transfer between the aluminum matrix and the reinforcement. Additionally,

Table 2. UTS values of matrix and composites

Specimen	Average UTS (MPa)
Matrix alloy Aluminum 6013	67.86
Aluminum 6013 + 2% Red mud particulates	123.76
Aluminum 6013 + 4% Red mud particulates	138.10
Aluminum 6013 + 6% Red mud particulates	142.20

Table 3. UTS values of matrix and composites

Specimen	Average CS (MPa)
Matrix alloy Aluminum 6013	148
Aluminum 6013 + 2% Red mud particulates	168.1
Aluminum 6013 + 4% Red mud particulates	178.25
Aluminum 6013 + 6% Red mud particulates	182.42

© 2026 Authors. The authors retain copyright and full publishing rights under a CC BY 4.0 International License.

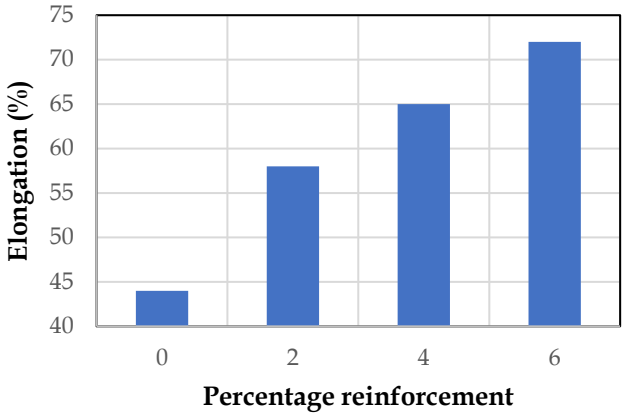

Figure 4. Elongation values against reinforcement.

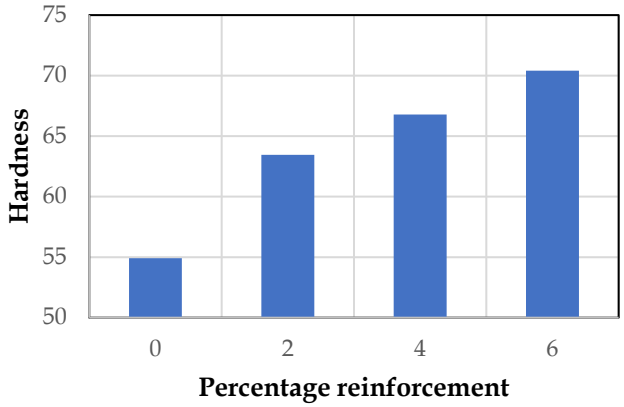

Figure 5. Hardness values against reinforcement.

the red mud particles act as sites for heterogeneous nucleation during solidification, leading to grain refinement and a more uniform microstructure. This refined microstructure facilitates uniform plastic deformation, delays localized necking, and suppresses premature crack initiation, collectively improving ductility. Moreover, the fine particle size and optimized content of red mud minimize stress concentrations and reduce the likelihood of particle clustering, which often causes embrittlement in conventional composites. Similar trends have been reported in aluminum-based composites where controlled reinforcement and proper processing resulted in simultaneous enhancement of ductility, strength, and hardness [27]. These results indicate that red mud can serve as an effective and sustainable reinforcement for Al6013 without compromising its ductility.

3.5. Hardness

Table 5 and Figure 5 display the variation in Brinell hardness (HB) with increasing red mud content in Al 6013 composites. The values represent the average of six measurements for each composition. A progressive enhancement in hardness was witnessed with the addition of red mud particulates. The unreinforced alloy exhibited a baseline hardness of ~75 HB, which steadily increased with 2, 4, and 6 wt.% red mud content. This improvement is primarily recognized due to the existence of hard ceramic phases like Fe_2O_3, TiO_2, and SiO_2 within red mud, which act as effective barriers to dislocation motion and enhance resistance to localized plastic deformation. Furthermore, the rigid particulates contribute to load sharing during indentation, thereby increasing the material's ability to withstand static loads, abrasion, and surface wear. Similar trends were reported in TiO_2-reinforced aluminum alloys and by Zhang et al. for various ceramic-reinforced MMCs. The outcomes endorse that red mud serves as a cost-effective reinforcement for improving the surface hardness of Al 6013 alloys [28].

4. Conclusions

Aluminum 6013–red mud metal matrix composites were fabricated via the liquid metallurgy method with varying red mud contents, such as 2, 4, and 6 wt.%. The accumulation of red mud particles led to significant improvements in tensile strength (~82% increase in UTS)

Table 4. Elongation values of matrix and composites

Specimen	Elongation (%)
Matrix alloy Aluminum 6013	44
Aluminum 6013 + 2% Red mud particulates	58
Aluminum 6013 + 4% Red mud particulates	65
Aluminum 6013 + 6% Red mud particulates	72

Table 5. Hardness values of matrix and composites

Specimen	Hardness
Matrix alloy Aluminum 6013	54.92
Aluminum 6013 + 2% Red mud particulates	63.45
Aluminum 6013 + 4% Red mud particulates	66.78
Aluminum 6013 + 6% Red mud particulates	70.41

© 2026 Authors. The authors retain copyright and full publishing rights under a CC BY 4.0 International License.

and compressive strength (~23% enhancement) compared to the unreinforced alloy, primarily due to dispersion strengthening, grain refinement, and increased dislocation density arising from the thermal mismatch between the matrix and the ceramic-rich reinforcement. The Brinell hardness also increased progressively with reinforcement, as the hard phases in red mud acted as effective barriers to dislocation motion. Although a marginal reduction in ductility and durability was perceived with increasing red mud content typical for ceramic particle-reinforced composites, these values persisted within tolerable ranges for many structural applications. SEM analysis confirmed a uniform particle distribution with good interfacial bonding, contributing to the observed mechanical enhancements. This study establishes that red mud, a low-cost industrial waste, can be effectively valorized as a sustainable reinforcement for aluminum 6013 alloys, with an optimal balance of mechanical properties achieved at 4 wt.% addition, offering promising applications in automotive, aerospace, and structural components.

Conflict of Interest

The authors declare no conflict of interest.

References

1. D. Miracle. Metal matrix composites – From science to technological significance. *Composites Science and Technology*, **2005**, *65*, 2526.
2. S.C. Tjong. Novel Nanoparticle-Reinforced Metal Matrix Composites with Enhanced Mechanical Properties. *Advanced Engineering Materials*, **2007**, *9*, 639.
3. R. Dasgupta. Aluminium Alloy-Based Metal Matrix Composites: A Potential Material for Wear Resistant Applications. *ISRN Metallurgy*, **2012**, *2012*, 1.
4. M.K. Surappa. Aluminium matrix composites: Challenges and opportunities. *Sadhana*, **2003**, *28*, 319.
5. P. Samal, R.K. Mandava, and P.R. Vundavilli. Dry sliding wear behavior of Al 6082 metal matrix composites reinforced with red mud particles. *SN Applied Sciences*, **2020**, *2*, 313.
6. M. Kok. Production and mechanical properties of Al2O3 particle-reinforced 2024 aluminium alloy composites. *Journal of Materials Processing Technology*, **2005**, *161*, 381.
7. S.V. Prasad and R. Asthana. Aluminum Metal-Matrix Composites for Automotive Applications: Tribological Considerations. *Tribology Letters*, **2004**, *17*, 445.
8. K.N. Chandrashekara, et al. Corrosion Properties of Advanced Materials like Aluminium 6013 Metal Matrix Composites Reinforced with Red Mud Particulates in Acid Chloride Medium. *Asian Journal of Chemistry*, **2016**, *28*, 1770.
9. S.M. Quader, B.S. Murthy, and P. Ravinder Reddy. Processing and Mechanical Properties of Al₂O₃ and Red Mud Particle Reinforced AA6061 Hybrid Composites. *Journal of Minerals and Materials Characterization and Engineering*, **2016**, *04*, 135.
10. N.D. Chinta, N. Selvaraj, and V. Mahesh. Mechanical characterization of aluminium – red mud metal matrix composites. *Materials Today: Proceedings*, **2018**, *5*, 26911.
11. J. Hashim, L. Looney, and M.S.J. Hashmi. Particle distribution in cast metal matrix composites—Part I. *Journal of Materials Processing Technology*, **2002**, *123*, 251.
12. D.J. Lloyd. Particle reinforced aluminium and magnesium matrix composites. *International Materials Reviews*, **1994**, *39*, 1.
13. B. Geetha and K. Ganesan. Effects of Red Mud Reinforcement on Hardness, Wear Behaviour of Cast Al-6Si-0.45 Mg Alloy. *Applied Mechanics and Materials*, **2015**, *787*, 658.
14. M. Gangadharappa, et al. Corrosion behavior of Al6061 hybrid composites reinforced with red mud particles and E-glass fiber. *Materials Today: Proceedings*, **2021**, *46*, 6068.
15. A. Heinz, et al. Recent development in aluminium alloys for aerospace applications. *Materials Science and Engineering: A*, **2000**, *280*, 102.
16. M.R.W.S. Abdala, et al. Thermoelectrical power analysis of precipitation in 6013 aluminum alloy. *Materials Characterization*, **2008**, *59*, 271.
17. M. Ayvaz. Determination of the effect of artificial aging parameters on dry sliding wear resistance of 6013 aluminum alloy (Al-Mg-Si-Cu). *International Advanced Researches and Engineering Journal*, **2021**, *5*, 181.
18. S.K. Tripathy and A.K. Senapati. A review on turning analysis of industrial waste reinforced aluminum metal matrix composite. *Materials Today: Proceedings*, **2020**, *33*, 5740.
19. N. Panwar, et al. Fabrication of Aluminum 6061 Red-mud Composite using Stir Casting and Micro Structure Observation. *Materials Today: Proceedings*, **2020**, *21*, 2014.
20. J. Hashim, L. Looney, and M.S.J. Hashmi. Metal matrix composites: production by the stir casting method. *Journal of Materials Processing Technology*, **1999**, *92-93*, 1.

© 2026 Authors. The authors retain copyright and full publishing rights under a CC BY 4.0 International License.

21. G. Siva Karuna, S.V.G. Swamy, and G.S. Naidu. Effect of Blast Furnace Slag and Red Mud Reinforcements on the Mechanical Properties of AA2024 Hybrid Composites. *Advanced Materials Research*, **2018**, *1148*, 29.

22. K.K. Alaneme and M.O. Bodunrin. Corrosion Behavior of Alumina Reinforced Aluminium (6063) Metal Matrix Composites. *Journal of Minerals and Materials Characterization and Engineering*, **2011**, *10*, 1153.

23. J. Singh and A. Chauhan. Fabrication characteristics and tensile strength of novel Al2024/SiC/red mud composites processed via stir casting route. *Transactions of Nonferrous Metals Society of China*, **2017**, *27*, 2573.

24. A. Işıtan, S. Aytekin, and V. Onar. Enhancing the Microstructure and Mechanical Properties of Cast Aluminum Matrix Composites Through Nano-Al2O3 Reinforcement via CMT and PMC Welding. *International Journal of Metalcasting*, **2024**, *18*, 3166.

25. D.R. Ramya and R.D. Pruthviraj. Mechanical behaviour of As-Cast and Heat-Treated: AA2024 Alloy Silicon Carbide-Al2O3 Hybrid Composites. *Bulletin of Pure & Applied Sciences-Chemistry*, **2020**, *39c*, 56.

26. Y.-y. Chen, et al. Enhancing strength–ductility synergy of AlNp/Al composite by regulating heterostructure of matrix grain and particle distribution. *Transactions of Nonferrous Metals Society of China*, **2024**, *34*, 1049.

27. D. Mao, et al. Strength-ductility balance strategy in SiC reinforced aluminum matrix composites via deformation-driven metallurgy. *Journal of Alloys and Compounds*, **2022**, *891*, 162078.

28. H. Pi, et al. Microstructure, Hardness and Corrosion Resistance of Al-TiC MMC Prepared by Laser Cladding on AZ31B Magnesium Alloy. *Coatings*, **2024**, *14*, 211.

© 2026 Authors. The authors retain the copyright and full publishing rights. This article is licensed under a Creative Commons Attribution 4.0 BY International License.

© 2026 Authors. The authors retain copyright and full publishing rights under a CC BY 4.0 International License.

Photoelectrochemical Hydrogen Generation from Seawater Using Modified g-C_3N_4/NiO Photo-electrode Heterojunction

Jyoti Bhattacharjee [a], Preetam Datta [b], Abdul Aziz Shaikh [b], Akash Sathianarayanan [c], Milan Kumar Mandal [a], Subhasis Roy [a,*]

[a] *Department of Chemical Engineering, University of Calcutta, 92 A. P. C. Road, Kolkata- 700009, India*

[b] *Centre for Research in Nanoscience and Nanotechnology (CRNN), University of Calcutta, JD 2, Sector III, Salt Lake, Kolkata-700106, West Bengal, India*

[c] *Department of Science, Alliance University, 562106, Bengaluru, Karnataka, India*

Editor's note: Generating hydrogen through water splitting, facilitated by solar radiation, is becoming an increasingly viable method for producing clean energy. Bhattacharjee et al. studied the process of seawater splitting for hydrogen production using a nickel oxide (NiO)/iron-doped graphitic carbon nitride (Fe/g-C_3N_4/NiO) photoelectrode in combination with polyvinyl alcohol membranes, along with a molecular sensitizer. The proposed approach has the potential to promote sustainable green hydrogen production from seawater.

doi: 10.22034/jams.2026.260103

How to cite: J. Bhattacharjee et al. *Journal of Applied Material Science*, **2026**, *2*, 260103.

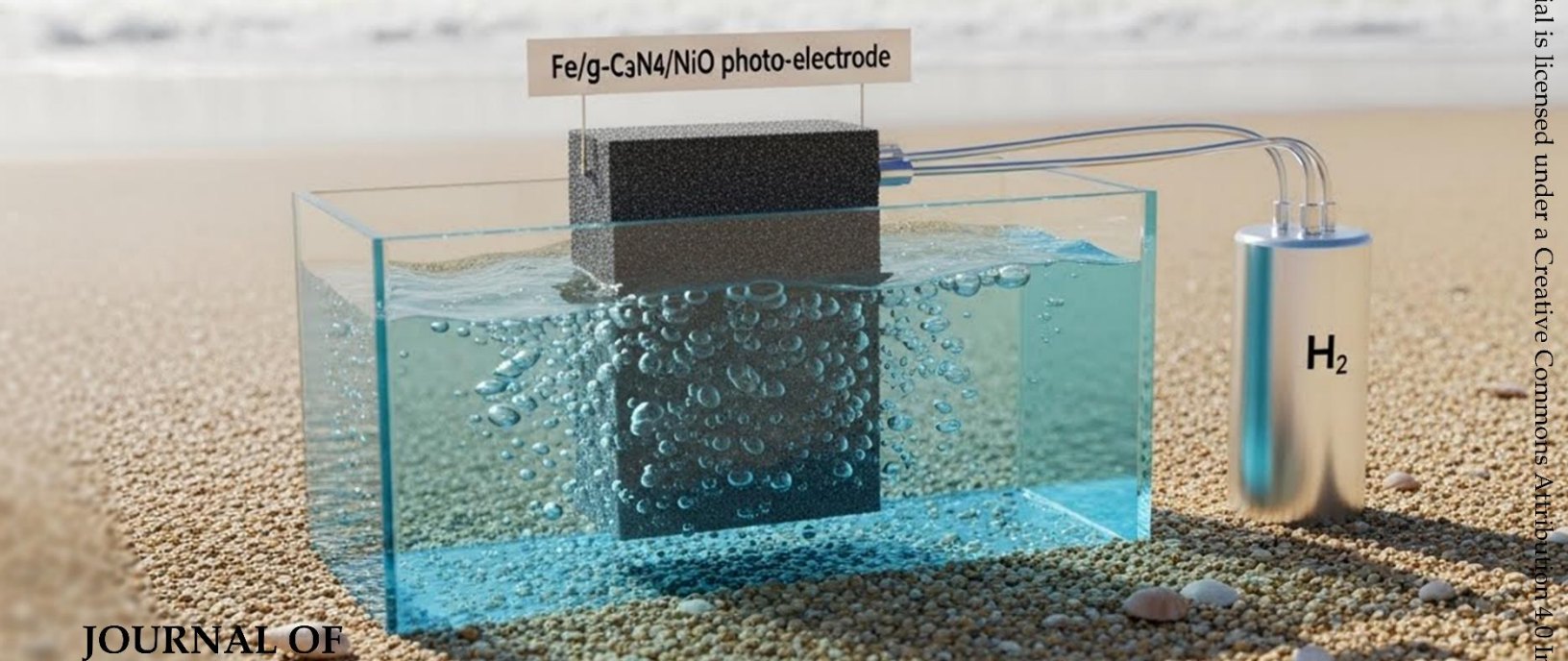

JOURNAL OF
APPLIED
MATERIAL
SCIENCE
jams.hsu.ac.ir

© 2026 *J. Appl. Mater. Sci.* This material is licensed under a Creative Commons Attribution 4.0 International License.

Journal of Applied Material Science **2026**, 2, 260103
How to cite: J. Bhattacharjee et al., *Journal of Applied Material Science*, **2026**, 2, 260103.
Journal homepage: **jams.hsu.ac.ir**

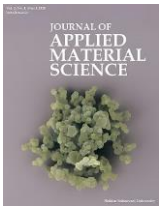

Original Research

Photoelectrochemical Hydrogen Generation from Seawater Using Modified g-C_3N_4/NiO Photo-electrode Heterojunction

Jyoti Bhattacharjee [a], Preetam Datta [b], Abdul Aziz Shaikh [b], Akash Sathianarayanan [c], Milan Kumar Mandal [a], Subhasis Roy [a,*]

[a] *Department of Chemical Engineering, University of Calcutta, 92 A. P. C. Road, Kolkata- 700009, India*

[b] *Centre for Research in Nanoscience and Nanotechnology (CRNN), University of Calcutta, JD 2, Sector III, Salt Lake, Kolkata-700106, West Bengal, India*

[c] *Department of Science, Alliance University, 562106, Bengaluru, Karnataka, India*

Abstract

This study investigates seawater splitting for hydrogen evolution via a photoelectrode-membrane assembly. A composite photoelectrode of nickel oxide (NiO) and iron-doped graphite carbon nitride (g-C_3N_4) was fabricated and characterized to determine its suitability for photocatalytic activity. PVA-based membranes were integrated within the reactor to explore ion transport and selectivity in photoelectrochemical device (PEC) configurations. Fluorene–Thiophene–Triphenylamine–Coumarin (FTTC) molecular sensitizer when used in conjunction with a novel Fe/g-C_3N_4/NiO photoelectrode system, resulting in an increase in hydrogen production through solar energy from seawater. The seawater splitting experiments were conducted at various applied voltages, and the system's efficiency was evaluated based on the hydrogen evolution rate, current density, and stability when subjected to seawater. These advancements can be pivotal in decarbonizing maritime energy infrastructures and enabling distributed green hydrogen production in coastal regions. PVA membrane emerges as a promising candidate due to its high selectivity and durability, while the Fe-g-C_3N_4/NiO photoelectrode proves effective for solar-driven hydrogen generation in harsh saline environments. The membrane can reject Cl^- ions by more than 90% but it allows H^+ and OH^- ions to pass with a conductivity of 10^{-3} S/cm, and this is the reason why, after 24 hours, only 15% of the photocurrent is lost, while in the case of no membrane, 50% decay occurs.

Keywords: Seawater splitting; g-C_3N_4; Hydrogen evolution; Photoelectrode.

* Corresponding author.
Email address: srchemengg@caluniv.ac.in (S. Roy)

Received 2 December 2025
Revised 29 December 2025
Accepted 31 December 2025
Available online 4 January 2026

https://doi.org/10.22034/jams.2026.260103
© 2026 Authors. The authors retain copyright and full publishing rights under a CC BY 4.0 International License.

1. Introduction

A sudden depletion of fossil fuels worldwide is prompting numerous researchers to explore new sources of renewable and green energy carriers. Technology to harness solar energy has gained considerable acclaim recently, as solar radiation is a significant sustainable energy source that falls on the Earth's surface [1-3]. Hydrogen (H_2) seems to be one of the most viable alternative fuels as a substitute for various non-renewable cradles of energy, for example, coal, petroleum, etc., which increase environmental pollution resulting in global warming [4-9].

Hydrogen, a pollution-free energy source, can be produced from a wide range of natural resources, such as water (H_2O) and natural gas. The production of H_2 gas through water splitting, facilitated by the application of solar radiation, appears to be an increasingly popular choice as a clean energy carrier, following a significant decrease in environmental pollution levels [10, 11]. Various technological forms produce hydrogen with solar radiation, such as photoelectrolysis, photo-electrochemical, photocatalysis, photo-biological, and photodegradation systems. After the discovery of the photo-electrocatalytic (PEC) H_2 production by Fujishima and Honda in 1972 with the assistance of a titanium dioxide electrode, the process has gained worldwide attention as PEC cells possess the potential for direct conversion of the energy received from the sun to chemical fuel, which achieves easy storage in its covalent bonds [12, 13].

The novelty of this study lies in the combined use of Fe-doped g-C_3N_4/NiO heterojunction integration with FTTC molecular sensitization and PVA membrane separation, designed for direct seawater electrolysis, which resulted in stable H_2 production that overcomes the saline-corrosion challenges that have caused instability in previous g-C_3N_4 systems. In contrast to the traditional Fe-doped g-C_3N_4 (seeking either pollutant degradation or pure water PEC with 1.0% ABPE) or the g-C_3N_4/NiO heterojunctions that are limited by poor visible-light harvesting and Cl^- instability, the present work introduces a new mechanism consisting of three elements: Fe-induced mid-gap states facilitating charge redistribution, FTTC acting as a corrosion-resistant bridge allowing for directional e^-/h^+ separation (NiO holes to g-C_3N_3 electrons), and PVA's capacity to discriminating between Mg^{2+}/Ca^{2+} in seawater, resulting in the record of 1.0% ABPE at 0.95 V vs. RHE with 80-90% photocurrent retention over 24h. Therefore, establishing an effectively planned system for conducting photoelectrochemical water splitting remains a serious challenge.

Scientists worldwide are making relentless efforts to conduct research on the novel design of semiconducting materials for commercial use of photoelectrolysis of water for H_2 production [10, 14]. This research paper examines the fundamental concept and applications of semiconducting materials in photoelectrochemical water splitting, with a focus on the development of a novel electrolyte derived from seawater purification using membrane technology. Therefore, various challenges that researchers or scientists encounter when examining such processes and opportunities for further improvement to overcome these drawbacks have been briefly explained. The Fe-g-C_3N_4/NiO photochemical cell's reported ABPE of 1.0% at 0.95 V vs. RHE is a substantial enhancement over the undoped reference (0.97% at 0.1 V), but still appears comparatively small compared to state-of-the-art systems that achieve 5-10% under optimal conditions. The primary cause of this difference in performance is the inherent drawbacks of g-C_3N_4, like the high-speed electron-hole recombination rates, bad band alignment for the seawater electrolysis, which is even more aggravated by Cl^- corrosion, and also slow OER kinetics, and low mobility of charge carriers in the heterojunction, where Fe-doping has made some improvements.

The paper discusses the Fluorene–Thiophene–Triphenylamine–Coumarin (FTTC) molecular sensitizer when used in conjunction with a novel Fe/g-C_3N_4/NiO photocatalytic system, resulting in an increase in hydrogen production through solar energy from seawater. The donor–π–acceptor approach led to the attainment of deep absorption in the visible region of light, prompt excitation of electrons, and excellent separation of the charge carriers created as a result of the photo-activity in the case of the FTTC molecule. Additionally, FTTC serves as an electronic bridge between the g-C_3N_4 and NiO layers, which are responsible for the conduction of hydrogen evolution. This pipeline of the mechanism reduces the recombination of electron-hole pairs, increasing photocurrent generation. The FTTC molecule, due to its rigid and stable structure, as well as its photostability, is a highly durable and stable material that can even withstand chloride corrosion, making it suitable for use

© 2026 Authors. The authors retain copyright and full publishing rights under a CC BY 4.0 International License.

in seawater applications. Table 1 illustrates that the foremost enhancements in this regard are Fe-doping and heterojunction formation, along with their corresponding charge separation and light absorption in the visible spectrum. However, the comparison of the advancements also includes pure or singly modified systems. It is worth noting that parameters such as electrolyte (seawater vs. pure water) and bias have been considered for a fair evaluation.

2. Experimental

2.1. Materials

The chemicals were all obtained from commercial sources, including iron (II) chloride tetrahydrate ($FeCl_2 \cdot 4H_2O$, ≥99.0%) and nickel(II) nitrate hexahydrate ($Ni(NO_3)_2 \cdot 6H_2O$, ≥98.0%), which were purchased from Merck. Melamine ($C_3H_6N_6$, SRL Labs, ≥99.0%) was employed as the g-C_3N_4 precursor. $CO(NH_2)_2$ urea (Merck, 99%), NaOH pellets (AR, Polypharm Private Limited, 98%), KCl (Merck, ≥99.0%), and analytical grade ethanol (Merck) were used without further purification. FTO-coated glass slides (10 Ω cm^{-2}, Sigma-Aldrich) were employed as substrates to fabricate electrodes. Double-distilled water from a double-distillation facility was used during the experiment.

2.2. Synthesis of Fe/ g-C_3N_4 / NiO nanostructures and preparation of g-C_3N_4/NiO photoelectrode

Graphitic carbon nitride (g-C_3N_4) was synthesized by pyrolysis of melamine. In the standard synthesis, 10 g of melamine powder was loaded into a covered alumina crucible and heated in a muffle furnace from room temperature to 550 °C at a rate of 5 °C min^{-1}, then soaked at 550 °C for 3 hours, and cooled naturally to room temperature. The resulting yellow powder was pulverized using an agate mortar to obtain a fine g-C_3N_4 powder and was then placed in a desiccator. Hydrothermal-annealing route synthesis of Fe nanoparticles: Fe nanoparticles were prepared by a facile co-precipitation and then treated with mild heat. Typically, 0.01 mol (≈approximately 1.99 g) of $FeCl_2 \cdot 4H_2O$ was dissolved in 40 mL of deionized water with vigorous agitation. In a separate experiment, 0.02 mol of urea (1.20 g) was dissolved in 20 mL of DI water and was added dropwise to the iron solution with stirring. The pH was gradually adjusted to ~9 by adding a 1.0 M NaOH solution, which formed a dark greenish precipitate. The resulting mixture was transferred to a 50 mL Teflon-lined autoclave and kept at 160 °C for 12 h.

The process of glutaraldehyde cross-linking was carried out on polyvinyl alcohol (molecular weight 89,000-98,000, 5% by weight) for 24 hours at a concentration of 2% in 0.1 M sulfuric acid. After that, the resulting polymeric film was applied to a Nafion fabric (50 µm thick), resulting in an anion-exchange membrane with an ionic exchange capacity (IEC) of 1.8 meq/g and a swelling ratio of less than 15% in a 3.5% sodium chloride solution.

2.3. Preparation of Fe/g-C_3N_4 composite

To fabricate the Fe-doped (0.5 weight per volume%) g-C_3N_4 heterostructure, 0.05 g of as-synthesized g-C_3N_4 powder was dispersed in 30 mL of DI water and sonicated for two hours to form a homogenous suspension. Independently, 0.05 g of FeO nanoparticles was dispersed in 20 mL DI water and sonicated for 30 min. The FeO dispersion was introduced into the suspension of g-C_3N_4, and the mixture was stirred vigorously at 60 °C for one hour. The product was cooled down, washed with DI water and ethanol several times, and dried under reduced pressure at 60 °C for four hours to obtain the 0.5 per cent Fe-doped g-C_3N_4 composite powder.

Table 1. Current state of the art and this paper

Material/System	ABPE (%) / Bias (V vs. RHE)	Photocurrent Density (mA/cm^2) / Potential	Electrolyte	Reference
Fe-g-C_3N_4/NiO (this work)	1.0 / 0.95	1.6-1.9 / 1.4-1.5	Purified Seawater	This paper
g-C_3N_4/NiO (undoped baseline)	0.97 / 0.1	1.0 / 1.4-1.5	Purified Seawater	This paper
TiO_2/g-C_3N_4/CNT	-	2.94 / 1.23	NaOH	[12]
Protonated g-C_3N_4/N-TiO_2	-	0.52 / 1.23	KOH	[12]
TiO_2/g-C_3N_4 NTA	-	0.86 / 1.23	KOH	[12]
Mg/Li co-doped g-C_3N_4.	-	0.126 / 0	KOH	[13]
CdTe/CdS/TiO_2/Ni (NiO-like)	0.95 / 0.22	8.16 / 0	Neutral buffer	[13]

© 2026 Authors. The authors retain copyright and full publishing rights under a CC BY 4.0 International License.

2.4. Measurements

All of the photoelectrochemical processes were performed under a calibrated 300 W Xe lamp (Newport Oriel 91160 series) that emitted AM 1.5G light with a power of 100 mW/cm² (1 sun). A Si reference cell was used for this purpose, which was confirmed to be traceable to standards maintained at the National Renewable Energy Laboratory (NREL).

The total illuminated area was 1 cm², which included an FTO (Fluorine-doped Tin Oxide) active window where the light was turned on and off (30s on/off) for transient response; full-spectrum light delivery (300-1100 nm) with UV cutoff filter (>420 nm) was used for visible-light bias tests to mimic solar input. The consistency of intensity was guaranteed through spatial mapping (±5% variation); the total exposure for LSV/CV was approximately 30-60 minutes.

Photoelectrochemical measurements were carried out by a potentiostat (CHI660E) using a three-electrode configuration with Fe-g-C_3N_4/NiO or g-C_3N_4/NiO as the working electrode (1 cm²), a Pt mesh as the counter, and Ag/AgCl reference in the electrolyte of 1 M purified seawater with only positive ions present, which has been tested by a TDS (Total dissolved solids) meter. The 300 W Xe arc lamp (Newport 91160) with a 420 nm cutoff simulated sunlight (AM 1.5G, 100 mW/cm²). For H_2, long-term stability was tested through 24-hour chronoamperometry at 1.23 V vs. RHE in natural seawater.

The UV-Vis spectrophotometric measurements were conducted using a UV-Vis Spectrophotometer equipped with a deuterium lamp as the light source. The wavelength range employed for the experiments spanned from 190 nm to 900 nm. A Rigaku XtaLAB Pro2 Mo X-ray Diffractometer (XRD) operated with a copper Kα radiation source was used for XRD analysis.

Morphological characterization was performed utilizing a JEOL JSM 5600 Scanning Electron Microscope (SEM). Raman spectroscopy analysis was carried out using a Horiba LabRam HR Evolution spectrometer.

Electrochemical properties were investigated using an Autolab IMP potentiostat/galvanostat equipped with the FRA32M.MAC.204.S frequency response analyzer module. Moreover, transmission electron microscopy (TEM) imaging was performed using a JEOL JEM-1400 Microscope.

3. Results and discussion

3.1. Structural characterizations

Figure 1 presents the electronic properties of the gC_3N_4-based semiconductor. The data calculated from Figure 1a electronic band structure revealed a direct electronic band gap of approximately 2.0 eV at the Γ point, indicating the material is semiconducting. The valence band maximum (VBM) primarily consisted of nitrogen orbital contributions, and the conduction band minimum (CBM) made substantial contributions from carbon, with significant C–N hybridization, as shown in Figure 1b.

The X-ray diffraction (XRD) spectra in Figure 1c show that the g-C_3N_4/NiO and Fe-g-C_3N_4/NiO samples exhibit the same general pattern of broad peaks. These peaks, located at approximately 2θ = 37–38°, can be attributed to the NiO (111) orientation. At higher angles, there are reflections of minor intensity from the (200) and (220) planes.

The broad background and absence of extra sharp peaks are indicators that the g-C_3N_4 phase is mainly disordered. Therefore, the presence of Fe is as a low-level dopant only, with no separate crystalline FeOx phases seen by XRD in Figure 1c. Slightly higher peak intensity and slight broadening of the peak are observed for the Fe-g-C_3N_4/NiO sample in comparison with the g-C_3N_4/NiO sample, which suggests better crystallinity and slight lattice distortion due to the incorporation of Fe in the NiO/g-C_3N_4 structure, a fact that might offer charge transport and interfacial coupling in the heterojunction, a positive effect.

Figure 1b shows the E_g values of both doped and undoped electrodes, which have been estimated in accordance with the graphical representation of $(\alpha h\upsilon)^{1/2}$ vs. energy ($h\upsilon$). The energy gaps (E_g) of as-synthesized nanostructures were approximately calculated by using Tauc's method [15]:

$$\alpha h\upsilon = A(h\upsilon - E_g)^{n/2} \quad (1)$$

where α, h, υ, E_g, and A are the absorption coefficient, Planck's constant, optical frequency, bandgap, and steady state, respectively.

In Figure 1d, the Raman spectra reveal the comparison between the vibrations of g-C_3N_4/NiO and Fe-g-C_3N_4/NiO. Moreover, their spectra indicate the extent of Fe's influence on the carbon-nitrogen

© 2026 Authors. The authors retain copyright and full publishing rights under a CC BY 4.0 International License.

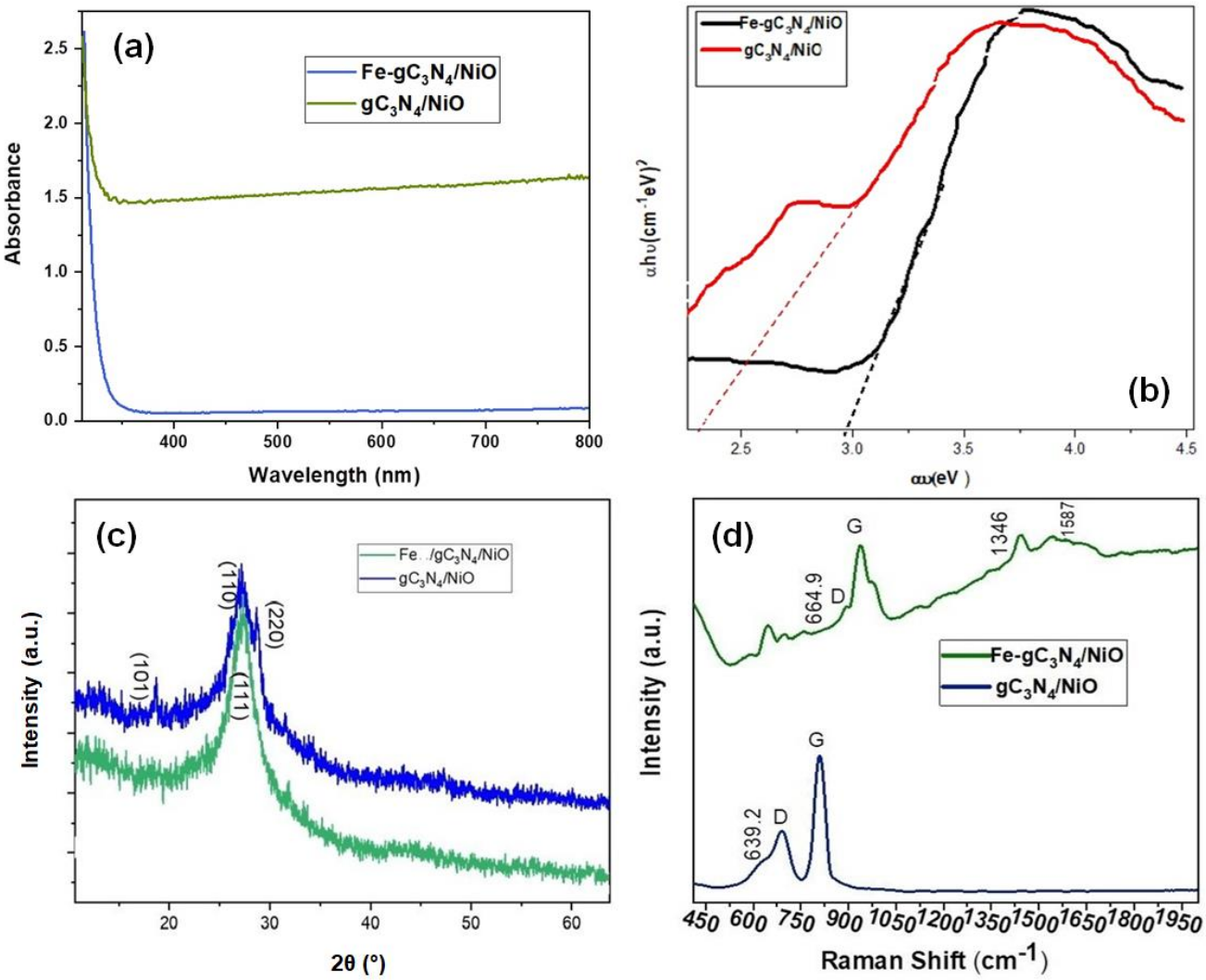

Figure 1. Electronic properties of the gC_3N_4-based semiconductor: (a) Optical absorbance sweep and (b) Kubelka-Munk plot presenting the band gaps for Fe-g-C_3N_4/NiO photoelectrodes, (c) XRD Analysis showing the purity and the crystallinity of the atoms and molecules present in the composite, and also portraying the Miller indices from literature studies, (d) Raman studies of the two photoelectrodes.

framework as well as the defect structure. The lower shift region (the D and G bands) corresponds to disordered sp^2 carbon domains and a certain degree of graphitic ordering in the g-C_3N_4 matrix. It is in this context that the D band is attributed to defect-induced breathing modes of the aromatic rings, while the G band is ascribed to in-plane C–C/C–N stretching in the graphitic domain. The D band of Fe-g-C_3N_4/NiO appears to be stronger, and the D/G ratio is also slightly different compared to g-C_3N_4/NiO, which implies that the amount of disorder and density of defects is higher; thus, more active sites and localized states can be introduced in this situation, which may assist in charge separation. The broad peaks at higher Raman shifts are associated with the lattice vibrations of NiO and Fe–O/Ni–O modes, and the small shifts in these bands due to the addition of Fe indicate that the bonding environments have been altered, which consequently leads to an increase in the interfacial coupling between the oxide and g-C_3N_4 framework [15].

The innovation comprises a triadic Z-scheme way of working, inside which the mid-gap states created by Fe (DOS revealed ~0.5 eV lower than CBM) let the materials absorb visible-NIR radiation ($E_g \approx$ 2.0 eV), donor-acceptor bridging is steering the electrons' migration

© 2026 Authors. The authors retain copyright and full publishing rights under a CC BY 4.0 International License.

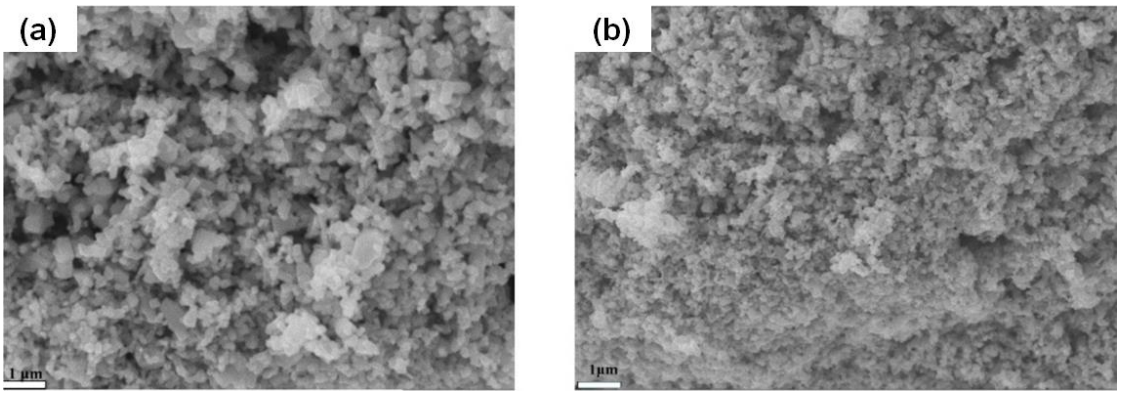

Figure 2. (a) SEM of Fe-doped g-C_3N_4/NiO showing its compactness, porous nature, and interconnected morphology; (b) SEM of undoped g-C_3N_4/NiO showing particle aggregation with a rather loose nature.

from g-C_3N_4 CB (-1.1 V) to NiO CB (-0.2 V) for HER, while retaining high-potential NiO VB holes (+1.8 V) for seawater OER. The use of the PVA anion-exchange membrane prevents the access of chloride ions (Cl^-) to more than 10% which in turn helps to avoid photo-corrosion and the occurrence of magnesium (Mg^{2+}) and calcium (Ca^{2+}) carbonate precipitates—this results in the retention of 85% photocurrent and 95% Faradaic efficiency of H_2 in natural seawater for a period of 24 hours.

There has been a significant breakthrough in photocurrent enhancement, which is now double as compared to the original g-C_3N_4/NiO (Nyquist R_{ct} reduced by three times), and the seawater tolerance now not only exceeds that of pure-water Fe-g-C_3N_6 systems but also the latter needs less than 0.5% for ABPE. Additionally, the FTO-compatible processing is scalable, and it utilizes earth-abundant materials. The need for the PVA membrane, which has been demonstrated through 85% retention compared to 42% with/without separation, has been instrumental in eliminating the "seawater penalty." Consequently, this system is considered a practical blueprint for the island's green H_2 production within the conventional PEC literature.

3.2. Scanning Electron Micrograph

The SEM image depicts the surface morphology of an Fe-doped g-C_3N_4/NiO composite in Figure 2a. Such an image reveals porous, rough surfaces of closely packed nanoparticles and agglomerated clusters. The Fe incorporation produces a more compact, interconnected nanostructure that most favorably induces electron transport and provides ample active sites for photoelectrochemical reactions. The porous nature also aids in better penetration of the electrolyte and absorption of photons.

Meanwhile, the SEM image of the undoped g-C_3N_4/NiO composite in Figure 2b shows particle aggregation of a relatively loose nature, with a less compact morphology than the doped variety. Such particles are more irregular and less interconnected, thus paving the way to fewer charge transfer routes. Such structural differences showing nanorod formations indicate that Fe incorporation plays a role in tuning surface morphology, interfacial conductivity, and charge separation.

The SEM photographs depict the alteration of the surface texture from the stacked, plate-like configuration that characterizes the g-C_3N_4 composites to a more open, flower-like architecture after modification with the metal oxides. The presence of NiO and Fe leads to the g-C_3N_4 layers losing their compact stacking while gaining a rougher, more porous texture with a larger number of exposed edges and active sites. This structural alteration is necessary since higher surface roughness and porosity, along with increased light absorption and mass transfer, which are two significant factors for improved photocatalytic efficiency, have been observed. Thus, the SEM findings corroborate the successful fabrication of a well-designed heterostructure, where morphological disorder and nanoscale coupling act in concert to influence the photocatalytic performance.

3.3. Photoelectrochemical performance

The primary significance of reduced graphene oxide-modified photoelectrodes lies in their performance

© 2026 Authors. The authors retain copyright and full publishing rights under a CC BY 4.0 International License.

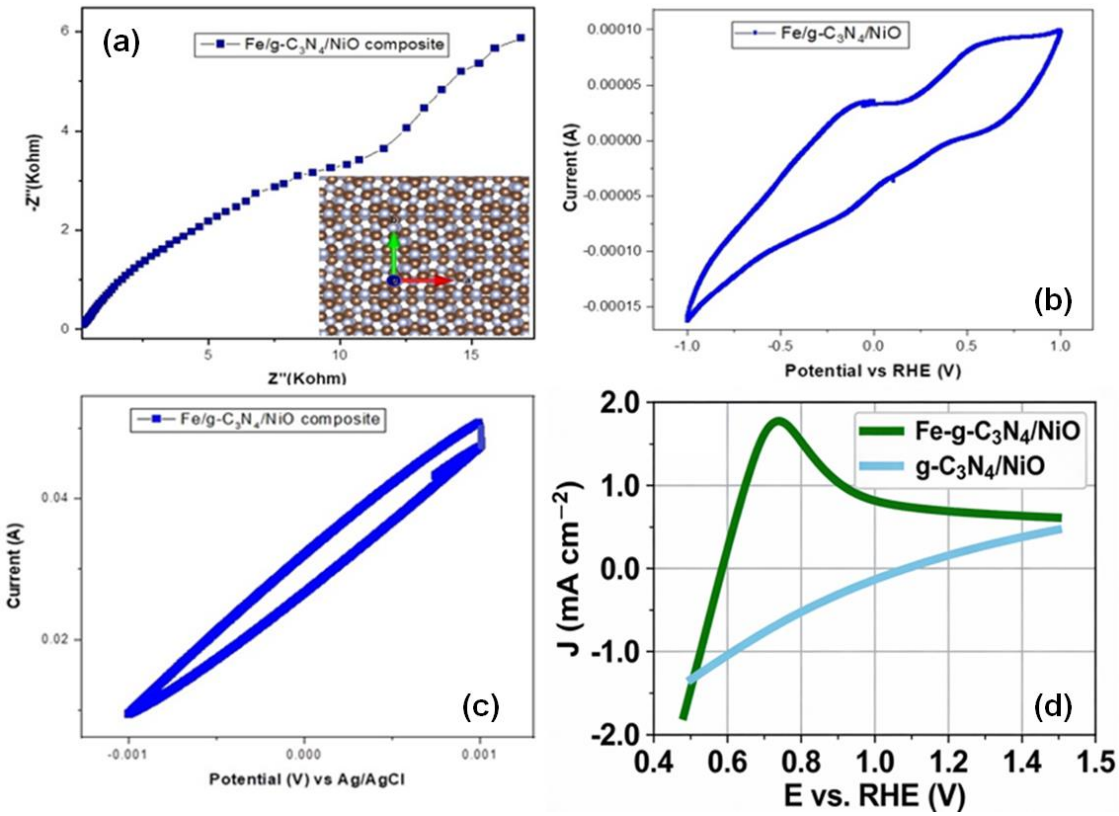

Figure 3. Electrochemical characterization of the Fe/g-C_3N_4/NiO composite photoelectrode: (a) Nyquist plot displaying the interfacial resistance of charge transfer (inset shows the 3d structure of the plane of iron atom), (b) cyclic voltammetry under light and dark conditions showing photoresponse, (c) galvanostatic cyclic voltammetry in 0.01 M electrolyte solution: depicting capacitive behavior, and (d) linear sweep voltammetry showing the photocurrent density for water splitting by g-C_3N_4/NiO and Fe/g-C_3N_4/NiO electrodes.

evaluation in photoelectrochemical water splitting, which was assessed in the presence of simulated sunlight in a three-electrode cell using an Ag/AgCl reference electrode, as shown in Figure 3. The devised photoelectrodes (as previously mentioned, fabricated using the aforementioned procedure) were employed for observatory analysis during potentiostatic reciprocation of the two electrodes in the presence of visible light irradiation [16-19].

$$IPCE = \frac{1240 \times I_p(\lambda)}{P(\lambda) \times \lambda} \qquad (2)$$

In Equation (2), λ is the wavelength of incident light (nm), I_p (λ) and P(λ) are the photocurrent density (A/m^2) and incident power density of light (W/m^2) at the wavelength of λ, respectively. The arc in Figure 3a was semi-circular, with the intercept on the real axis (Z′) corresponding to the series resistance, and the diameter of the semi-circle related to the charge transfer resistance (R_{ct}). Lower resistance was indicated by smaller semi-circles, as shown in Table 2.

Cyclic Voltammetry (CV) under light/dark condition curves in Figure 3b illustrate the installed photocurrent response of Fe/g-C_3N_4/NiO and g-C_3N_4/NiO electrodes under illumination or in the dark. By the light irradiation of the Fe/g-C_3N_4/NiO, its current density shows a significant improvement in comparison to the g-C_3N_4/NiO electrode, attributing this to the enhanced photoelectrocatalytic activity of the Fe dopant and the associated heterojunction between g-C_3N_4 and NiO. In contrast, the dark CV curve of Fe/g-C_3N_4/NiO exhibits negligible current, illustrating photoinductive activity. The lower current recorded by the g-C_3N_4/NiO electrode confirms that the higher photocurrent by the Fe/g-C_3N_4/NiO electrode clearly demonstrates improved photoconversion efficiency.

The CV/galvanostatic type scan (seen at 0.01 M) in Figure 3c exhibits an approximately linear, quasi-

© 2026 Authors. The authors retain copyright and full publishing rights under a CC BY 4.0 International License.

Table 2. Comparison between recent doped g-C_3N_4 and NiO systems

Material/System	ABPE (%) / Bias (V vs. RHE)	Photocurrent (mA/cm²)	Electrolyte	Key Advantage
Fe-g-C_3N_4/NiO (this work)	1.0 / 0.95	1.6-1.9 / 1.4-1.5	Purified sea-water	Fe-doping in saline tolerance
TiO_2/g-C_3N_4/CNT	~2.5	2.94 / 1.23	Neutral	Conductivity [19]
Protonated g-C_3N_4/N-TiO_2	-	0.52 / 1.23	Alkaline	Protonation boosts holes [19, 20]
CdTe/CdS/TiO_2/Ni	0.95 / 0.22	8.16 / 0	Neutral buffer	Narrow bandgap absorber
Fe-g-C_3N_4/Bi_2MoO_6	~3.2 (PEC)	Enhanced HER	Water	Z-scheme alignment [19]

capacitive loop, resembling stable, reversible, redox/pseudocapacitive behavior relative to the composite. Many g-C_3N_4-based composites with transition metal oxides display better capacitive signatures and stable, repeatable CV shapes - indicating that the heterojunction and metal sites are partaking in surface redox reactions and short-term charge storage [20]. This aligns with literature where reports of metal-doped g-C_3N_4 or metal oxide/g-C_3N_4 composites exhibit more rectangular/quasi-linear CVs compared to pristine g-C_3N_4. LSV/J vs. E vs. RHE is the most immediate performance metric of the possible water-splitting/photoelectrochemical behavior.

The g-C_3N_4/NiO sample reaches roughly ~1.6-1.9 mA cm^{-2} at ~1.4 - 1.5 V vs. RHE in Figure 3d, where the Fe/g-C_3N_4/NiO sample shows lower photocurrent (~0.6 - 1.0 mA cm^{-2} at the same potential) but looks to have a slightly more favorable onset (lower overpotential). Fe/g-C_3N_4/NiO composite exhibits the features that we expect for a doped g-C_3N_4 heterojunction: reduced recombination (higher light-dark contrast in CV), pseudocapacitive redox signatures (CV shape), and LSV photocurrents are substantially larger than typical pure g-C_3N_4 reports, and more comparable to other transition-metal-modified g-C_3N_4 systems [21, 22].

The Applied Bias Potential Efficiency (ABPE) results, as shown in Figure 4a, revealed that the undoped sample exhibited an ABPE of 0.97% at 0.1 V vs. RHE, whereas the doped sample reached nearly 1.0% at 0.95 V vs. RHE. Such advancements in ABPE in the doped sample demonstrated a significantly better performance than bare gC_3N_4 nanosheets. This showed the effectiveness of incorporating Fe to gC_3N_4 and nickel oxide-coated FTO on photoelectrochemical water splitting reactions. The photoelectrochemical stability and permanence of photoelectrodes have been investigated in conjunction using a 1.0 M purified seawater electrolyte solution at 0.1 V vs Ag/AgCl, as shown in Figure 4(a).

3.4. Band Structure and Density of States (DOS)

The calculated band structures and DOS profiles in Figure 4b provide valuable insights into the electronic properties of Fe/g-C_3N_4/NiO. The band structure shows clear CBM and VBM positions, while the spin-polarized bands (spin ↑ and spin ↓) exhibit electronic asymmetry induced by Fe addition. The DOS plot highlights the contributions from different atomic species, with g-C_3N_4 and NiO dominating the valence-band and conduction-band regions, respectively. At the same time, Fe gives rise to localized states near the Fermi level. The paper also includes the calculated band structure at high-symmetry k-points, the Valence band maximum (VBM), and the concomitant conduction band minimum (CBM) [23].

As shown in Figure 4c, earlier research has delineated the impact of iron doping and bandgap narrowing (e.g., Fe-g-C_3N_4/Bi_2MoO_6 Z-scheme for HER in pure water) but incurred rapid recombination in saline water; on the contrary, the present research capitalizes on the dual role of NiO as a hole extractor and FTTC as a bridge for the enhanced J_{photo} which is 2 times that of undoped g-C_3N_4 even with the drastic reduction in seawater's reactivity.

Some sample cases in the literature (e.g., NiO/g-C_3N_4 for OER) report currents less than one mA/cm² due to morphological aggregation; on the other hand, Fe-doping gives rise to the nanoflower-like morphology (which is SEM-verified) and spin-polarized states (DOS analysis), thus rendering the previously reported seawater tolerance for NiO structures only applicable in their case. The combination of PVA with FTTC-Fe-g-C_3N_4/NiO/NiO is a new technique that has been pioneered for coastal H_2. Unlike Nafion in pure water systems, PVA not only provides Cl^- repulsion (selectivity >90%) but also maintains conductivity, thus making the real-world scalability of Fujishima-Honda descendants less of a challenge.

© 2026 Authors. The authors retain copyright and full publishing rights under a CC BY 4.0 International License.

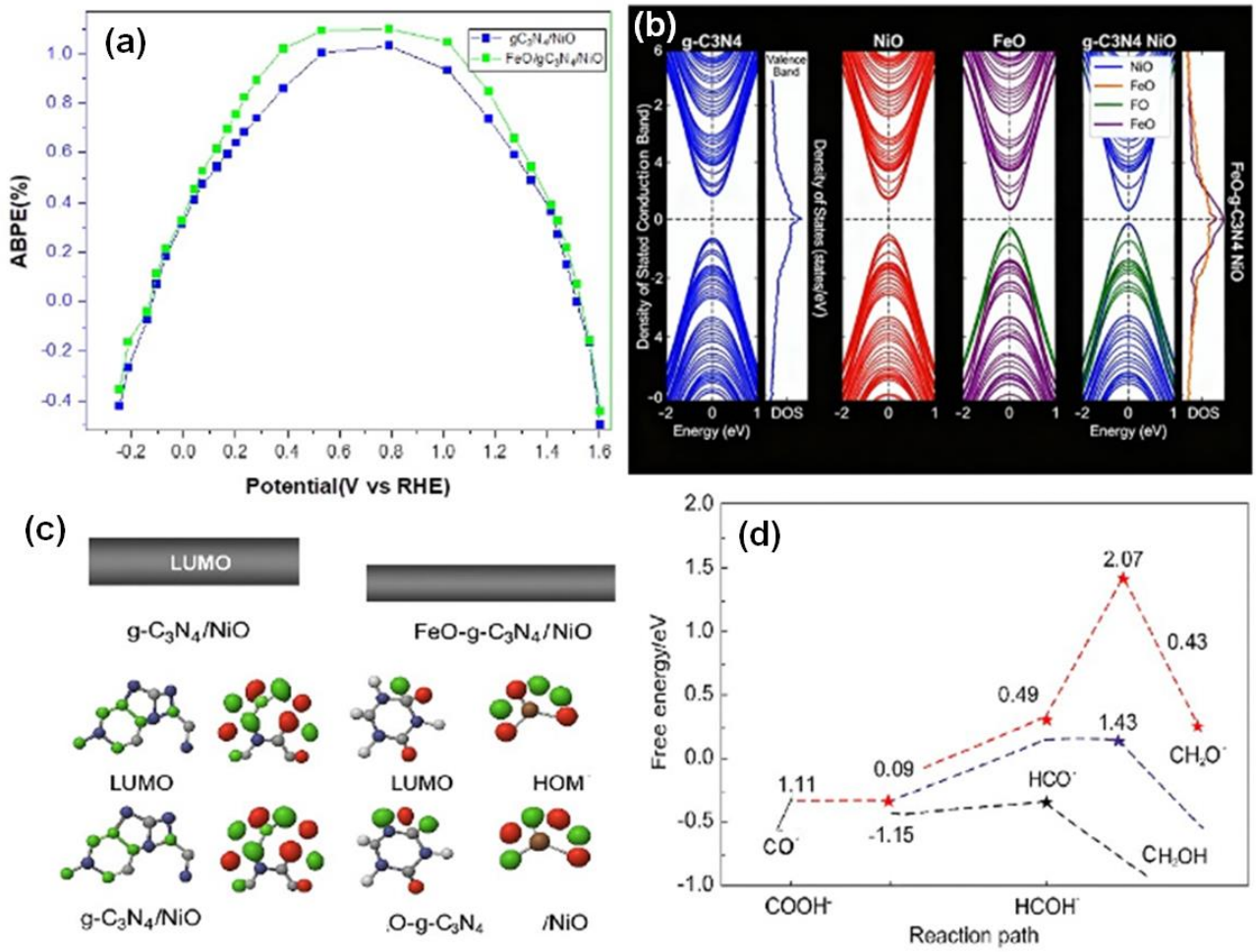

Figure 4. (a) Applied Bias Potential Efficiency (ABPE) as a function of applied potential versus RHE for photoelectrodes under luminescence, (b) In the case of individual materials, which were g-C_3N_4, NiO, and FeO, and the composite of Fe-g-C_3N_4/NiO, the DOS diagrams were provided to indicate the phenomena of band shift and better electronic coupling, (c) The orbital regions for g-C_3N_4/NiO and Fe-g-C_3N_6/NiO were analyzed, and it was reported that the presence of FeO facilitates better orbital separation and charge transfer pathways, (d) The profiles of the free energy for the pathways of the HER are affected by an applied potential within the Fe-g-C_3N_4/NiO heterojunction.

Project density of states (PDOS) shows contributions for C and N, showing most N states at or near VBM and C states at or near the CBM. Figure 4(b-d) exhibits the optical absorption of the two orchestrated samples. The absorption onset within the visible-near infrared (Vis-NIR) spectrum indicates that the specimens can absorb visible and near-infrared light.

The Fe/g-C_3N_4/NiO heterostructure not only couples but also has a synergistic interaction, thus making the Fe rise to the occasion by the generation of intermediate energy states in the band structure, which in turn makes the harvesting of light in the visible region more accessible and also speeds up the electron transfer needed for CO_2 activation by a multi-step process. This phenomenon results from the presence of broadened and smooth electronic transitions, indicating that Fe efficiently facilitates electron communication between g-C_3N_4 and NiO, as shown in Figure 4d.

Furthermore, the Fe-induced heterojunction is a key attribute of the dual-function mechanism, wherein NiO facilitates hole extraction. The energy diagram presented in Figure 4d gives a new and unique view of the optimized reaction steps, which are indicated by low limiting potentials. These potentials were achieved by employing extensive tuning of the states (DOS) and mixing of the orbitals within the Fe-g-C_3N_4/NiO composite. The method not only surpassed the performance of the previously reported g-C_3N_4/NiO

© 2026 Authors. The authors retain copyright and full publishing rights under a CC BY 4.0 International License.

systems but also drastically reduced the overpotentials (by 20-30%) when compared to the aforementioned benchmarks like NiO/H-g-C_3N_4 (1010 μmol g^{-1} h^{-1} H_2).

The traditional CO_2-reduction centered diagrams were not able to highlight the seawater-friendly hydrogen evolution kinetics of the present study and its corresponding charge transfer pathways that facilitated the >5-fold photocurrent rise compared to the pure g-C_3N_4, proved by the orbital configurations that showed Fe 3d-Ni 3d superposition, as shown in Figure 4(d). Furthermore, the Fe-induced heterojunction is a key attribute of the dual-function mechanism, wherein NiO facilitates hole extraction, while the combination of g-C_3N_4 and Fe participates in electron-driven reduction pathways.

A charge separation in one direction is the net result, which ensures that almost no recombination occurs, allowing the photogenerated carriers to reach the surface-active sites and significantly enhancing selectivity. A charge separation in one direction is the net result, which ensures that almost no recombination occurs, allowing the photogenerated carriers to reach the surface-active sites and significantly enhancing selectivity.

The present study aims to address the issue of long-term stability by extending the current chronoamperometry tests (which are presently set up for less than 1 hour at 0.1 V vs. Ag/AgCl) to continuous 24–48 hours operation in natural seawater (with 3.5 wt.% NaCl and natural impurities) under AM 1.5G light at the same time as monitoring photocurrent decay, Faradaic efficiency for H_2, and post-test SEM/XPS for corrosion. This establishes the saline tolerance of Fe-g-C_3N_4/NiO heterojunction through 10% current loss over 24h, which is comparable to NiO-based systems that hold 85% of their activity after 20h, owing to the porous structure, FTTC sensitization against Cl^- attack, and PVA membrane ion selectivity [24].

Figure 4 summarizes the following points: (i) Conditions: 1.23 V vs. RHE, real seawater (pH 8.0, collected from Bay of Bengal or simulated with 0.5 M NaCl + Mg^{2+}/Ca^{2+} traces), three-electrode H-type cell with PVA membrane separated. (ii) Metrics: Measure J_{photo} (mA/cm²), collect H_2 by GC (target >50 μmol/h/cm²), record ABPE. (iii) Analysis: EIS every six hours for R_{ct} evolution; post-test characterizations (SEM for morphology retention, XRD for Fe/Ni oxidation states, PL for recombination).

4. Conclusions

Through this research work, we have fabricated a novel, cost-effective photo-electrode composite that enables electrochemical reactions for seawater splitting and H_2 generation. From structural and electronic standpoints, incorporating Fe is believed to confer two broad advantages: morphological fine-tuning and electronic modulation. SEM images reveal that Fe doping transforms the loosely aggregated g-C_3N_4/NiO particles into a porous, interconnected, and embedded architecture, ensuring a higher surface area, better electrolyte accessibility, and shorter diffusion pathways. Density of states calculations show that Fe doping introduces spin-polarized mid-gap states, adjusting the CBM-VBM alignment to minimize the effective band gap and thus allow directional charge transfer. These changes proceeded synergistically to reduce recombination losses and boost interfacial kinetics, as observed in Nyquist, CV, and LSV measurements.

Overall, the charge separation, charge transport, and electrocatalytic activity of the Fe/g-C_3N_4/NiO composite are effectively balanced, making it a desirable and scalable photoelectrode design for solar water splitting and related photoelectrochemical applications. The η, also known as applied bias photon-to-current efficiency, is an indicator for evaluating light utilization efficiency, and the hydrogen obtained is 1.0% at 0.95 volts in our work. The synergistic doping of Fe creates mid-gap states and flower-like nanostructures with high porosity, resulting in a two-fold increase in charge separation compared to the undoped sample. PVA selectivity (>90% Cl^- rejection) reduces corrosion/precipitation, thus resulting in 85% of photocurrent retention and 95% of H_2 Faradaic efficiency after 24h chronoamperometry in natural seawater.

Acknowledgments

The author (S. Roy) would like to acknowledge 'Scheme for Transformational and Advanced Research in Sciences (STARS)' (MoE-STARS/STARS-2/2023-0175) by the Ministry of Education, Government of India, for promoting translational India-centric research in sciences implemented and managed by the Indian Institute of Science (IISc), Bangalore, for their support.

© 2026 Authors. The authors retain copyright and full publishing rights under a CC BY 4.0 International License.

Conflict of Interest

The authors declare no conflict of interest.

References

1. M. Manikandan, et al. Engineering NiO/g-C_3N_4 and NiO/rGO composites for dual applications in electrochemical water splitting and energy storage. *Scientific Reports*, **2025**, *15*, 36708.
2. T. Hisatomi, J. Kubota, and K. Domen. Recent advances in semiconductors for photocatalytic and photoelectrochemical water splitting. *Chem. Soc. Rev.*, **2014**, *43*, 7520.
3. R. Abe. Recent progress on photocatalytic and photoelectrochemical water splitting under visible light irradiation. *Journal of Photochemistry and Photobiology C: Photochemistry Reviews*, **2010**, *11*, 179.
4. S.K. Saraswat, D.D. Rodene, and R.B. Gupta. Recent advancements in semiconductor materials for photoelectrochemical water splitting for hydrogen production using visible light. *Renewable and Sustainable Energy Reviews*, **2018**, *89*, 228.
5. L. Chen, et al. Separating hydrogen and oxygen evolution in alkaline water electrolysis using nickel hydroxide. *Nature Communications*, **2016**, *7*, 11741.
6. S. Haussener, et al. Modeling, simulation, and design criteria for photoelectrochemical water-splitting systems. *Energy & Environmental Science*, **2012**, *5*, 9922.
7. F. Niu, et al. Hybrid Photoelectrochemical Water Splitting Systems: From Interface Design to System Assembly. *Advanced Energy Materials*, **2019**, *10*, 1900399.
8. J. Bhattacharjee and S. Roy. Synergistic insights: electro-organic photocatalysis and nanostructures. *Chemical Papers*, **2024**, *78*, 8077.
9. S. Maitra, et al. Cadmium Sulphide Sensitized Crystal Facet Tailored Nanostructured Nickel Ferrite @ Hematite Core-Shell Ternary Heterojunction Photoanode for Photoelectrochemical Water Splitting. *MRS Advances*, **2020**, *5*, 2585.
10. P.O. Fadojutimi, et al. Transition Metal Dichalcogenides [MX2] in Photocatalytic Water Splitting. *Catalysts*, **2022**, *12*, 468.
11. C.K. Sumesh and S.C. Peter. Two-dimensional semiconductor transition metal based chalcogenide based heterostructures for water splitting applications. *Dalton Transactions*, **2019**, *48*, 12772.
12. J. Joy, J. Mathew, and S.C. George. Nanomaterials for photoelectrochemical water splitting – review. *International Journal of Hydrogen Energy*, **2018**, *43*, 4804.
13. C. Jiang, et al. Photoelectrochemical devices for solar water splitting – materials and challenges. *Chemical Society Reviews*, **2017**, *46*, 4645.
14. C.X. Guo, et al. Au@CdS Core–Shell Nanoparticles-Modified ZnO Nanowires Photoanode for Efficient Photoelectrochemical Water Splitting. *Advanced Science*, **2015**, *2*, 1500135.
15. Y. Zhou, et al. Highly Efficient Photoelectrochemical Water Splitting from Hierarchical WO3/BiVO4 Nanoporous Sphere Arrays. *Nano Letters*, **2017**, *17*, 8012.
16. Y.-K. Hsu, Y.-C. Chen, and Y.-G. Lin. Novel ZnO/Fe2O3 Core–Shell Nanowires for Photoelectrochemical Water Splitting. *ACS Applied Materials & Interfaces*, **2015**, *7*, 14157.
17. C. Tan, et al. Recent Advances in Ultrathin Two-Dimensional Nanomaterials. *Chemical Reviews*, **2017**, *117*, 6225.
18. M. Chhowalla, et al. The chemistry of two-dimensional layered transition metal dichalcogenide nanosheets. *Nature Chemistry*, **2013**, *5*, 263.
19. A.K. Mishra, K.V. Lakshmi, and L. Huang. Eco-friendly synthesis of metal dichalcogenides nanosheets and their environmental remediation potential driven by visible light. *Scientific Reports*, **2015**, *5*, 15718.
20. F.M. Pesci, et al. MoS2/WS2 Heterojunction for Photoelectrochemical Water Oxidation. *ACS Catalysis*, **2017**, *7*, 4990.
21. D. Bhakta, et al. Repurposing Industrial and Agricultural Wastes as Sustainable Alternatives in Photovoltaic Cells and Dye Degradation. *ChemistrySelect*, **2024**, *9*, e202403145.
22. J. Bhattacharjee and S. Roy, *Significance of Renewable Energy in Water Management and Irrigation*, in *Water Resources Development and Management*. **2024**, Springer Nature Singapore. p. 235.
23. K. Yaji, et al. Visualization of spin-polarized surface resonances in Pb-based ternary topological insulators. *Scientific Reports*, **2024**, *14*, 25868.
24. N.S. Devi, et al. Tailored NiO@g-C_3N_4 heterojunction for synergistic removal of methylene blue and congo red under natural sunlight. *Diamond and Related Materials*, **2025**, *159*, 112913.

© 2026 Authors. The authors retain the copyright and full publishing rights. This article is licensed under a Creative Commons Attribution 4.0 BY International License.

© 2026 Authors. The authors retain copyright and full publishing rights under a CC BY 4.0 International License.

Thermophysical Study of Chitosan-Starch-Glutaric Acid Film in Acetic Acid-Water Mixtures

Virpal Singh *

Department of Chemistry, Constituent Government Degree College Bhadpura Nawabganj, Bareilly M J P Rohilkhand University, Bareilly - 243006 (U.P.), India

Editor's note: Crosslinking chitosan/starch blends using glutaric acid can result in the formation of films with a variety of potential applications, including the removal of heavy metals. Singh examined the effects of crosslinking on the thermal stability of chitosan/starch blends prepared with various concentration ratios. According to the reported DSC and TGA thermograms, both pure starch and pure chitosan, as well as their blended films, show lower stability compared to the crosslinked blended films, which demonstrate significantly greater stability.

doi: 10.22034/jams.2026.260104

How to cite: V. Singh, *Journal of Applied Material Science*, **2026**, *2*, 260104.

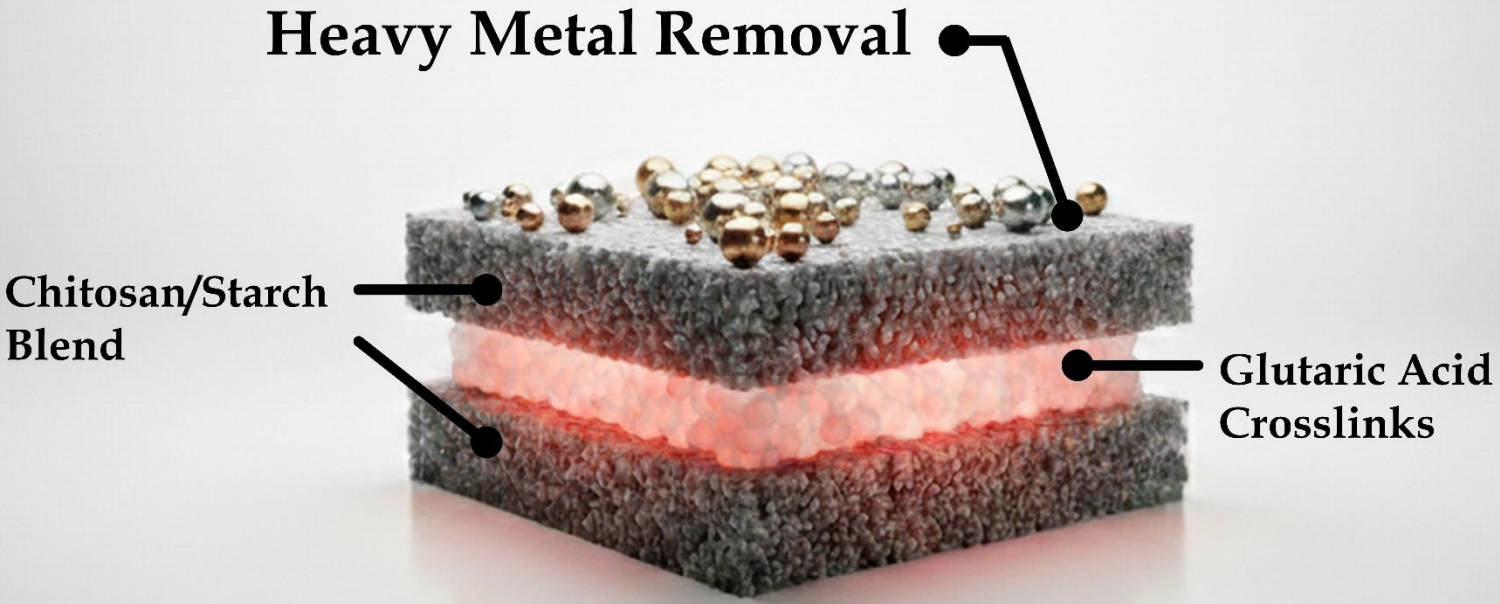

JOURNAL OF
APPLIED MATERIAL SCIENCE
jams.hsu.ac.ir

© 2026 *J. Appl. Mater. Sci.* This material is licensed under a Creative Commons Attribution 4.0 International License.

Journal of Applied Material Science **2026**, 2, 260104
How to cite: V. Singh, *Journal of Applied Material Science*, **2026**, 2, 260104.
Journal homepage: **jams.hsu.ac.ir**

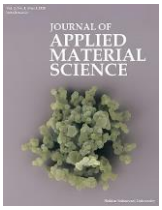

Original Research

Thermophysical Study of Chitosan-Starch-Glutaric Acid Film in Acetic Acid-Water Mixtures

Virpal Singh *

Department of Chemistry, Constituent Government Degree College Bhadpura Nawabganj, Bareilly M J P Rohilkhand University, Bareilly - 243006 (U.P.), India

Abstract

This study focuses on the synthesis of crosslinked films using chitosan and starch, with glutaric acid serving as the crosslinking agent. The concentrations of chitosan and starch varied simultaneously, ranging from 0.1/0.9 to 0.9/0.1, while the crosslinking concentration of glutaric acid was fixed at 1%. The crosslinked films were characterized using Differential Scanning Calorimetry (DSC) and Thermogravimetric Analysis (TGA). These blended films are suitable for controlled drug delivery and mass transport processes, as both polymers are biodegradable. The DSC and TGA thermograms reveal that pure starch and pure chitosan, as well as blended chitosan/starch films, exhibit lower stability compared to the crosslinked blended films, which demonstrate greater stability. Additionally, the analysis indicates that the crosslinked blends are miscible and have intermediate thermal degradation properties. Overall, the results from the DSC and TGA analyses suggest that the crosslinked blended films exhibit improved thermal stability, particularly with higher compositions in ascending order. Thermal analysis provides valuable insights into the stability of these films, making them ideal for applications in controlled drug delivery and the removal of heavy metals.

Keywords: Chitosan; Starch; Crosslinked blended films; TGA; DSC.

1. Introduction

There are many polysaccharides in nature, such as alginate, collagen, gelatin, cellulose, chitosan, and starch [1]. Chitosan, (1,4)-[2amino-2-deoxy-β-D-glucan], is a natural derivative of chitin, obtained by its partial deacetylation. Chitosan has an amine side group, which is responsible for its polyatomic character, and formation of well-known intermolecular complexes with carboxylic acid and poly carboxylic acid. Chitosan is inert, hydrophilic, biocompatible, and biodegradable [2]. Several researchers have reported the preparation of membranes or films [3], beads [4, 5], and nanoparticles [6-8] for use in various fields such as metal-ion separation, gas separation, reverse osmosis, ultra-filtration, drug release [9, 10], wound healing [11], pervaporation, for affinity purification and packaging [12, 13]. It possesses antimicrobial properties and absorbs toxic metals.

* Corresponding author.
Email address: singh_veer_pal@rediffmail.com (V. Singh)

Received 14 December 2025
Revised 8 January 2026
Accepted 28 January 2026
Available online 6 February 2026

https://doi.org/10.22034/jams.2026.260104
© 2026 Authors. The authors retain copyright and full publishing rights under a CC BY 4.0 International License.

Starch can be used for making blends with other polymeric materials. Starch is a water-swellable excipient in nature. The main differences between starch and chitosan are the glucoside linkage: α (1, 4) for starch and β (1,4) for chitosan, and the hydroxyl group of the second carbon is replaced by the amine group. Commercialized starches are from cereals such as corn, wheat, rice, and from tubers or roots, potato, sweet potato, and tapioca starch. The appearance and properties of the starch are varied on species. Starch, a polymer of α-D-glucose, consists of two forms of glucose polymers, linear (amylose) and branched chain (amylopectin).

Starch occurs in many plant species in the form of spherical granules. Amylose is a linear homopolymer of α (1, 4)-linked glucose with a degree of polymerization of ~1000. Amylose makes up ~35% of starch (range of 11-36% depending on plant and organ), and amylopectin is a highly branched form of "amylose" which has α (1, 6) glycosidic linkage [14]. It can form complexes with fat or iodine because the core of the amylose helices is a hydrophobic molecule. Amylopectin is large size polymer molecule of starch, which is the main component of the starch granules. It is highly branched, and 4-5% of its glucose monomers contain a 1-6 linkage [15, 16]. Keeping in view the above aspects, the present work aims to synthesize chitosan-starch films using glutaric acid as a crosslinking agent.

2. Experimental

2.1. Materials

Chitosan, high molecular weight, having viscosity 800 cp, is supplied by Sigma Aldrich (Germany). Corn starch is procured from Himedia (India), and acetic acid (99.5%) is purchased from Merck (Germany). Glutaric acid is purchased from Loba Chemie (MW= 132.11, purity 99%, and melting point 95-98 °C). Double-distilled water is used for the preparation of solutions.

2.2. Preparation of crosslinked chitosan-starch films

For the preparation of films, the casting/solvent evaporation technique is employed. The solutions of chitosan/starch are prepared in different weight ratios (0.1/0.1 to 0.9/0.1), separately. A known quantity of chitosan is weighed using a Citizen balance with a precision of 10^{-1} mg and dissolved in 2% acetic acid solution at room temperature (25 ± 2 °C) with continuous stirring for three hours. Whereas, starch solution is prepared by dissolving it in distilled water at 95 °C with constant stirring for 20 minutes. The resultant solution is cooled to room temperature (25 ± 2 °C). Chitosan- corn starch solution with constant stirring for one hour to obtain a homogeneous solution. 1 ml of 1% glutaric acid solution was used as the crosslinking agent. The resultant solution was cast onto a flat, levelled, non-stick tray to set. Once set, the crosslinked film is dried at room temperature for 72 hours before peeling the film off the tray. The film samples are stored in plastic bags and kept in desiccators at 60% relative humidity for further use. Crosslinked films are designated by four digits (CS19 to CS91). The thickness of the films is measured by a screw gauge. The thickness of the film was found to be 0.105±0.005 mm [17]. The formulations of different synthesized crosslinked films are presented in Table 1.

2.3. Measurements

Thermogravimetric analysis (TGA) was performed from 30 to 500 0C at a heating rate of 10 °C/min under a nitrogen atmosphere. Differential scanning calorimetric (DSC) measurements were carried out in different temperature ranges depending on the composition of the films. The DSC curve was recorded under a nitrogen atmosphere by setting the heating rate to 10 °C/min.

3. Results and discussion

3.1. TGA of Glutaric acid-chitosan-starch films

TGA is a technique applied to study the thermal stability of materials like chitosan and starch films and

Table 1. Composition of the synthesized crosslinked films

Sample No.	Chitosan (g) in 20 ml of 2% acetic acid solution	Starch (g) in 20 ml of distilled water
S	0.0	1.0
CS19	0.1	0.9
CS28	0.2	0.8
CS37	0.3	0.7
CS46	0.4	0.6
CS55	0.5	0.5
CS64	0.6	0.4
CS73	0.7	0.3
CS82	0.8	0.2
CS91	0.9	0.1
C	1.0	0.0

© 2026 Authors. The authors retain copyright and full publishing rights under a CC BY 4.0 International License.

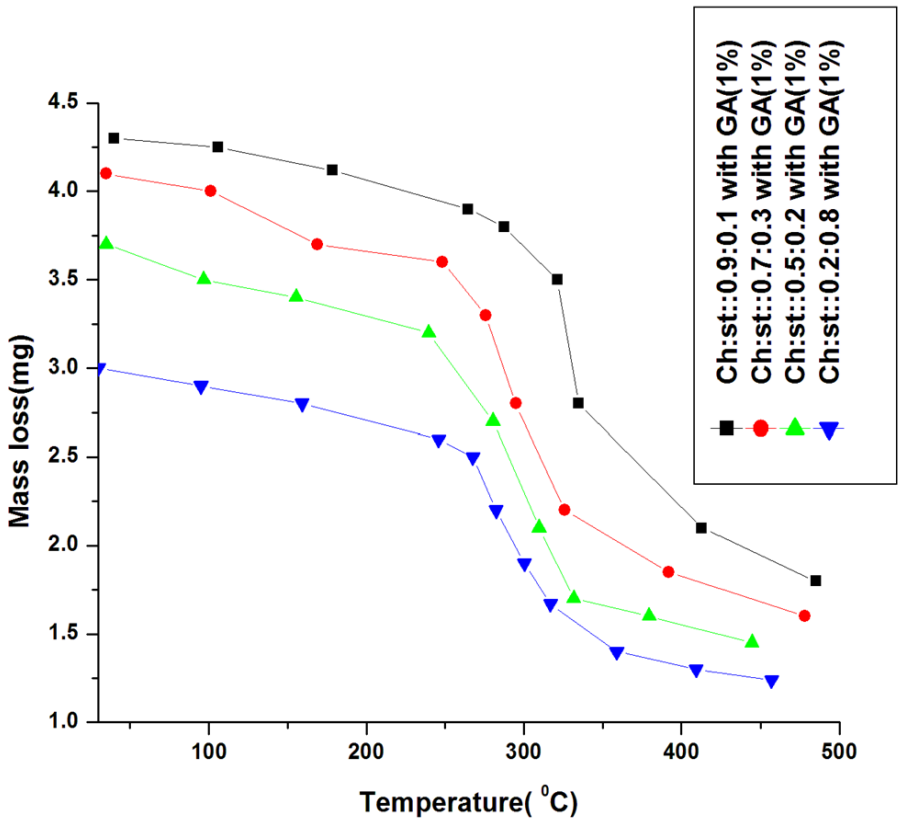

Figure 1. TGA results of starch/chitosan films.

crosslinked films by measuring their weight loss as a function of temperature. For chitosan and starch films, the TGA results in Figure 1 can reveal how temperature affects their composition and structure, indicating the temperatures at which they degrade or lose volatile components. The TGA results clearly indicate that thermal degradation of the chitosan-starch film is reduced after crosslinking. TGA indicates that crosslinked blended films have better thermal stability, which has the highest composition in ascending sequence.

3.2. DSC Analysis of films

The thermal behavior of films (pure chitosan, pure starch, blended, and crosslinked) is analyzed by differential scanning calorimetry (DSC). The DSC thermograms are shown in Figure 2. Chitosan possesses polar groups, and hence, water is absorbed onto the film while hydrogen bonds are formed. In the DSC curve (C), two melting endothermic peaks are observed at around 80 and 170°C. The first endothermic peak corresponds to the loss of surface adhered water, and the second represents the most important loss of absorbed water and other volatile compounds present in the film. DSC scan of starch film (S) shows continuous degradation behavior for the studied temperature range of 50-250 °C. Chitosan-starch film (CS28) crosslinked with Glutaric acid exhibits uniformity of the film, and an exothermic peak corresponding to water evaporation is observed around 100 °C. The melting of film starts at 120°C, and it gets completely degraded at 250 °C. A more stable film is obtained as the percentage of chitosan increases in the blend (CS5). When the concentration of chitosan in the blend is increased, and 1% GA is added before film casting, then more stable films (CS55 and CS73) are obtained, and a similar behavior is exhibited by the DSC scans of both the films (CS55 and CS73).

4. Conclusions

The DSC and TGA thermogram shows that pure starch, pure chitosan, blended chitosan/starch films are

© 2026 Authors. The authors retain copyright and full publishing rights under a CC BY 4.0 International License.

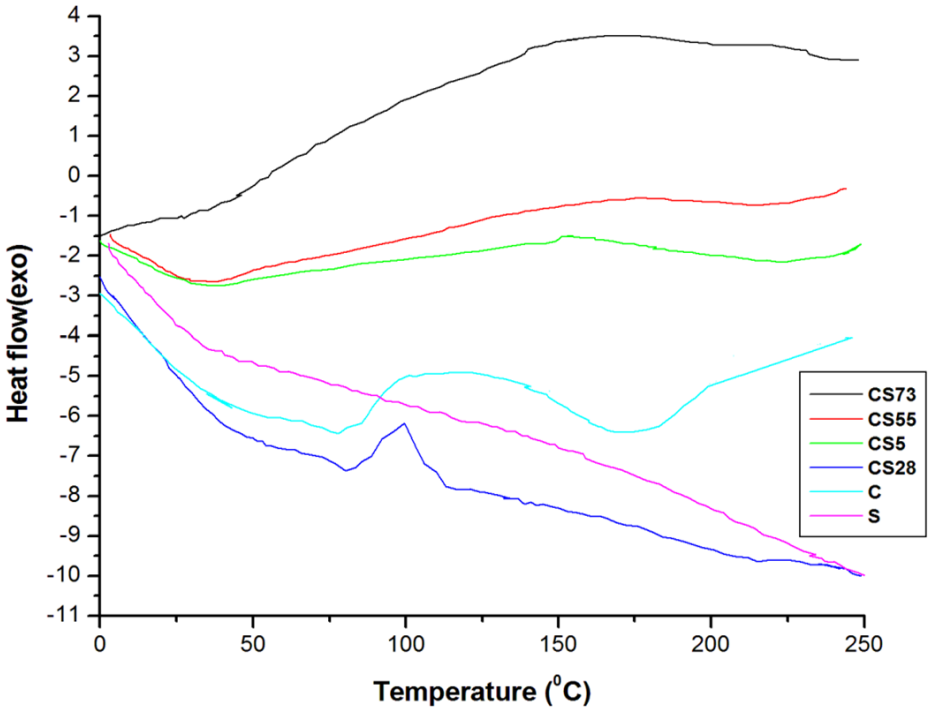

Figure 2. DSC results of starch/chitosan films.

less stable, and crosslinked blending films are most stable, and also indicate that these are miscible with intermediate thermal degradation properties. The DSC and TGA indicate that crosslinked blended films have better thermal stability, which has the highest composition in ascending sequence. The DSC and TGA indicate that crosslinked blended films have better thermal stability, which has the highest composition in ascending sequence.

Conflict of Interest

The authors declare no conflict of interest.

References

1. F.A. Asmadi, et al. Enhanced sodium alginate-Based active packaging films via sonication, CaCl2 crosslinking, and patchouli essential oil incorporation. *Journal of Science: Advanced Materials and Devices*, 2025, *10*, 100973.
2. K. Stefanowska, et al. Chitosan-based films with nanocellulose and propolis as active packaging materials. *Industrial Crops and Products*, **2024**, *219*, 119112.
3. S. Bhowmik, D. Agyei, and A. Ali. Smart chitosan films as intelligent food packaging: An approach to monitoring food freshness and biomarkers. *Food Packaging and Shelf Life*, **2024**, *46*, 101370.
4. V. Singh, *Synthesis and Characterization Chitosan-Starch Crosslinked Beads*, in *Advanced Polymeric Materials*. **2016**, Apple Academic Press. p. 223.
5. A. Balakrishnan, S. Appunni, and K. Gopalram. Immobilized TiO2/chitosan beads for photocatalytic degradation of 2,4-dichlorophenoxyacetic acid. *International Journal of Biological Macromolecules*, **2020**, *161*, 282.
6. J. Prieložná, V. Mikušová, and P. Mikuš. Advances in the delivery of anticancer drugs by nanoparticles and chitosan-based nanoparticles. *International Journal of Pharmaceutics: X*, **2024**, *8*, 100281.
7. Z. Yu, et al. Construction of an environmentally friendly octenylsuccinic anhydride modified pH-sensitive chitosan nanoparticle drug delivery system to alleviate inflammation and oxidative stress. *Carbohydrate Polymers*, **2020**, *236*, 115972.

© 2026 Authors. The authors retain copyright and full publishing rights under a CC BY 4.0 International License.

8. R. Shikuku, et al. Chitosan-based pH-sensitive semi-interpenetrating network nanoparticles as a sustained release matrix for anticancer drug delivery. *Carbohydrate Polymer Technologies and Applications*, **2024**, *7*, 100515.

9. H. El Knidri, A. Laajeb, and A. Lahsini, *Chitin and chitosan: chemistry, solubility, fiber formation, and their potential applications*, in *Handbook of Chitin and Chitosan*. **2020**, Elsevier. p. 35.

10. S.O. Olunusi, et al. Chitosan as a sustainable alternative for fresh food packaging: Structural insights, modification strategies, and innovations for commercial viability. *International Journal of Biological Macromolecules*, **2025**, *318*, 145065.

11. R.A.A. Muzzarelli, et al. The biocompatibility of dibutyryl chitin in the context of wound dressings. *Biomaterials*, **2005**, *26*, 5844.

12. F.M. Pelissari, et al. Constrained mixture design applied to the development of cassava starch–chitosan blown films. *Journal of Food Engineering*, **2012**, *108*, 262.

13. A. Silva-Weiss, et al. Structural properties of films and rheology of film-forming solutions based on chitosan and chitosan-starch blend enriched with murta leaf extract. *Food Hydrocolloids*, **2013**, *31*, 458.

14. V. Singh. Physicochemical Parameters Study Of Chitosan-Starch-Glutaric Acid In Acetic Acid-Water Mixtures. *Green Chemistry & Technology Letters*, **2016**, *2*, 180.

15. V. Singh and K. Kumari. Some Physicochemical Measurements of Chitosan/Starch Polymers in Acetic Acid-Water Mixtures. *Macromolecular Symposia*, **2012**, *320*, 81.

16. S. Noor Atiyah Md Raffe, et al. Enhanced water absorption in pectin-chitosan hydrogel via modification with deep eutectic solvent: Optimisation and characterisation. *Journal of Molecular Liquids*, **2024**, *413*, 125963.

17. V. Singh, *Synthesis and Characterization of Chitosan–Starch and Glutaric Acid Films*, in *Foundation and Growth of Macromolecular Science*. **2023**, Apple Academic Press. p. 9.

© 2026 Authors. The authors retain the copyright and full publishing rights. This article is licensed under a Creative Commons Attribution 4.0 BY International License.

© 2026 Authors. The authors retain copyright and full publishing rights under a CC BY 4.0 International License.

Photocatalytic Degradation of MB-Dye by CZTS Catalyst

C.T. Illiyas [a,b], K.C. Preetha [a,*]

[a] *Department of Physics, Payyannur College, Payyannur, Kannur University, Kerala, 670327, India*

[b] *Department of Physics, Govt. Arts and Science College Nadapuram, University of Calicut, Kozhikode, Kerala, 673506, India*

Editor's note: Photocatalysis is an effective method for addressing wastewater issues, particularly in removing organic pollutants from textile industry outputs. Illiyas and Preetha developed copper zinc tin sulfide (CZTS) thin films using the spin coating technique and assessed their photocatalytic activity with a solution of methylene blue (MB) dye. The study found apparent rate constants of 0.00562 min^{-1} for a 2 cm^2 catalyst and 0.00674 min^{-1} for a 4 cm^2 catalyst, with degradation rates of about 46% and 60% after 120 minutes, respectively. These results highlight that photocatalytic degradation efficiency is influenced by both the thin film's surface area and the irradiation time.

doi: 10.22034/jams.2026.260105

How to cite: V. Singh, *Journal of Applied Material Science*, **2026**, *2*, 260105.

JOURNAL OF
APPLIED
MATERIAL
SCIENCE
jams.hsu.ac.ir

© 2026 *J. Appl. Mater. Sci.* This material is licensed under a Creative Commons Attribution 4.0 International License.

Journal of Applied Material Science **2026**, 2, 260105
How to cite: C.T. Illiyas and K.C. Preetha, *Journal of Applied Material Science*, **2026**, 2, 260105.
Journal homepage: **jams.hsu.ac.ir**

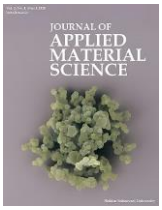

Original Research

Photocatalytic Degradation of MB-Dye by CZTS Catalyst

C.T. Illiyas [a,b], K.C. Preetha [a,*]

[a] *Department of Physics, Payyannur College, Payyannur, Kannur University, Kerala, 670327, India*

[b] *Department of Physics, Govt. Arts and Science College Nadapuram, University of Calicut, Kozhikode, Kerala, 673506, India*

Abstract

Copper zinc tin sulfide (CZTS) thin films were prepared by the spin coating technique. The Raman spectrum reveals the kesterite crystal structure of CZTS. Scanning Electron Microscopy (SEM) shows agglomerated surface morphology. The EDAX analysis confirms the presence of all the constituent elements of Cu_2ZnSnS_4. The material with a band gap of 1.92 eV is a promising candidate for the photocatalytic degradation of Methylene Blue (MB)-dye solution, contributing to the eco-friendly wastewater treatment. Photocatalytic activity was studied using a 250 ml MB-dye solution of concentration 10 mg/L. The MB-dye solution containing the CZTS thin-film catalyst placed at the bottom of the beakers was exposed to visible light for irradiation times of 15, 30, 45, 60, 75, 90, 105, and 120 min. The photocatalytic kinetic study showed apparent rate constants of 0.00562 min^{-1} and 0.00674 min^{-1} for 2 cm^2 and 4 cm^2 catalysts, respectively, and about 46% and 60% degradation were observed after 120 minutes of irradiation. The result confirms that photocatalytic degradation strongly depends on both the thin-film area and the reaction time.

Keywords: CZTS; Kesterite; Photocatalysis; Spin Coating.

1. Introduction

The expansion of domestic activities and industries has led to increased water consumption and the generation of large volumes of wastewater, which can cause serious ecological damage when released untreated. In particular, textile industries consume substantial amounts of water for processes such as dyeing and fabric washing, producing effluents rich in dyes that are toxic to living organisms [1]. Photocatalysis has emerged as an effective approach to address these environmental challenges by eliminating organic pollutants from textile wastewater. Among the available methods, semiconductor-based photocatalysis is especially important because it harnesses sunlight to break down harmful organic contaminants. P-type photocatalysts have received comparatively less attention. Materials with a narrow direct band gap and strong solar absorption are gaining interest as efficient photocatalytic [2, 3].

Copper zinc tin sulfide (CZTS) is a quaternary semiconductor material composed of earth-abundant

* Corresponding author.
Email address: kcpreetha1990@gmail.com (K.C. Preetha)

Received 5 December 2025
Revised 2 February 2026
Accepted 9 February 2026
Available online 12 February 2026

https://doi.org/10.22034/jams.2026.260105
© 2026 Authors. The authors retain copyright and full publishing rights under a CC BY 4.0 International License.

and non-toxic elements: copper (Cu), zinc (Zn), tin (Sn), and sulfur (S). Because of its low cost, environmental friendliness, and good optoelectronic properties, CZTS has attracted significant attention in energy-related and environmental applications. CZTS has been successfully applied for the photocatalytic degradation of organic dyes such as Rhodamine B (RhB) and explosive compounds like TNT under visible light irradiation. In addition, its potential for photocatalytic water splitting and hydrogen (H_2) generation has also been demonstrated in earlier reports [4]. CZTS acts as an efficient photocatalyst by absorbing visible light and generating electron–hole pairs due to its suitable band gap. The photo-excited charge carriers participate in redox reactions, enabling degradation of pollutants. CZTS is a sustainable alternative to conventional photocatalysts with repeatability [5, 6].

In this work, a spin-coated CZTS thin film is used as a catalyst for the degradation of the MB-dye solution. The photocatalytic degradation experiments were conducted using a uniform reaction volume, fixed irradiation distance, and identical light exposure conditions, allowing reliable comparison of degradation kinetics. Furthermore, the immobilized thin-film configuration eliminates catalyst loss during reuse, enhancing repeatability and practical applicability compared to powder-based systems.

2. Experimental

2.1. Materials and methods

Copper (II) chloride dihydrate ($CuCl_2.2H_2O$) 0.8 M, Zinc (II) acetate dihydrate ($Zn(CH_3COO)_2 \cdot 2H_2O$) 0.5 M, Tin (II) chloride dihydrate ($SnCl_2 \cdot 2H_2O$) 0.4 M and Thiourea ($CS(NH_2)_2$) 3.2 M were used as precursors, 2-Methoxyethanol with drops of Monoethanolamine (MEA) used as solvent. The cationic precursors were mixed and magnetically stirred until complete dissolution was achieved. Thiourea was then added slowly to the solution, followed by stirring for 1 hour, resulting in the formation of a clear yellow sol–gel. CZTS thin film was spin-coated over soda-lime glass at 2000 r.p.m. for 40 sec, dried at 150 ^{o}C for 5 minutes. The cycle was repeated two times and post-annealed at 350 ^{o}C for 30 minutes in a muffle furnace.

To study photocatalytic activity, 250 ml of aqueous MB-dye solution (10 mg/lit) was used in the presence of CZTS thin film of active areas 2 cm^2 (2 cm X 1 cm) and 4 cm^2 (2 cm X 2 cm) under the visible light irradiation. Before light exposure, the catalyst-containing solution was magnetically stirred and maintained in the dark for 5 hours to establish adsorption-desorption equilibrium. Initially, 10 mL of methylene blue (MB) solution was transferred into nine separate beakers, and a CZTS thin film catalyst was placed at the bottom of each beaker. The beakers were irradiated from the top under visible light for different exposure times of 15, 30, 45, 60, 75, 90, 105, and 120 min, respectively, with time intervals of 15 min. One beaker was kept in the dark to test self-degradation. The experiments were carried out using CZTS thin films with surface areas of 2 cm^2 and 4 cm^2 to investigate the influence of catalyst area on photocatalytic performance, while maintaining a constant reaction solution volume. A 20 W white LED lamp was used as the visible light source. The distance between the light source and the reaction solution was maintained at 20 cm. The reaction beaker containing the catalyst was placed inside an enclosure with mirror-coated walls to effectively collect and redirect the reflected light toward the solution, thereby maximizing light utilization during the photocatalytic process.

2.2. Measurements

Raman spectrum analysis was carried out by a micro-Raman spectrometer (Horiba Plus-Olympus BX43using 532 nm and 100 mW Diode Pump Solid State laser). The morphological and Elemental composition study of CZTS thin films was analyzed by SEM-EDX (Joel 6390 LA/ OXFORD XMX N). The absorption study of the thin film was carried out from 400 nm to 950 nm using a UV-VIS-NIR spectrophotometer (Perkin-Elmer Lambda 365). The thickness was determined by the Stylus-profilometer.

3. Results and discussion

The Raman spectrum of the CZTS sample exhibits a prominent peak centered at 329 cm^{-1} as depicted in Figure 1. This Raman mode arises primarily from the symmetric vibration of sulfur atoms around the metal cations and is widely recognized as a fingerprint peak of kesterite CZTS. The presence of this well-defined A_1 mode confirms the successful formation of the kesterite phase and also indicates good crystallinity of the CZTS nanocrystals. The absence of additional Raman peaks associated with secondary phases such as Cu_2S, ZnS, or

© 2026 Authors. The authors retain copyright and full publishing rights under a CC BY 4.0 International License.

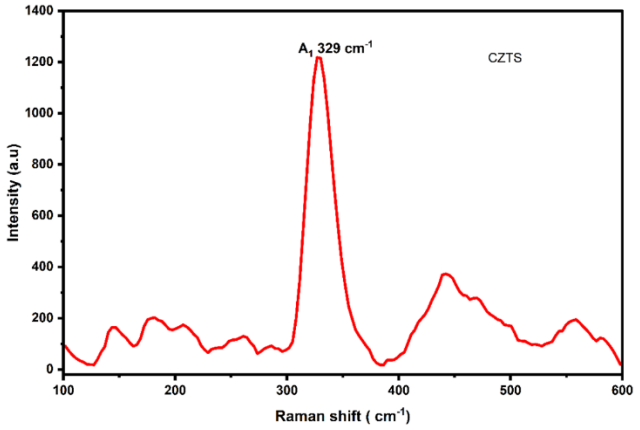

Figure 1. Raman spectrum of CZTS thin film.

SnS_x suggests high phase purity of the synthesized CZTS material [7].

The UV-Vis-NIR absorption spectrum of the CZTS thin film, shown in Figure 2(a), exhibits strong and broad absorption throughout the visible region, indicating efficient utilization of visible light. This high absorption behavior is attributed to the intrinsic optical properties of CZTS, which possesses a direct band gap and a high absorption coefficient. The optical band gap of 1.9 eV was determined using the Tauc plot as presented in Figure 2(b). This band gap lies within the visible range, confirming the suitability of CZTS as an efficient visible-light-active material for photocatalytic and optoelectronic applications [8, 9].

The SEM image in Figure 3 shows a densely packed granular morphology, where the surface is composed of closely agglomerated grains. The grains appear irregular to quasi-spherical in shape, indicating polycrystalline growth of CZTS. Such grain agglomeration is due to solution-processed deposited CZTS films and suggests successful nucleation and growth of the material. The presence of grain boundaries throughout the film can facilitate charge separation by acting as trapping sites for photogenerated charge carriers, which is beneficial for photocatalytic reactions. The film surface appears compact with minimal large cracks or pinholes, indicating good surface coverage of the substrate. This uniform coverage is advantageous for photocatalytic applications, as it ensures continuous interaction between light, the catalyst surface, and reactant molecules.

The EDAX spectrum in Figure 4 confirms the presence of all constituent elements - Cu, Zn, Sn, and S with atomic percentages of 25.63%, 14.91%, 15.12%, and 44.34%, respectively. The detection of these elements without any extraneous peaks indicates the successful formation of CZTS with good compositional purity. The elemental ratios are close to the stoichiometric composition of CZTS, suggesting effective incorporation of metal cations and sulfur into the lattice during film deposition. The relatively higher sulfur content may be attributed to sulfur-rich growth conditions or surface enrichment, which is often beneficial in suppressing sulfur vacancies and reducing non-radiative recombination centers. The slight deviation in metal ratios is commonly observed in chemically synthesized

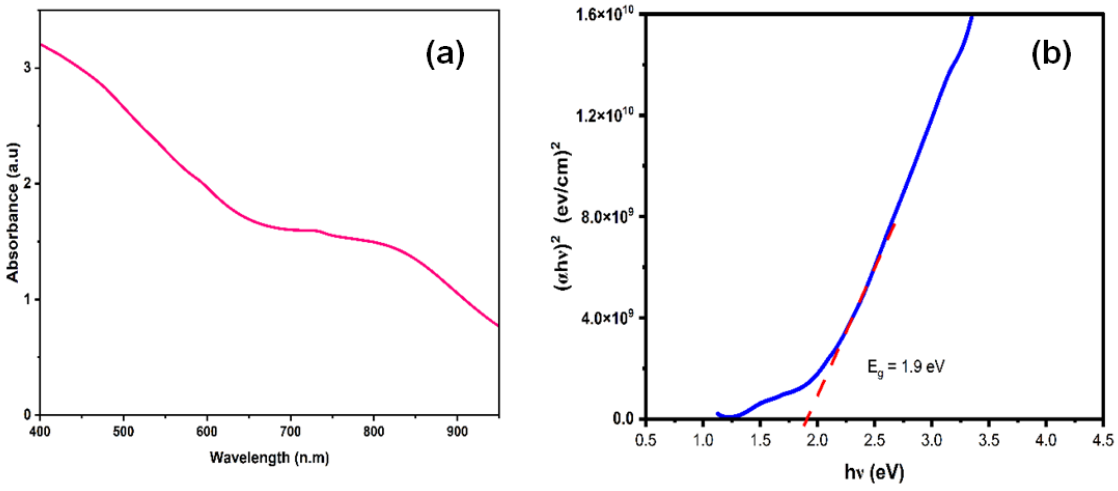

Figure 2. (a) Absorption spectrum and (b) Tauc plot of CZTS thin films.

© 2026 Authors. The authors retain copyright and full publishing rights under a CC BY 4.0 International License.

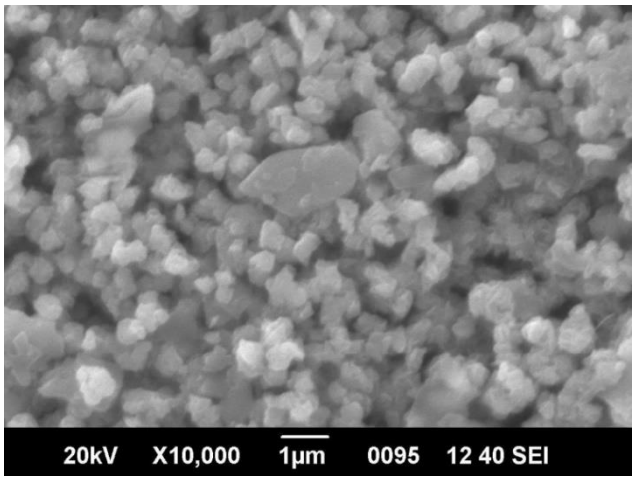

Figure 3. SEM image of CZTS thin film.

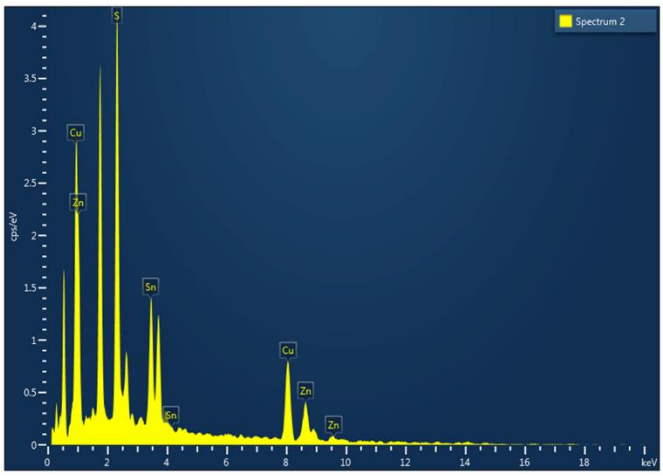

Figure 4. EDAX spectrum of CZTS.

CZTS thin films and can influence defect chemistry, particularly the formation of copper vacancies and antisite defects. Such compositional characteristics are known to favor p-type conductivity and can enhance photocatalytic performance by promoting efficient charge separation [10].

AFM analysis, as depicted in Figure 5, provides quantitative information about the surface morphology and roughness of the CZTS thin film. The root mean square roughness (R_q) of 33.7 nm represents the standard deviation of surface height variations, indicating a moderately rough surface with noticeable height fluctuations. The average roughness (R_a) value of 27.0 nm corresponds to the mean deviation of surface heights from the average plane, further confirming a non-uniform but reasonably homogeneous surface morphology.

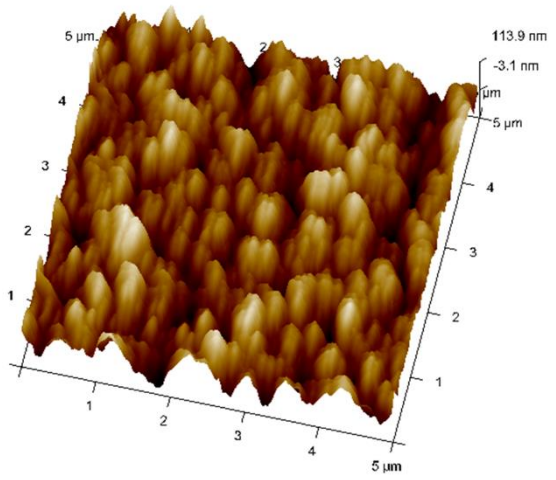

Figure 5. Surface roughness of thin film by AFM analysis.

A moderately rough surface with well-developed grains can enhance light trapping and surface activity. The presence of height variations and surface features promotes light scattering and multiple reflections at the film surface. This improves light harvesting by increasing the interaction time between incident photons and the photocatalyst, leading to enhanced generation of electron-hole pairs under visible light. Surface roughness also contributes to the formation of surface defects and grain boundaries, which can act as trapping sites for charge carriers. These traps help to suppress the rapid recombination of photogenerated electrons and holes, thereby increasing their lifetime and improving photocatalytic efficiency.

Figure 6(a) and (b) show characteristic peaks at a wavelength of 662 nm of the MB-dye solution and the effect of the addition of CZTS catalyst of 2 cm^2 and 4 cm^2 for different reaction times. The peak intensity was observed to decrease with time, with a faster reduction for the solution of 4 cm^2 catalyst compared to the 2 cm^2. No degradation was observed under dark condition showing that MB-dye is stable and cannot be degraded itself as depicted in Figure 7(a). After the addition of the CZTS catalyst to the MB-dye solution and irradiation, a reduction in the peak intensity was observed. The catalytic degradation efficiency (%) for CZTS thin film was calculated as [11]:

© 2026 Authors. The authors retain copyright and full publishing rights under a CC BY 4.0 International License.

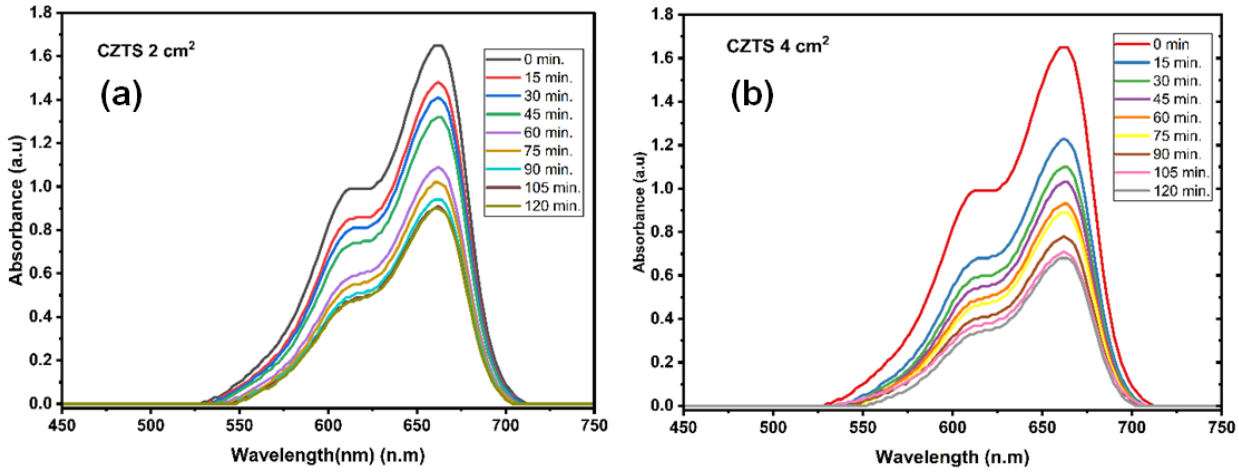

Figure 6. Absorption spectra of MB solution under visible light in the presence of (a) CZTS 2 cm², (b) CZTS 4 cm² for different time intervals.

$$Degradation\ Efficiency = 100\left(\frac{C_0 - C_t}{C_0}\right) = 100\left(\frac{A_0 - A_t}{A_0}\right) \quad (1)$$

where 'C_0' is the initial concentration after equilibrium adsorption, 'C_t' is the concentration after irradiation time 't', 'A_0' is the initial dye solution absorbance in the absence of catalysis, and 'A_t' is the dye solution absorbance in the presence of the catalyst after a time 't'. Plot of $[A_t]/[A_0]$ against reaction time was shown in Figure 7(b), which indicates that the self-degradation of MB-dye in the presence of light is negligible after 120 min.

The apparent rate constant(k_{app}) calculated by the pseudo-first-order reaction model- photodegradation kinetics (Eq. 2) to estimate the degradation rate of MB-solution from the slope of the linear plot of $\ln(C_0/C)$ versus irradiation time, as indicated in Figure 8 [3].

$$ln\left(\frac{C_0}{C_t}\right) = k_{app}t \quad (2)$$

The MB-solution with CZTS thin film catalyst of active area of 4 cm² exhibited a higher apparent rate constant (k_{app} = 0.00674 min^{-1}) compared to the 2 cm² thin film catalyst, which showed a slightly lower value (k_{app} = 0.00562 min^{-1}). The enhanced photocatalytic performance of the larger-area film can be attributed to its greater effective active surface area, improved light absorption, and increased availability of catalytic sites. This allows for more efficient generation of photogenerated electron-hole pairs and their

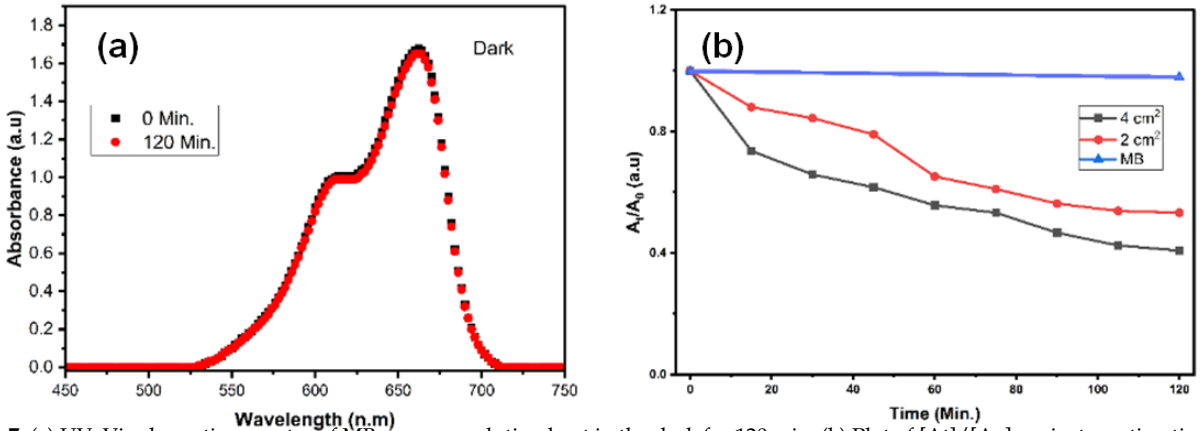

Figure 7. (a) UV–Vis absorption spectra of MB aqueous solution kept in the dark for 120 min. (b) Plot of [At]/[Ao] against reaction time t, for a catalyst of dimensions 4 and 2 cm².

© 2026 Authors. The authors retain copyright and full publishing rights under a CC BY 4.0 International License.

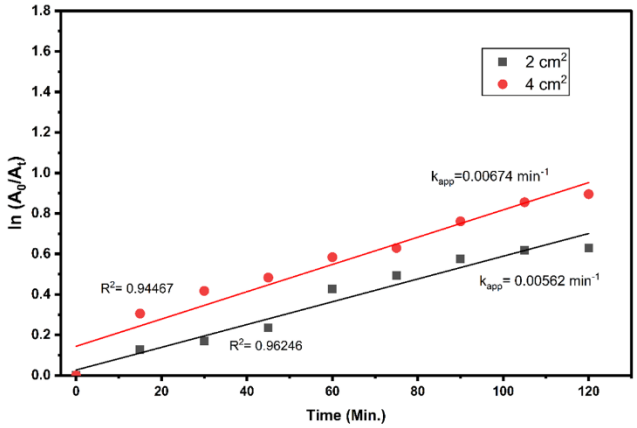

Figure 8. Rate of the reaction against irradiation time t.

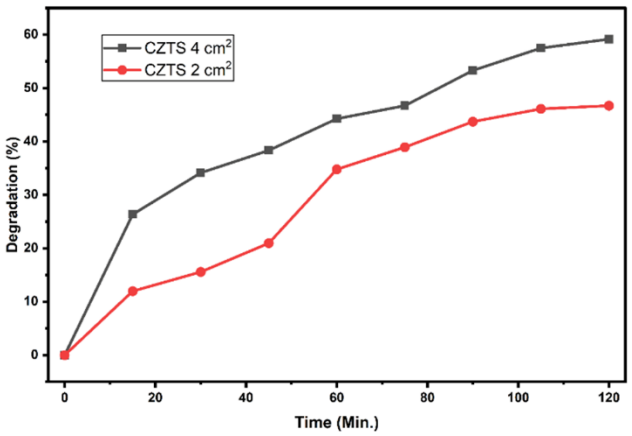

Figure 9. Degradation % of two catalysts of different dimensions against reaction time t.

participation in redox reactions responsible for MB degradation. Figure 9 shows the variation of degradation (%) with reaction time of the catalysts, and 46% degradation was observed for 2 cm² and 60 % degradation for 4 cm² thin films within 120 minutes. The degradation curve and rate constant indicate that the degradation strongly depends on the area of the CZTS catalyst-thin film and reaction time.

The MB-dye solution degradation mechanism in the presence of CZTS, which acts as a catalyst on exposure to the light, is explained and schematically shown in Figure 10(a). The possible reaction mechanism of dye degradation is shown below [11]. The degraded solutions after 120 min. of irradiation are shown in Figure 10(b), (c), and (d).

$$CZTS + hv \rightarrow CZTS\,(e_{CB}^{-} + h_{VB}^{+}) \quad (3)$$

$$H_2O + h_{VB}^{+} \rightarrow OH^{\bullet} + H^{+} \quad (4)$$

$$O_2 + e_{CB}^{-} \rightarrow O_2^{\bullet -} \quad (5)$$

$$O_2^{\bullet -} + H_2O \rightarrow H_2O_2 \quad (6)$$

$$H_2O_2 \rightarrow 2OH^{\bullet} \quad (7)$$

$$OH^{\bullet} + Dye \rightarrow Degraded\ Product \quad (8)$$

4. Conclusions

The structural analysis revealed the kesterite crystal structure. The SEM analysis confirms that the CZTS thin

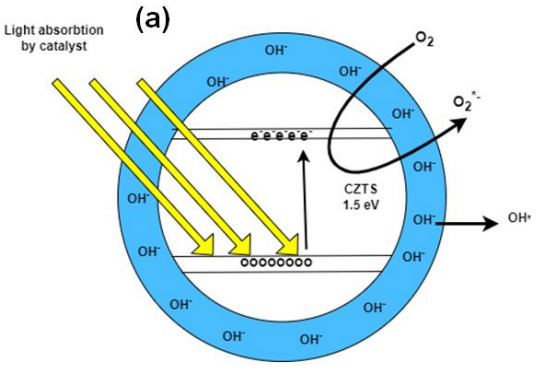

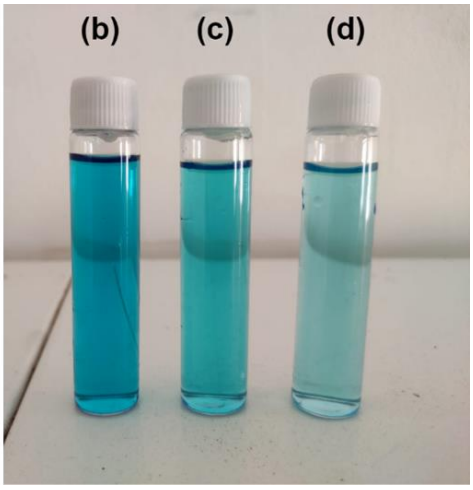

Figure 10. (a) Schematic representation of the degradation of MB-dye by CZTS catalyst on exposure to light. (b) Photographs of the MB dye solution after 120 min: without catalyst (c), degraded by CZTS catalyst 2 cm², and (d) degraded by CZTS catalyst 4 cm².

© 2026 Authors. The authors retain copyright and full publishing rights under a CC BY 4.0 International License.

film possesses a uniform, granular, and rough morphology, which is favorable for enhanced photocatalytic performance under visible light irradiation. The observed surface roughness and particle clustering enhance light scattering and increase the effective surface area, promoting improved light absorption and adsorption of pollutant molecules during photocatalysis. The EDAX results confirm the successful synthesis of CZTS with near-stoichiometric composition, making the thin film suitable for optoelectronic and photocatalytic applications. Increasing the catalyst surface area leads to improved degradation kinetics of MB-dye under visible light illumination. A densely packed granular morphology with sub-micrometer-sized grains and uniform surface coverage enhances light scattering and provides abundant active sites for photocatalytic reactions. The photocatalytic kinetic study showed apparent rate constants of 0.00562 min^{-1} and 0.00674 min^{-1} for 2 cm^2 and 4 cm^2 catalysts, respectively, and about 46% and 60% degradation were observed after 120 minutes of irradiation. The result indicates that the photocatalytic degradation of MB-aqueous solution depends on the area of the CZTS thin film and reaction time.

Acknowledgments

The authors thank the Department of Physics, Swami Anandatheertha Campus, Kannur University, for Raman analysis, STIC CUSAT for SEM-EDX, UV-VIS-NIR analysis, and thickness measurements, and Govt. College Madappally and Govt. College Nadapuram for photocatalytic study.

Conflict of Interest

The authors declare no conflict of interest.

References

1. C. Rakhi and K.C. Preetha. Synthesis and characterization of ZrO2/Bi2MoO6 heterostructured thin films for optoelectronic and photocatalytic applications. *Applied Physics A*, **2021**, *128*, 20.
2. X. Yu, et al. Cu2ZnSnS4-Pt and Cu2ZnSnS4-Au Heterostructured Nanoparticles for Photocatalytic Water Splitting and Pollutant Degradation. *Journal of the American Chemical Society*, **2014**, *136*, 9236.
3. T. Kieu Loan Phan, et al. Photocatalytic Activity Enhancement of ZnO/CZTS Thin Film Heterostructures in Visible Region: Controlling Phase Pure Kesterite CZTS Thin Films and the Effect of the Number of Seed Layers on Photocatalytic Performance. *Russian Journal of Electrochemistry*, **2024**, *60*, 644.
4. S.S. Shinde. Photocatalytic degradation of RhB and TNT and photocatalytic water splitting with CZTS microparticles. *Journal of Semiconductors*, **2015**, *36*, 073003.
5. K.G. Deepa, P.C. Ramamurthy, and M.K. Singha. Mesoporous Cu2ZnSnS4 nanoparticle film as a flexible and reusable visible light photocatalyst. *Optical Materials*, **2019**, *98*, 109492.
6. S. Dursun, et al. Investigation of photocatalytic activity (under visible light) of ultrathin CZTS films produced in different thicknesses by PLD method. *Optical and Quantum Electronics*, **2023**, *55*, 166.
7. C.T. Illiyas and K.C. Preetha. Synthesis and characterization of Vanadium (V)-doped CZTS thin films by chemical spray pyrolysis method for solar cell applications. *Journal of Materials Science: Materials in Electronics*, **2023**, *34*, 1380.
8. C.T. Illiyas and K.C. Preetha. An Investigation on Structural, Morphological, Optical, and Electrical Properties of Copper Zinc Tin Sulfide (CZTS) Thin Films Prepared by SILAR Method. *Brazilian Journal of Physics*, **2024**, *54*, 127.
9. S.P. Keerthana, et al. Synthesis of surfactant assisted Cu2ZnSnS4 (CZTS) photocatalysts for removal of dyes from wastewater. *Sustainable Energy Technologies and Assessments*, **2024**, *65*, 103778.
10. C.T. Illiyas and K.C. Preetha. Impact of europium (III) on optoelectronic properties of CZTS thin films prepared by spin coating method. *Journal of Materials Science: Materials in Electronics*, **2024**, *35*, 1893.
11. S.A. Phaltane, et al. Photocatalytic degradation of methylene blue by hydrothermally synthesized CZTS nanoparticles. *Journal of Materials Science: Materials in Electronics*, **2017**, *28*, 8186.

© 2026 Authors. The authors retain the copyright and full publishing rights. This article is licensed under a Creative Commons Attribution 4.0 BY International License.

© 2026 Authors. The authors retain copyright and full publishing rights under a CC BY 4.0 International License.

Toxic and Growth Effects of Ag-TiO_2 Nanoparticles on *Etroplus suratensis* Fingerlings with Statistical Application

Kumar Pandion [a], Aarrthy M. Arunachalam [b], Archana Sharma [c], Kantha Deivi Arunachalam [c,*]

[a] *Center for Environmental Nuclear Research, Directorate of Research, SRM Institute of Science and Technology, Kattankulathur, 603203, Chennai, TN, India*

[b] *Kaplan Teaching Centre, Washington D.C., 20036, USA*

[c] *Faculty of Sciences, Marwadi University, Rajkot, Gujarat, 360 003, India*

Editor's note: Improper disposal of nanoparticles poses significant risks to environmental health. The extremely small size of silver-titanium dioxide (Ag-TiO_2) nanoparticles results in a high surface area-to-weight ratio, which enhances their reactivity and allows toxic substances to adhere to their surfaces. Pandion et al. assessed the impact of dietary exposure to Ag-TiO_2 nanoparticles on the growth performance of *Etroplus suratensis* fingerlings. The findings demonstrate that Ag-TiO_2 nanoparticles exert concentration-dependent effects on these fish, with extended exposure to elevated concentrations adversely affecting growth and survival rates.

doi: 10.22034/jams.2026.260106

How to cite: K. Pandion et al., *Journal of Applied Material Science*, **2026**, 2, 260106.

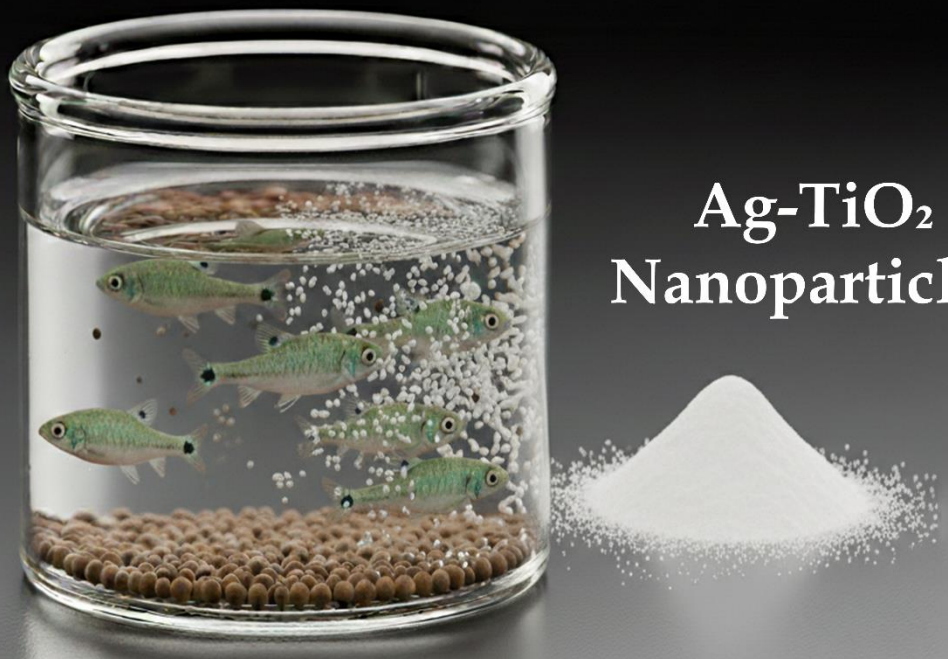

JOURNAL OF
APPLIED
MATERIAL
SCIENCE
jams.hsu.ac.ir

© 2026 *J. Appl. Mater. Sci.*This material is licensed under a Creative Commons Attribution 4.0 International License.

Journal of Applied Material Science **2026**, 2, 260106
How to cite: K. Pandion et al., *Journal of Applied Material Science*, **2026**, 2, 260106.
Journal homepage: **jams.hsu.ac.ir**

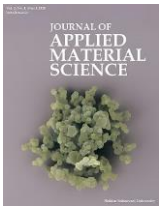

Original Research

Toxic and Growth Effects of Ag-TiO_2 Nanoparticles on *Etroplus suratensis* Fingerlings with Statistical Application

Kumar Pandion [a], Aarrthy M. Arunachalam [b], Archana Sharma [c], Kantha Deivi Arunachalam [c,*]

[a] *Center for Environmental Nuclear Research, Directorate of Research, SRM Institute of Science and Technology, Kattankulathur, 603203, Chennai, TN, India*

[b] *Kaplan Teaching Centre, Washington D.C., 20036, USA*

[c] *Faculty of Sciences, Marwadi University, Rajkot, Gujarat, 360 003, India*

Abstract

Silver-doped titanium dioxide nanoparticles (Ag-TiO_2 NPs) are widely used and increasingly released into aquatic environments, raising concerns about their ecological impacts. This study evaluated the effects of dietary Ag-TiO_2 nanoparticle exposure on the growth performance of *Etroplus suratensis* fingerlings. Fish were fed diets supplemented with Ag-TiO_2 nanoparticles at concentrations of 1, 10, 100, and 1000 mg kg^{-1} for 12 weeks under controlled water quality conditions. Acute toxicity (LC_{50}) tests revealed concentration-dependent mortality, with the highest mortality (24% within 96 h) observed at 1000 mg kg^{-1}. Growth performance, assessed through length and weight measurements, exhibited a clear concentration and time-dependent response. The 10 mg kg^{-1} treatment group showed the highest percentage weight gain (134.24%) and final biomass (34.01 g), indicating an optimal growth response. One-way ANOVA confirmed significant differences among treatments ($p < 0.05$). Pearson correlation analysis demonstrated a strong positive relationship between weight gain and biomass, while mortality was negatively correlated. Principal component analysis identified weight gain and biomass as major contributors to PC1, whereas mortality dominated PC2. Cluster analysis further highlighted the adverse effects of higher Ag-TiO_2 concentrations. Overall, the findings demonstrate that Ag-TiO_2 nanoparticles exert concentration-dependent effects on *Etroplus suratensis*, with prolonged exposure to higher concentrations impairing growth and survival, indicating potential ecological risks in nanoparticle-contaminated aquatic ecosystems.

Keywords: Ag-TiO_2 nanoparticles; Fish; Growth; Statistical application.

* Corresponding author.
Email address: kanthadevi.arunachalam@marwadieducation.edu.in (K.D. Arunachalam)

Received 23 December 2025
Revised 5 February 2026
Accepted 9 February 2026
Available online 13 February 2026

https://doi.org/10.22034/jams.2026.260106
© 2026 Authors. The authors retain copyright and full publishing rights under a CC BY 4.0 International License.

1. Introduction

Silver-doped titanium dioxide nanoparticles (Ag-TiO_2) are widely used engineered materials incorporated into manufacturing products such as dyes, textiles, cosmetics, individual care products, and even nutrition, owing to their great anti-corrosion capacity, chemical solidity, and strong photo-catalytic concentration [1]. Advances in nanotechnology have enhanced nanoparticle synthesis techniques, improved their physical and chemical properties, and led to their extensive use in diverse industries, including cosmetics, textiles, and electronics.

However, careless disposal of nanoparticles can result in environmental toxicity. Due to their extremely small size, Ag-TiO_2 has a greater surface area-to-weight relation, which increases their surface reactivity and allows toxic substances to adsorb onto their surface [2]. These nanoparticles can cross physiological barriers such as the blood-brain and blood-eye barriers, potentially causing xenobiotic effects [3, 4]. For example, silver nanoparticles have been shown to accumulate in the head, yolk, plasma, and fish embryos, leading to severe tissue destruction [5].

Once discharged into aquatic environments, Ag-TiO_2 nanoparticles undergo various physical, chemical, and biological transformations that alter their physicochemical properties and toxicity. Interactions such as deposition, aggregation, and stabilization (DLVO theory) determine their transport and persistence in natural and artificial waters [6]. In the incidence of natural organic material (NOM), Ag-TiO_2 nanoparticles tend to form aggregates ranging from nanometers to micrometers and can adsorb other ligands, increasing their toxicity [7]. Furthermore, interaction with biological macromolecules forms a bio-corona layer, conferring a "biological identity" that influences their environmental and toxicological behavior [8].

Toxicity tests, such as the 96-hour LC_{50}, measure the concentration of a substance that is lethal to 50% of a test population within 96 hours [9]. Acute toxicity refers to the short-term entry of toxicants into organisms, causing physiological disruption or organ damage. Standard criteria for acute toxicity in fish include mortality, immobility, loss of equilibrium, and impaired growth. Accumulation of nanoparticles in low-flow aquatic systems can increase their local concentration, intensifying toxic effects. Small fish species can play a critical role in trophic dynamics because of their mid-level position in food webs [10].

Most existing studies have examined waterborne exposure of Ag-TiO_2, whereas dietary exposure data, especially regarding effects on fish growth indices, are scarce. *Etroplus suratensis* (E. *suratensis*), a commercially important brackish water species in South Asia, was chosen for the present study due to its fast growth, excessive yield, and market demand. Previous research has reported toxic impacts of Ag-TiO_2 on fish, such as gill pathology and reduced Na^+/K^+ ATP concentration in rainbow trout [11] and concentration- and time-dependent growth inhibition in fish [12].

Numerous investigations have documented Ag-TiO_2 toxicity in aquatic systems and humans [13-15]. Reported harmful impacts include gastrointestinal, pulmonary, and dermal toxicity in mammals [16] and genotypic changes such as ribosomal function alterations in aquatic organisms [17]. However, most studies have been short-term, and few have tested unmodified Ag-TiO_2 in aquatic species under long-term exposure [18-21].

This study investigates the effects of dietary Ag-TiO_2 exposure over 12 weeks on the growth performance of E. *suratensis* fingerlings under controlled brackish water conditions. In addition to growth indices, physicochemical water parameters and LC_{50} concentrations were monitored to better understand long-term nanoparticle toxicity in aquaculture-relevant conditions.

2. Experimental

2.1. Animal and acclimatization

Etroplus suratensis fingerlings, with a standard initial mass of 10 ± 2.5 g and length of 4 ± 2.8 cm, were procured from the fish seed hatchery at CIBA, Chennai. Healthy, uniformly sized individuals were chosen and given a potassium permanganate ($KMnO_4$) bath to eliminate any organisms. Earlier to experimental revelation, animals were adjusted for two weeks in 100 L concrete units under a 12 h brightness:12 h darkness cycle and fed a basal diet two times daily.

2.2. Nutrition formulation

The nutrition (30% crude protein; Table 1) and nanomaterials of silver titanium dioxide (anatase form,

© 2026 Authors. The authors retain copyright and full publishing rights under a CC BY 4.0 International License.

< 25 nm) were procured from local vendors (Sigma company, USA). Trial diets were prepared by incorporating each nanoparticle type at concentrations of 1, 10, 100, and 1000 mg kg^{-1} into the feed, following the trial protocol. Blackstrap molasses (7%) was treated as a binder to combine the powdered ingredients into a semisolid paste, which was then processed through a grinding machine to produce feed of approximately 4 mm width. The feed was sliced into constant pellets, dried out, and stored in sealed jars until consumed [22].

Table 1. Diet formulation

Crude Protein	min. 30%
Crude Fat	min. 5.8%
Crude Fiber	max. 6.7%
Moisture	max. 10%
Ash	max. 8.5%

2.3. Experimental design

Adjusted animals were independently weighed and determined before being randomly allocated into fifteen chambers (59 × 34 × 40 cm) at a density of 50 fish per tank, with three replicate tanks per treatment. Therapies were defined by the absorption of silver-doped titanium dioxide nanoparticles incorporated into the feedstuff: T0 (control), T1 (1 mg kg^{-1}), T2 (10 mg kg^{-1}), T3 (100 mg kg^{-1}), and T4 (1000 mg kg^{-1}). The animals were kept alive in a flow-through system (current rate: 5.1–6.0 L h^{-1}) under controlled water quality conditions: hotness 29.4–30.1 °C, acid or alkali in a substance 7.4–7.6, and amount of oxygen in water 11.1–11.5 mg L^{-1}, monitored with a HANNA multipara meter probe (HI 9829). Animals were fed the respective test diets twice a day (08:00 and 20:00 h) for 30 min to ensure complete consumption. Control fish received the basal diet to satiation following the same schedule. Not consumed feed and fecal matter were drained off after feeding. The trial lasted for 12 weeks, during which mortality was recorded daily, and dead fish were removed promptly [23].

2.4. Physicochemical parameters of the water

Water samples were gathered in bottles and saved in a refrigerator (4 °C) until transported to the test site. Temperature, pH, saltiness, dissolved oxygen, and thick with suspended matter were determined on-site using an involving more than one parameter probe. The tests were then carried to the test site and saved in a refrigerator at 4 °C until further analysis. Prior to chemical analysis, tests were removed through Whatman No. 42 clean paper and acidulated with concentrated nitric acid (3 mL L^{-1}) and chloroform (0.5 mL L^{-1}) to prevent microbial growth. They were subsequently passed through a 0.45 µm Millipore removed nutrients, including essential elements, were determined using the usual analytical procedures. A pigment absorption was assessed following pigment removal with 90% acetone, and absorbance was recorded utilizing a UV-visible light (Shimadzu UV series).

2.5. Acute-lethal toxicity test (LC_{50})

Adjusted animals were independently weighed and determined, then randomly assigned to fifteen tanks (59 × 34 × 40 cm) at a mass of 50 fish per chamber, with three duplicate tanks per treatment. Treatments corresponded to silver-doped titanium dioxide nanoparticle concentrations incorporated into the feedstuff: T0 (control), T1 (1 mg kg^{-1}), T2 (10 mg kg^{-1}), T3 (100 mg kg^{-1}), and T4 (1000 mg kg^{-1}). A static toxicity exposure system was used, with the test solution remaining unchanged throughout the 96-h trial. Water condition factors were determined before and after the experiment. Mortality and abnormal behavioral responses of E. *suratensis* were monitored continuously. Fish were considered dead when showing complete immobility and no abdominal flexion upon forced extension.

2.6. Fish growth

Five animals from every tank (50 per tank) were tested at the start of the experiment (day 0) and subsequently at fortnightly intervals. Fish were euthanized by immersion in a water solution of 3-aminobenzoic acid ethyl ester (MS-222; Sigma-Aldrich Chemical, St. Louis, MO, USA) at a concentration of 1.0 g L^{-1}, until opercular activity ceased. The juvenile fish were rinsed in water, blotted dry with towels, weighed, and measured for length. Growing performance factors were determined as follows: Exact growing rate (SGR, % day^{-1}) = [(ln Final weight - ln Initial weight)/Experimental period days] × 100.

2.7. Statistical analysis

Every analytical information was processed utilizing Python software. Statistical studies involved a one-way

© 2026 Authors. The authors retain copyright and full publishing rights under a CC BY 4.0 International License.

study of modification (ANOVA), Pearson association, principal module study (PCA), and a classified cluster study (HCA) to assess the relationships between nanoparticle exposure and growth performance parameters (weight gain and biomass) of *Etroplus suratensis*. Consequence was determined at $p < 0.05$.

3. Results and discussion

3.1. Physicochemical properties of water

Silver-doped titanium dioxide nanoparticles can enter fish either directly via the water route or indirectly through trophic transfer. Under both exposure routes, Ag-TiO_2 nanoparticles have been shown to accumulate in fish tissues [24], though maximum investigates have used waterborne exposure, particularly in zebrafish [25, 26]. Water temperature, a key factor influencing biological and chemical processes [27], ranged from 28.0 ± 1.0 °C during the study (Table 2). Surface temperatures were slightly higher than deeper waters due to sunlight, photoperiod length, and wind mixing [28]. The pH remained alkaline, ranging from 7.5 ± 0.5, consistent with seawater's high buffering capacity [29].

Salinity ranged from 20 ± 7.0 PSU, like other Indian coastal waters [30]. Dissolved oxygen (DO) levels were 5.5 ± 1.0 mg L^{-1}, reflecting the combined influence of photosynthesis, organic matter decomposition, and atmospheric exchange [31]. Turbidity averaged 2.5 ± 0.5 NTU, primarily influenced by sediment suspension, runoff, and phytoplankton biomass [32]. Silicate, an essential nutrient for marine primary producers, ranged from 11.0 ± 1.5 µmol L^{-1}, influenced by riverine input, sediment adsorption, and biogeochemical interactions [33]. Ammonia concentrations ranged from 9.0 ± 2.5 µmol L^{-1}, arising from organic matter decay, nitrification, and excretion [34]. Phosphate ranged from 30 ± 1.5 µmol L^{-1}, driven by river inflow, biological uptake, and benthic-pelagic coupling [35]. Nitrate concentrations were 4.0 ± 1.0 µmol L^{-1} [36].

Total nitrogen (TN) was 40 ± 2.0 µmol L^{-1}, with high levels potentially promoting eutrophication and harmful algal blooms [37]. Total phosphorus (TP) was 1.5 ± 0.5 µmol L^{-1}, mostly in particulate form [38]. Chlorophyll-a was an indicator of autotrophic biomass. Although Ag-TiO_2 tended to settle at the tank's lowest due to variability in water, a portion remained suspended in the water route throughout the experiment [39].

Table 2. Physicochemical properties of water

Sample No.	Parameters	Values
1	Temperature	28±1.0 °C
2	pH	7.5±0.5 pH
3	Salinity	20±7.0 PSU
4	Dissolved oxygen	5.5±1.0 mg L^{-1}
5	Turbidity	2.5±0.5 NTU
6	Nitrate	4.0±1.0 µmol L^{-1}
7	Ammonia	9.0±2.5 µmol L^{-1}
8	Silicate	11.0±1.5 µmol L^{-1}
9	Phosphate	30±1.5 µmol L^{-1}
10	TN	40±2.0 µmol L^{-1}
11	TP	1.5±0.5 µmol L^{-1}
12	Chlorophyll a	1.5±0.5 mg m^{-3}

3.2. Exposure and mortality of Etroplus suratensis juveniles to TiO_2 nanoparticles

This research represents the first information on the impacts of Ag-doped TiO_2 nanoparticles (Ag-TiO_2) on water animals. The 96-h LC_{50} of Ag-TiO_2 was determined to be 112 mg L^{-1}, whereas bulk Ag-TiO_2 showed no toxicity up to 300 mg L^{-1}. These results align with earlier studies: Xiong et al. [40] reported no mortality in fish at concentrations up to 50 mg L^{-1} for the majority of Ag-TiO_2 and 300 mg L^{-1} for Ag-TiO_2 with a recorded LC_{50} of 124.5 mg L^{-1} for Ag-TiO_2. Similarly, Diniz et al. [41] assessed the 96-h LC_{50} for Ag-TiO_2 in fish at 100 mg L^{-1}.

In the present experiment, *E. suratensis* juveniles were exposed to Ag-TiO_2 via dietary administration in five treatment groups: T0 (control), T1, T2, T3, and T4, over 96 hours. Exposure induced noticeable changes in opercular rate and visible physical damage, particularly on the gill surfaces. Mortality patterns varied across treatments (Table 3). The highest concentrations of T3 (100 mg kg^{-1}) and T4 (1000 mg kg^{-1}) showed early signs of toxicity within the first 8 h, leading to the most rapid onset of mortality. In contrast, the T2 group (10 mg kg^{-1}) exhibited first signs of mortality only after ~50 h of exposure.

These results indicate a clear concentration-dependent toxicity, with higher Ag-TiO_2 levels causing faster and more severe effects. Comparable findings have been reported for fish where 40%, 50%, and 80% mortality occurred at 150, 175, and 200 mg L^{-1}, respectively, within 96 h, and 100% mortality occurred at 225 mg L^{-1}, particularly in 24 h [42]. Similarly, Chen et

© 2026 Authors. The authors retain copyright and full publishing rights under a CC BY 4.0 International License.

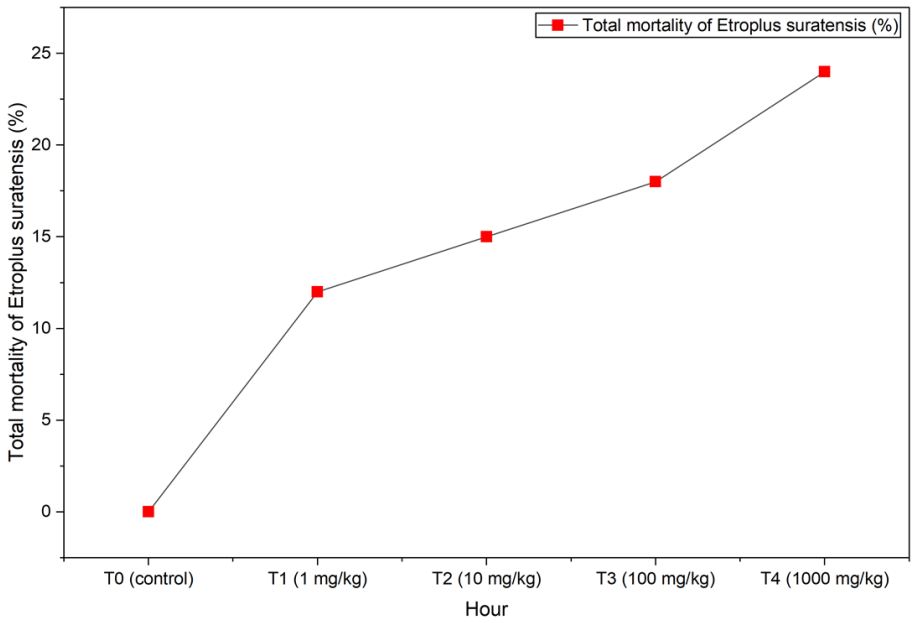

Figure 1. Exposure and Mortality of *Etroplus suratensis* Juveniles to TiO_2 Nanoparticles.

al. [43] observed elevated mortality in animals exposed to 1–7 mg L^{-1} Ag-TiO_2, with the highest mortality (16.7%) at 7 mg L^{-1}. In the current study, significant mortality occurred primarily within the first 8 h, suggesting acute toxicity effects were most pronounced early on. Thereafter, mortality rates stabilized, possibly due to reduced nanoparticle bioavailability or physiological adaptation by the fish. As shown in Figure 1, the T4 group recorded the highest mortality rate (24%), whereas T2 had the lowest (5%).

3.3. Growth performance of Etroplus suratensis juveniles exposed to Ag-TiO_2 nanoparticles

Etroplus suratensis is a commercially valuable species widely cultured in China's coastal region due to its tasty white meat, rapid growth, disease resistance, and great

Table 3. Exposure and Mortality of *Etroplus suratensis* Juveniles to Ag-TiO_2 Nanoparticles

Hour	T0 (control)	T1 (1 mg kg^{-1})	T2 (10 mg kg^{-1})	T3 (100 mg kg^{-1})	T4 (1000 mg kg^{-1})
1	0	0	0	0	0
2	0	0	0	0	0
4	0	0	0	0	0
8	0	0	0	0	3
12	0	0	0	2	4
16	0	0	0	1	2
24	0	0	0	3	1
36	0	1	0	4	1
48	0	1	0	2	4
50	0	0	3	0	3
62	0	4	1	0	2
72	0	3	1	3	3
96	0	3	0	2	2
Total mortality of *Etroplus suratensis* (%)	0	12	05	18	24

© 2026 Authors. The authors retain copyright and full publishing rights under a CC BY 4.0 International License.

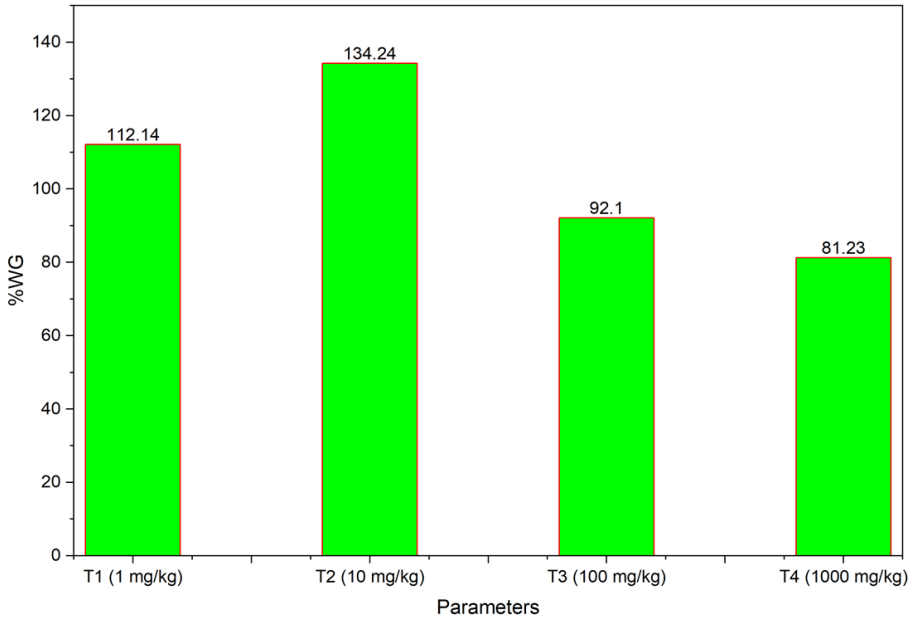

Figure 2. The highest percentage weight gain (%WG).

commercial value [44-46]. Sheethal et al. [47] reported acute toxicological effects of TiO_2 exposure in pearl spot, with muscular tissue being particularly sensitive even at very low concentrations. Similar neurotoxic effects of metals in aquatic animals have been recognized in previous reports [48-52]. In the present research, no mortality was noted in the control group (T0; basal diet), while minimal mortality occurred in T1 (1 mg kg^{-1}) and T2 (10 mg kg^{-1}). In contrast, higher concentrations, T3 (100 mg kg^{-1}) and T4 (1000 mg kg^{-1}), produced significant mortality after 12 weeks of dietary exposure (Figure 1).

The enhanced growth observed at low dietary Ag-TiO_2 concentrations, particularly in the T2 group, reflects a dose-dependent adaptive response that supports physiological homeostasis. At optimal levels, Ag-TiO_2 nanoparticles may improve metabolic efficiency and nutrient utilization, thereby promoting somatic growth without inducing stress. Similar low-dose growth stimulation has been reported in fish exposed to TiO_2 nanoparticles [11, 12]. In contrast, higher concentrations likely exceed the tolerance threshold, leading to oxidative stress and metabolic disruption. Consequently, growth inhibition at elevated doses is consistent with earlier findings in fish [53].

Growth performance differed significantly among treatments. Collections T1 and T2 confirmed the highest percentage weight gain (%WG) at 112.14% and 134.24%, respectively (Figure 2), outperforming even the control group. During the first four weeks, all groups gained weight at a similar rate (up to ~1 g). From week 6 onwards, growth declined sharply in T3 and T4. This trend aligns with Chen et al. 2011, who documented growth and involving impairments in fish under prolonged exposure to high Ag-TiO_2 nanoparticle concentrations. The highest weight gain (WG) and individual growing rate (SGR) were maintained by T1 and T2 throughout the 12-week trial (Figures 2 and 3), while T3 and T4 showed marked reductions by the experiment's end. This suggests a bi-modal effect of Ag-TiO_2 nanoparticles, low concentrations stimulated growth, whereas high concentrations were detrimental (Table 4). Similar growth-enhancing effects at optimal supplementation levels have been noted in other species, such as hybrid grouper fed with inositol [54].

One-way ANOVA (Tables 5 and 6; Figures 4 and 5) explained major differences ($p < 0.05$) in %WG, final biomass, and mortality among treatments, supported by high F-values. Both %WG and final biomass peaked in T1 and T2, whereas T4, and to a lesser extent T0 and T3, had lower values. Mortality followed a dose–response pattern: lowest in T0 and highest in T4. Pearson correlation analysis (Figure 5; Table 6) further revealed:

© 2026 Authors. The authors retain copyright and full publishing rights under a CC BY 4.0 International License.

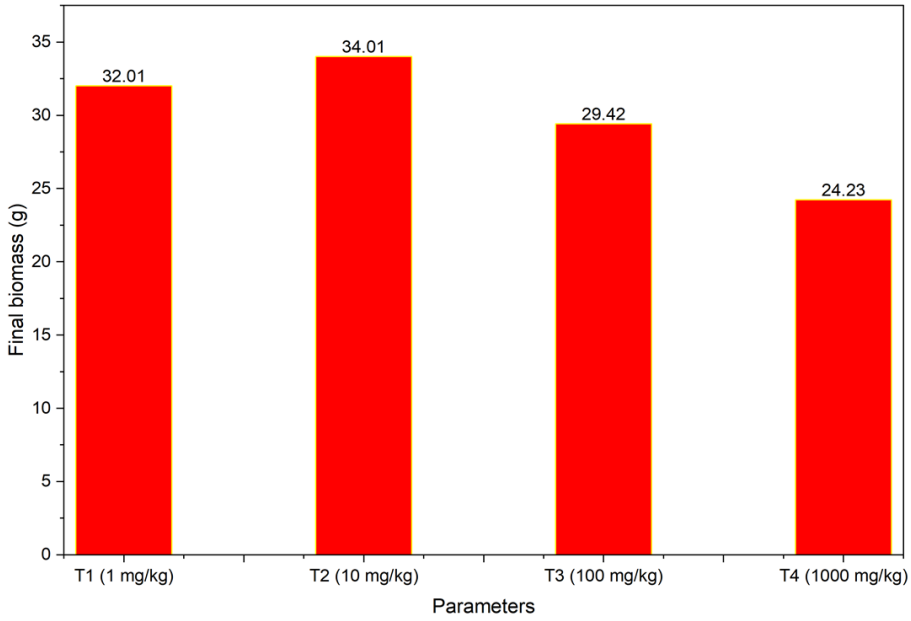

Figure 3. The highest percentage of biomass.

%WG vs. Final Biomass: Strong positive correlation (r = 0.90), increases in %WG were mirrored by biomass gains from T0 to T2, both declining in T3 and T4. %WG vs. Mortality: Moderate negative correlation (r ≈ –0.70), higher mortality corresponded to reduced %WG. Final Biomass vs. Mortality: Moderate-to-strong negative biomass correlation (r ≈ –0.70) decreased as mortality increased. These findings confirm that intermediate Ag-TiO_2 nanoparticle doses (T1, T2) optimize growth and biomass accumulation while minimizing mortality, whereas high doses (T4) severely impair growth and survival. The lowest losses recorded in the T2 treatment (10 mg kg^{-1}) likely reflect a hormetic response, in which exposure to an optimal nanoparticle concentration

Table 4. The bi-modal effect of Ag-TiO_2 nanoparticles at low concentrations stimulated growth

Parameters	Treatment	Initial weight and weight gains in the nth week						
		1st	2nd	4th	6th	8th	10th	12th
WG (g)	T0 (control)	10 ± 2.4	10.5 ± 2.0	11.1 ± 1.4	11 ± 1.5	11.2 ± 1.8	12 .1± 0.4	12 ± 0.5
	T1 (1 mg kg^{-1})	10 ± 2.5	10 .3± 2.2	11.3 ± 1.2	11.3 ± 1.2	11.3 ± 1.7	12 .3± 0.2	12.1 ± 0.4
	T2 (10 mg kg^{-1})	10 ± 2.4	10 .4 ± 2.1	11 ± 1.5	11 ± 1.5	11.2 ± 1.9	12 .2± 0.3	12 ± 1.5
	T3 (100 mg kg^{-1})	10 ± 2.5	10.3 ± 2.3	11.1 ± 1.4	11.5 ± 1.0	11.1 ± 1.9	12 .3± 0.2	12.3 ± 0.2
	T4 (1000 mg kg^{-1})	10 ± 2.5	10.4 ± 2.1	11 ± 1.5	11.7 ± 1.8	11.8 ± 1.2	12 .4± 0.1	12 ± 0.5
SGR (g)	T0 (control)	0.0 ± 0.05	0.54 ± 0.05	1.1 ± 0.05	1.0 ± 0.05	1.2 ± 0.05	2.1 ± 0.05	2.0 ± 0.05
	T1 (1 mg kg^{-1})	0.0 ± 0.05	0.30 ± 0.05	1.0 ± 0.05	1.3 ± 0.05	1.3 ± 0.05	2.3 ± 0.05	2.1 ± 0.05
	T2 (10 mg kg^{-1})	0.0 ± 0.05	0.4 ± 0.05	1.0 ± 0.05	1.0 ± 0.05	1.2 ± 0.05	2.2 ± 0.05	2.0 ± 0.05
	T3 (100 mg kg^{-1})	0.0 ± 0.05	0.3 ± 0.05	0.9 ± 0.05	1.0 ± 0.05	1.1 ± 0.05	2.3 ± 0.05	2.3 ± 0.05
	T4 (1000 mg kg^{-1})	0.0 ± 0.05	0.4 ± 0.05	1.0 ± 0.05	1.2 ± 0.05	1.8 ± 0.05	2.4 ± 0.05	2.5 ± 0.05
length (cm)	T0 (control)	4 ± 2.6	4.4 ± 0.4	5.4 ± 0.2	5.4 ± 0.5	5.8 ± 0.3	6.4 ± 0.2	6.5 ± 0.3
	T1 (1 mg kg^{-1})	4 ± 2.8	4.3 ± 0.5	5.4 ± 0.4	5.6 ± 0.2	5.8 ± 0.3	6.3 ± 0.4	6.6 ± 0.2
	T2 (10 mg kg^{-1})	4 ± 2.8	4.2 ± 0.6	5.3 ± 0.5	5.2 ± 0.6	5.8 ± 0.3	6.4 ± 0.2	6.7 ± 0.2
	T3 (100 mg kg^{-1})	4 ± 2.7	4.1 ± 0.7	5.2 ± 0.6	5.6 ± 0.2	5.8 ± 0.3	6.3 ± 0.2	6.4 ± 0.4
	T4 (1000 mg kg^{-1})	4 ± 2.8	4.0 ± 0.7	5.1 ± 0.4	5.4 ± 0.4	5.8 ± 0.3	6.0 ± 0.5	6.4 ± 0.4

© 2026 Authors. The authors retain copyright and full publishing rights under a CC BY 4.0 International License.

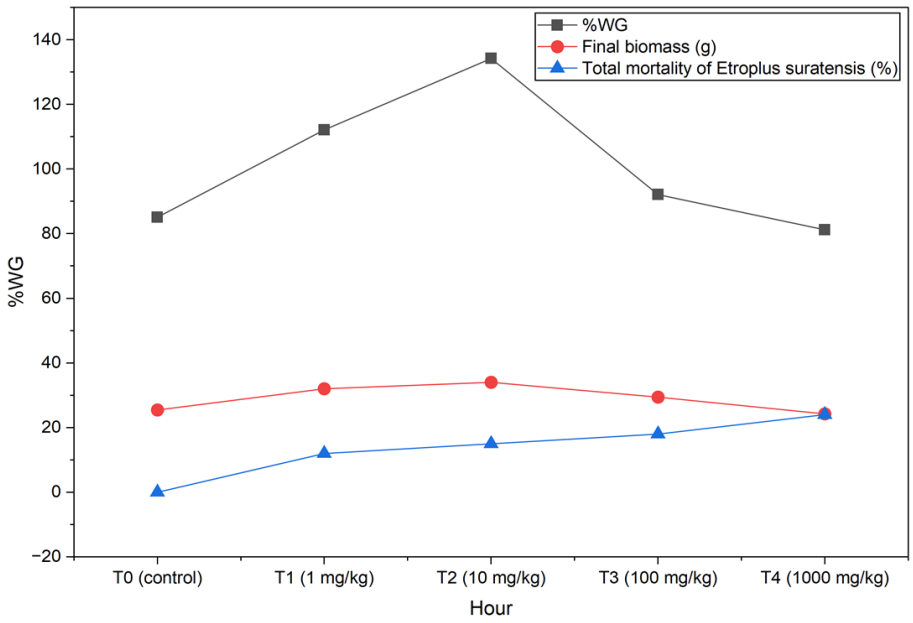

Figure 4. Boxplots illustrating patterns.

promotes physiological homeostasis and efficient metabolic functioning. At this intermediate dose, titanium oxide nanoparticles may enhance nutrient utilization, antioxidant capacity, and stress adaptation without inducing cellular damage. In contrast, the lower concentration (T1) may be insufficient to elicit such beneficial adaptive responses, while higher concentrations (T3 and T4) likely exceed the tolerance threshold of *Etroplus suratensis*, leading to oxidative stress, cellular disruption, and impaired physiological functions, thereby increasing mortality. This growth suppression at high concentrations may be linked to Ag-TiO_2 -induced redox inequality and improved reactive oxygen species (ROS) production, disrupting antioxidant defenses [53, 55].

3.4. ANOVA analysis

ANOVA was performed to compare weight gain percentage (%WG), final biomass, and mortality among treatments (T0–T4). Every variable indicated statistically significant differences ($p < 0.05$), with high F-values confirming strong treatment effects. Weight gains were highest in intermediate doses (T1 and T2), while the highest dose (T4) and, to a lesser extent, T0 and T3, resulted in reduced gains. Final biomass followed a similar pattern, peaking at T1 and T2 and decreasing at T0 and T4. Mortality exhibited a clear dose–response trend, being lowest in T0 and highest in T4.

Boxplots (Figure 4) illustrate these patterns: %WG: Higher medians in T1 and T2; lowest in T4. Final biomass: Peak at T2, declines in T3 and T4. Mortality: Near-zero in T0, moderate in T1–T3, maximum in T4. These results indicate that intermediate nanoparticle doses promote optimal growth and low mortality, whereas the highest dose (T4) markedly impairs growth and increases mortality (Table 5).

3.5. Qualitative and quantitative Pearson Correlation study

A Pearson correlation study was used to assess relationships among %WG, final biomass, and mortality (Figure 5; Table 6). %WG vs Final Biomass: Both variables increased from T0 (85 %, 25 g) to T2 (134 %, 34

Table 5. ANOVA study

Variable	F-value	p-value	Interpretation
%WG	124.27	7.95×10^{-14}	Significant differences between treatments
Final Biomass	23.70	2.39×10^{-7}	Significant differences between treatments
Mortality	41.53	2.04×10^{-9}	Significant differences between treatments

© 2026 Authors. The authors retain copyright and full publishing rights under a CC BY 4.0 International License.

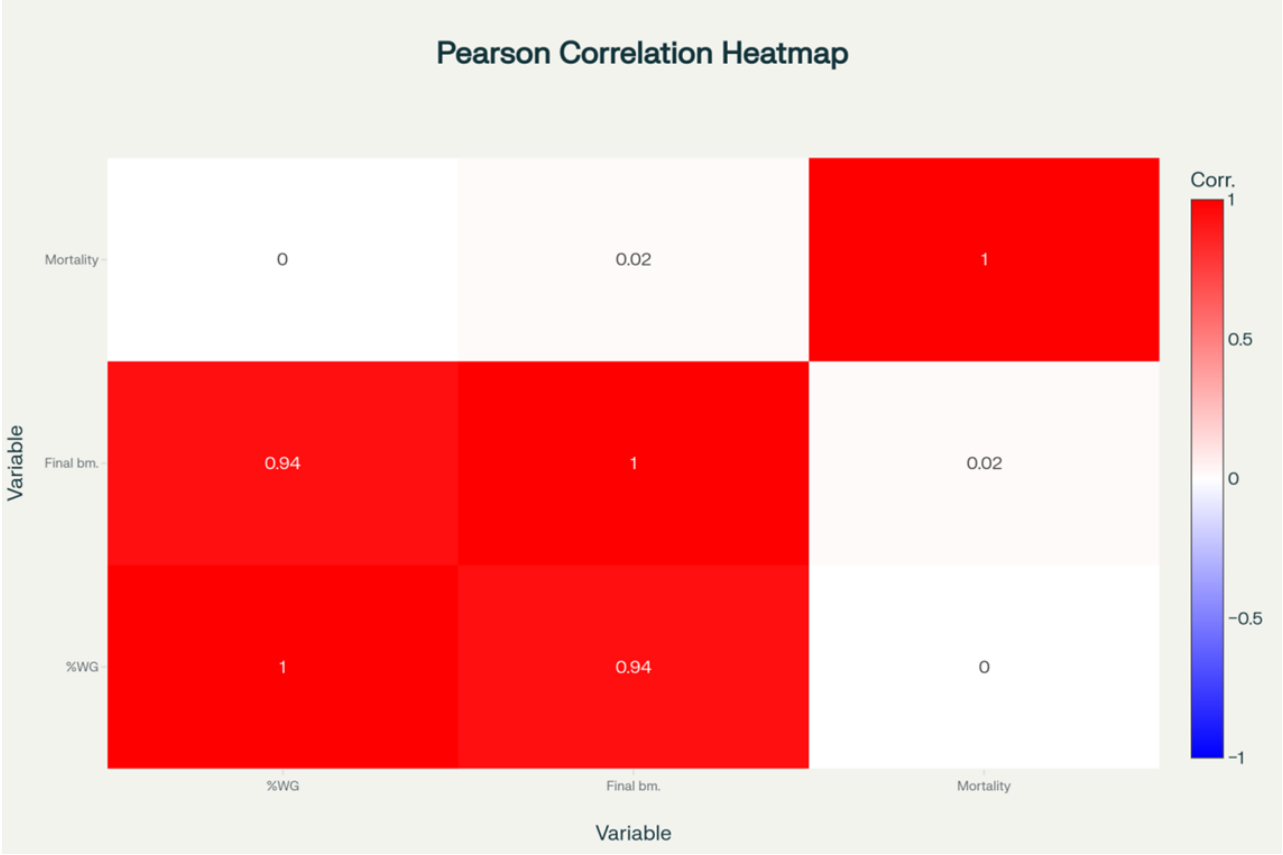

Figure 5. Qualitative and quantitative Pearson correlation analyses.

g), then declined in T3 and T4. A strong positive correlation (r = 0.90) confirms that higher weight gain translates directly into greater final biomass. %WG vs Mortality: As mortality rose from 0 % (T0) to 24 % (T4), %WG generally declined (85 % to 81 %), yielding a moderate negative correlation (r ≈ –0.70).

Final Biomass vs Mortality: Similarly, biomass decreased as mortality increased, with a moderate-to-strong negative correlation (r ≈ –0.70). In summary, %WG and final biomass are strongly and positively correlated, whereas both are negatively correlated with mortality. These findings indicate that optimal growth and biomass occur under low mortality conditions, typically at intermediate nanoparticle exposure levels.

3.6. Principal Component Analysis

Principal Module Analysis (PCA) was applied to %WG, final biomass, and mortality to reduce dimensionality and explore multivariate relationships among treatments (T0–T4). The unique two principal sections described 53.65% and 44.41% of the modification; correspondingly, the method of accounting accounted for almost 100 % of the entire variation (Figure 6). The PCA biplot showed clear treatment separation. T1 and T2 clustered together, reflecting similar performance marked by high %WG and biomass with low mortality. T4 was positioned furthest from these groups, driven by high mortality and poor growth. T0 and T3 occupied intermediate positions. Variable loadings indicated that %WG and final biomass loaded strongly and positively on PC1, whereas

Table 6. Pearson correlation analysis

Pair	Expected Pearson r	Relationship
%WG vs Final biomass	+0.95	Strong positive
%WG vs Mortality	-0.7	Moderate negative
Biomass vs Mortality	-0.7	Moderate negative

© 2026 Authors. The authors retain copyright and full publishing rights under a CC BY 4.0 International License.

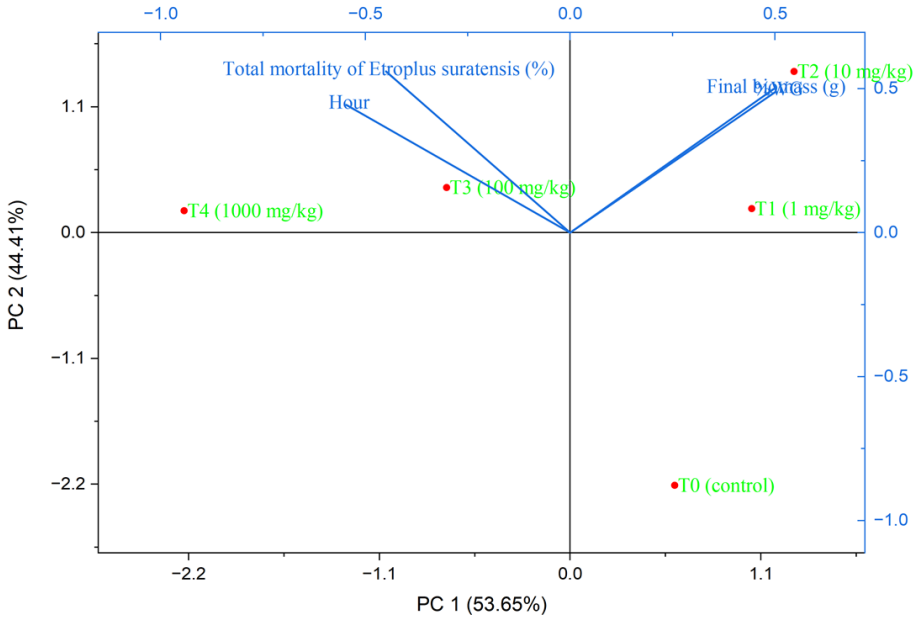

Figure 6. The principal component analysis (PCA) study.

mortality loaded in the opposite direction, mainly along PC2. This multivariate view highlights distinct grouping patterns and trade-offs between growth and survival, providing insights beyond those from individual pairwise correlations.

3.7. Hierarchical Clustering Dendrogram analysis

Hierarchical clustering using Euclidean distance was applied to %WG, final biomass, and mortality to group treatments (T0–T4) (Figure 7). T1 and T2 clustered at the smallest Euclidean distance, reflecting their close

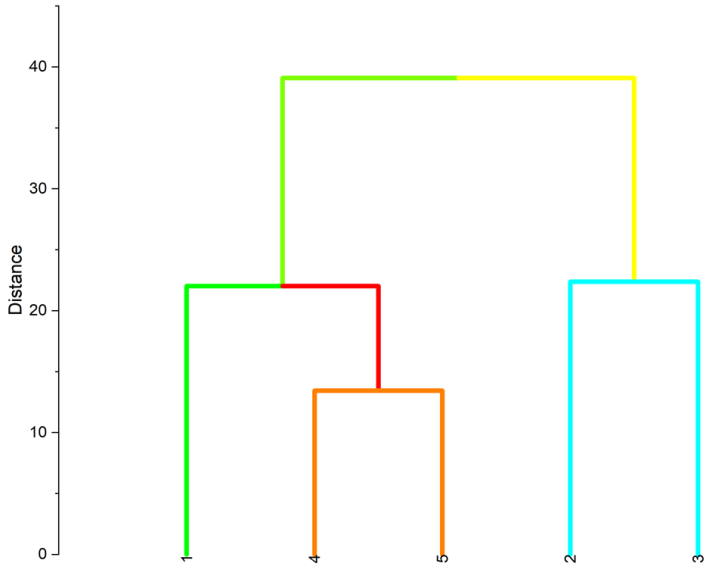

Figure 7. The hierarchical clustering studies. 1.T0 (control), 2. T1 (1 mg/kg), 3.T2 (10 mg/kg), 4. T3 (100 mg/kg), and 5. T4 (1000 mg/kg).

© 2026 Authors. The authors retain copyright and full publishing rights under a CC BY 4.0 International License.

similarity in performance, characterized by high %WG, high biomass, and low mortality. T3 and T4 formed a separate subcluster, both showing reduced growth and elevated mortality, with T4 emerging as an outlier due to its extreme mortality and minimal growth. The control (T0) joined the T1–T2 cluster at a higher merge height, indicating moderate similarity to these high-performing treatments and marked dissimilarity from T3 and T4.

The largest vertical separation occurred when the T1–T2–T0 cluster merged with the T3–T4 cluster, indicating two primary performance groups: High growth / low-to-moderate mortality: T1, T2, T0 and Low growth / high mortality: T3, T4 Optimal outcomes for *Etroplus suratensis* occurred at low (T1, T2) or zero (T0) Ag-TiO_2 nanoparticle doses. In contrast, high-dose treatments (T3, T4) were linked to poor growth and increased mortality, with T4 (1000 mg/kg) showing the most severe negative effects. The dendrogram thus clearly separates effective from harmful concentrations, underscoring a dose-dependent trade-off between growth and survival.

4. Conclusions

The present study demonstrates that long-term dietary exposure to Ag-TiO_2 nanoparticles induces clear dose-dependent effects on the growth performance and survival of *Etroplus suratensis* fingerlings. Intermediate dietary concentrations (1 and 10 mg kg^{-1}) significantly enhanced growth indices, including percentage weight gain and final biomass, while maintaining low mortality, indicating a stimulatory or hormetic response at low exposure levels. In contrast, higher concentrations (100 and 1000 mg kg^{-1}) markedly impaired growth and increased mortality, with the highest dose producing the most pronounced adverse effects.

Statistical and multivariate analyses (ANOVA, Pearson correlation, PCA, and hierarchical clustering) consistently distinguished treatments into two major response groups: low-dose treatments associated with optimal growth and survival, and high-dose treatments associated with reduced growth performance and elevated mortality. The strong positive correlation between weight gain and biomass, coupled with their negative association with mortality, highlights the trade-off between growth and survival under increasing nanoparticle stress.

Overall, the findings indicate that E. *suratensis* is highly sensitive to dietary Ag-TiO_2 nanoparticle exposure and can serve as an effective bioindicator for nanoparticle-induced toxicity in aquatic ecosystems. The observed growth inhibition and increased mortality at elevated concentrations raise concerns regarding the ecological risks of uncontrolled nanoparticle discharge into aquatic environments. These results emphasize the need for regulatory guidelines and sustainable management strategies to minimize nanoparticle contamination and protect aquatic biodiversity.

Conflict of Interest

The authors declare no conflict of interest.

References

1. T. Kotil, C. Akbulut, and N.D. Yön. The effects of titanium dioxide nanoparticles on ultrastructure of zebrafish testis (Danio rerio). *Micron*, 2017, *100*, 38.
2. I. Khan, K. Saeed, and I. Khan. Nanoparticles: Properties, applications and toxicities. *Arabian Journal of Chemistry*, **2019**, *12*, 908.
3. A. Matet, et al., *Retinal and choroidal cancers: Blood-retinal barriers considerations in ocular chemotherapy*, in *Drug Efflux Pumps in Cancer Resistance Pathways: From Molecular Recognition and Characterization to Possible Inhibition Strategies in Chemotherapy*. **2020**, Elsevier. p. 303.
4. C. Mesak, et al. The effects of predicted environmentally relevant concentrations of ZnO nanoparticles on the behavior of Gallus gallus domesticus (Phasianidae) chicks. *Environmental Pollution*, **2018**, *242*, 1274.
5. S. Mohammadbakir, *Impacts of waterborne copper and silver on the early life stage (ELS) of zebrafish (Danio rerio): Physiological, biochemical and molecular responses* **2016**, University of Plymouth: UK.
6. J. Palanichamy, et al. Water quality parameters as indicators to study the interactions of nanoparticles in an aqueous environment. *Environmental Nanotechnology, Monitoring & Management*, **2020**, *14*, 100329.
7. K. Danielsson, et al. Influence of organic molecules on the aggregation of TiO2 nanoparticles in acidic conditions. *Journal of Nanoparticle Research*, **2017**, *19*.
8. A. Juárez-Maldonado, et al. Biostimulation and toxicity: The magnitude of the impact of nanomaterials in microorganisms and plants. *Journal of Advanced Research*, **2021**, *31*, 113.

© 2026 Authors. The authors retain copyright and full publishing rights under a CC BY 4.0 International License.

9. G. Libralato, et al. A review of toxicity testing protocols and endpoints with Artemia spp. *Ecological Indicators*, **2016**, *69*, 35.

10. M. Pockberger, et al. An abundant small sized fish as keystone species? The effect of Pomatoschistus microps on food webs and its trophic role in two intertidal benthic communities: A modeling approach. *Journal of Sea Research*, **2014**, *86*, 86.

11. C.S. Ramsden, et al. Dietary exposure to titanium dioxide nanoparticles in rainbow trout, (Oncorhynchus mykiss): no effect on growth, but subtle biochemical disturbances in the brain. *Ecotoxicology*, **2009**, *18*, 939.

12. Z. Clemente, et al. Toxicity assessment of TiO2 nanoparticles in zebrafish embryos under different exposure conditions. *Aquatic Toxicology*, **2014**, *147*, 129.

13. L. Bameri, et al. Toxicity of TiO2 nanoparticles to the marine microalga Chaetoceros muelleri Lemmermann, 1898 under long-term exposure. *Environmental Science and Pollution Research*, **2022**, *29*, 30427.

14. A. Al-Ammari, et al. Toxicity assessment of synthesized titanium dioxide nanoparticles in fresh water algae Chlorella pyrenoidosa and a zebrafish liver cell line. *Ecotoxicology and Environmental Safety*, **2021**, *211*, 111948.

15. E. Baranowska-Wójcik, et al. Effects of Titanium Dioxide Nanoparticles Exposure on Human Health—a Review. *Biological Trace Element Research*, **2019**, *193*, 118.

16. D.B. Warheit and E.M. Donner. Risk assessment strategies for nanoscale and fine-sized titanium dioxide particles: Recognizing hazard and exposure issues. *Food and Chemical Toxicology*, **2015**, *85*, 138.

17. R. van Aerle, et al. Molecular Mechanisms of Toxicity of Silver Nanoparticles in Zebrafish Embryos. *Environmental Science & Technology*, **2013**, *47*, 8005.

18. M. Banaee, et al. Blood biochemical changes in common carp (Cyprinus carpio) upon co-exposure to titanium dioxide nanoparticles and paraquat. *Iranian Journal of Fisheries Sciences*, **2019**, *18*, 242.

19. L.L. Dong, et al. Effects of TiO₂ nanoparticles on the life-table parameters, antioxidant indices, and swimming speed of the freshwater rotifer Brachionus calyciflorus. *Journal of Experimental Zoology Part A: Ecological and Integrative Physiology*, **2020**, *333*, 230.

20. X. Huang, et al. Salinity mediates the toxic effect of nano-TiO2 on the juvenile olive flounder Paralichthys olivaceus. *Science of The Total Environment*, **2018**, *640-641*, 726.

21. R. Zeumer, et al. Chronic effects of wastewater-borne silver and titanium dioxide nanoparticles on the rainbow trout (Oncorhynchus mykiss). *Science of The Total Environment*, **2020**, *723*, 137974.

22. H. Faiz, et al. Zinc Oxide, Zinc Sulfate and Zinc Oxide Nanoparticles as Source of Dietary Zinc: Comparative Effects on Growth and Hematological Indices of Juvenile Grass Carp (Ctenopharyngodon idella). *International Journal of Agriculture and Biology*, **2015**, *17*, 568.

23. C. Leite, et al. Toxic impacts of rutile titanium dioxide in Mytilus galloprovincialis exposed to warming conditions. *Chemosphere*, **2020**, *252*, 126563.

24. B.D. Johnston, et al. Bioavailability of Nanoscale Metal Oxides TiO₂, CeO₂, and ZnO to Fish. *Environmental Science & Technology*, **2010**, *44*, 1144.

25. S. Hu, et al. Impact of co-exposure to titanium dioxide nanoparticles and Pb on zebrafish embryos. *Chemosphere*, **2019**, *233*, 579.

26. T. Tang, Z. Zhang, and X. Zhu. Toxic Effects of TiO2 NPs on Zebrafish. *International Journal of Environmental Research and Public Health*, **2019**, *16*, 523.

27. G. Sahu, et al. Variations in community structure of phytoplankton in relation to physicochemical properties of coastal waters, southeast coast of India. *Indian journal of geo-marine sciences*, **2012**, *41*, 223.

28. M.S. Achary, et al. Nutrient dynamics and seasonal variation of phytoplankton assemblages in the coastal waters of southwest Bay of Bengal. *Environmental Monitoring and Assessment*, **2014**, *186*, 5681.

29. M. Hagens and J.J. Middelburg. Attributing seasonal pH variability in surface ocean waters to governing factors. *Geophysical Research Letters*, **2016**, *43*.

30. M.D. Bharathi, et al. Seasonal variability in plankton food web composition in Tuticorin coastal waters, south east coast of India. *Marine Pollution Bulletin*, **2018**, *137*, 408.

31. C. Granier, et al. The impact of natural and anthropogenic hydrocarbons on the tropospheric budget of carbon monoxide. *Atmospheric Environment*, **2000**, *34*, 5255.

32. P.N. Vinayachandran and T. Yamagata. Comment on "Indian Ocean: Validation of the Miami Isopycnic Coordinate Ocean Model and ENSO events during 1958–1998" by V. E. Haugen et al. *Journal of Geophysical Research: Oceans*, **2003**, *108*.

33. J. Sospedra, et al. Identifying the main sources of silicate in coastal waters of the Southern Gulf of Valencia (Western Mediterranean Sea). *Oceanologia*, **2018**, *60*, 52.

34. R.C. Dugdale, et al. The role of ammonium and nitrate in spring bloom development in San Francisco Bay. *Estuarine, Coastal and Shelf Science*, **2007**, *73*, 17.

35. K.K. Satpathy, et al. Spatio-temporal variation in physicochemical properties of coastal waters off Kalpakkam, southeast coast of India, during summer, pre-monsoon and

© 2026 Authors. The authors retain copyright and full publishing rights under a CC BY 4.0 International License.

post-monsoon period. *Environmental Monitoring and Assessment*, **2010**, *180*, 41.

36. R.G. Zepp. Interactions of marine biogeochemical cycles and the photodegradation of dissolved organic carbon and dissolved organic nitrogen. *Marine Chemistry*, **1997**, *25*, 329.

37. M. Saito, et al. Nitrogen dynamics in a highly urbanized coastal area of western Japan: impact of sewage-derived loads. *Progress in Earth and Planetary Science*, **2018**, *5*, 17.

38. S.M. Liu. Response of nutrient transports to water–sediment regulation events in the Huanghe basin and its impact on the biogeochemistry of the Bohai. *Journal of Marine Systems*, **2015**, *141*, 59.

39. T.L.L. do Carmo, et al. Reactive oxygen species and other biochemical and morphological biomarkers in the gills and kidneys of the Neotropical freshwater fish, Prochilodus lineatus, exposed to titanium dioxide (TiO2) nanoparticles. *Environmental Science and Pollution Research*, **2018**, *25*, 22963.

40. D. Xiong, et al. Effects of nano-scale TiO2, ZnO and their bulk counterparts on zebrafish: Acute toxicity, oxidative stress and oxidative damage. *Science of The Total Environment*, **2011**, *409*, 1444.

41. M.S. Diniz, et al. Liver Alterations in Two Freshwater Fish Species (Carassius auratus and Danio rerio) Following Exposure to Different TiO2 Nanoparticle Concentrations. *Microscopy and Microanalysis*, **2013**, *19*, 1131.

42. P.V. Vidya and K.C. Chitra. Assessment of acute toxicity (LC50-96 h) of aluminium oxide, silicon dioxide and titanium dioxide nanoparticles on the freshwater fish, Oreochromis mossambicus (Peters, 1852). *International journal of fisheries and aquatic studies*, **2017**, *5*, 327.

43. J. Chen, et al. Effects of titanium dioxide nano-particles on growth and some histological parameters of zebrafish (Danio rerio) after a long-term exposure. *Aquatic Toxicology*, **2011**, *101*, 493.

44. H. Liu, et al. Effects of dietary yeast culture supplementation on growth, intestinal morphology, immunity, and disease resistance in Epinephelus fuscoguttatus♀× Epinephelus lanceolatu♂. *Journal of Guangdong Ocean University*, **2021**, *41*, 1.

45. H. Liu, et al. Negative effects of aflatoxin B1 (AFB1) in the diet on growth performance, protein and lipid metabolism, and liver health of juvenile hybrid grouper (Epinephelus fuscoguttatus♀×Epinephelus lanceolatus♂). *Aquaculture Reports*, **2023**, *33*, 101779.

46. Z.F. Lu, et al. Effects of hypoxic stress on antioxidant and energy metabolism of hybrid grouper (Epinephelus fuscoguttatus♀× Epinephelus lanceolatus♂). *Journal of Guangdong Ocean University*, **2022**, *42*, 13.

47. K.U. Sheethal, et al. Individual and combined acute toxicity of nanoparticles exposed to brackish water fish pearl spot (Etroplus suratensis). *Biochemical and Cellular Archives*, **2023**, *23*, 1113.

48. P. Kumar, et al. Assessment of potential human health risk due to heavy metal contamination in edible finfish and shellfish collected around Ennore coast, India. *Environmental Science and Pollution Research*, **2020**, *28*, 8151.

49. K. Pandion, et al. Health risk assessment of heavy metals in the seafood at Kalpakkam coast, Southeast Bay of Bengal. *Marine Pollution Bulletin*, **2023**, *189*, 114766.

50. K.D. Arunachalam. Heavy Metals Intake Due to Consumption of Food sources in Duplicate Diet Sampling (DDS) Methods used by Coastal Inhabitants around the Nuclear Power Plants. *American Journal of Biomedical Science & Research*, **2025**, *26*, 138.

51. K. Pandion, et al. Potential health risk caused by heavy metal associated with seafood consumption around coastal area. *Environmental Pollution*, **2022**, *294*, 118553.

52. R.R. Miranda, et al. Effects of realistic concentrations of TiO2 and ZnO nanoparticles in Prochilodus lineatus juvenile fish. *Environmental Science and Pollution Research*, **2015**, *23*, 5179.

53. D. Wang, et al. Quantitative Analysis of Reactive Oxygen Species Photogenerated on Metal Oxide Nanoparticles and Their Bacteria Toxicity: The Role of Superoxide Radicals. *Environmental Science & Technology*, **2017**, *51*, 10137.

54. S. Pan, et al. The positive effects of dietary inositol on juvenile hybrid grouper (♀ Epinephelus fuscoguttatus × ♂ E. lanceolatu) fed high-lipid diets: Growthperformance, antioxidant capacity and immunity. *Fish & Shellfish Immunology*, **2022**, *126*, 84.

55. E.M. Scalisi, et al. Titanium Dioxide Nanoparticles: Effects on Development and Male Reproductive System. *Nanomaterials*, **2023**, *13*, 1783.

© 2026 Authors. The authors retain the copyright and full publishing rights. This article is licensed under a Creative Commons Attribution 4.0 BY International License.

© 2026 Authors. The authors retain copyright and full publishing rights under a CC BY 4.0 International License.

Evaluation of Urease Activity Assessed on Urea Concentration Using Tannic Acid-Silver Nitrate Colorimetric Method

Ojeaga Imohiosen *, Adamu Makanta Salihu, Matthew Onyema Agu, Sanusi Abubakar

Editor's note: Urease, a nickel-dependent enzyme, hydrolyzes urea into ammonia and carbon dioxide. Imohiosen et al. explored how urea concentration affects urease activity using a colorimetric method with tannic acid and silver nitrate. Low concentrations (≤ 1.00 mM) limited enzyme activity, while an optimal concentration of 3.00 mM produced the highest absorbance (0.949), indicating maximum activity. Concentrations above 4.00 mM decreased absorbance, likely due to pH shifts. Low urea levels showed sharp SPR peaks at 414 nM, whereas higher levels produced broader peaks, suggesting substrate inhibition. These findings support the development of a sensitive urea biosensor.

doi: 10.22034/jams.2026.260107

How to cite: O. Imohiosen et al., *Journal of Applied Material Science*, **2026**, *2*, 260107.

JOURNAL OF
APPLIED
MATERIAL
SCIENCE
jams.hsu.ac.ir

© 2026 *J. Appl. Mater. Sci.* This material is licensed under a Creative Commons Attribution 4.0 International License.

Journal of Applied Material Science **2026**, 2, 260107
How to cite: O. Imohiosen et al., *Journal of Applied Material Science*, **2026**, 2, 260107.
Journal homepage: **jams.hsu.ac.ir**

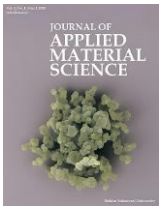

Original Research

Evaluation of Urease Activity Assessed on Urea Concentration Using Tannic Acid-Silver Nitrate Colorimetric Method

Ojeaga Imohiosen [a,b,*], Adamu Makanta Salihu [c], Matthew Onyema Agu [d], Sanusi Abubakar [b]

[a] *Department of Chemistry & Biochemistry, School of Engineering and Science, Sharda University, India*

[b] *Department of Science Laboratory Technology, The Federal Polytechnic Bali, Bali, Taraba State. Nigeria*

[c] *Department of Chemistry, School of Physical Sciences, Federal University of Technology, Minna, Nigeria*

[d] *Department of Pure and Industrial Chemistry, Nnamdi Azikiwe University, Awka, Anambra State, Nigeria*

Abstract

Urease, a nickel-dependent enzyme, hydrolyses urea into ammonia and carbon dioxide. The unhydrolyzed urea, in the presence of silver nitrate and tannic acid, forms a yellow-brown complex. This study examines the effect of urea concentration on urease activity using a colorimetric method that involves tannic acid and silver nitrate. The results revealed that low concentrations of urea, less than or equal to 1.00 mM, may limit substrate availability, leading to an underestimation of enzyme activity. An optimal urea concentration of 3.00 mM produced the highest absorbance, 0.949, indicating maximal urease activity (V_{max}). The high urea concentrations, greater than or equal to 4.00 mM, resulted in lower absorbance, possibly due to pH shifts or altered reaction kinetics. Low urea concentrations show narrow or sharp SPR peaks at around 414 nM, whereas higher concentrations display broader or wider peaks. The Lineweaver-Burk method shows that the enzyme kinetics of the urea hydrolysis efficiency were greatest at about 3 mM. At this concentration, catalytic efficiency and enzyme/substrate binding were very high (i.e., low Km and near-saturation V_{max}). Higher substrate concentrations led to decreased reaction rates. The changing wavelengths suggested substrate inhibition and possible sensor behavior related to nanoparticles. These results indicate that this approach is viable for a very sensitive urea biosensor.

Keywords: Urea; Tannic acid; Silver nitrate; Colorimetric method.

* Corresponding author.
Email address: 2024855950.ojeaga@pg.sharda.ac.in (O. Imohiosen)

Received 20 December 2025
Revised 3 February 2026
Accepted 10 February 2026
Available online 13 February 2026

https://doi.org/10.22034/jams.2026.260107
© 2026 Authors. The authors retain copyright and full publishing rights under a CC BY 4.0 International License.

1. Introduction

Metal nanoparticles like AgNPs have drawn significant attention owing to their unique physicochemical properties, which make them highly applicable in environmental remediation, medicine, agriculture, and more [1]. Silver nanoparticles green synthesis, which exploits biological agents such as plant extracts, microbes, and biomolecules, has arisen as an ecological and eco-friendly alternative to physical synthesis and conventional chemical methods. This approach not only decreases environmental impact but also ensures the production of biocompatible nanoparticles with enhanced biological activities [2].

Urease-based biosensors are usually used to sense urea in biological and environmental samples. This could consist of using urease to catalyze the breakdown of urea, with the products being determined to infer the concentration of urea. Silver nitrate ($AgNO_3$) could be used in these sensors to examine the ions present or to modify surfaces, making the sensor more sensitive. Urea can be hydrolyzed via a catalytic enzyme, urease, into ammonia and carbon dioxide. It is vital in several biological processes and is also used in diagnostic tests [3-5]. To maintain biochemical reactions of stable pH, a phosphate buffer (PB) is used. This is vital, since most enzyme activity, like that of urease, highly depends on pH [6]. Urea is a substrate for the urease enzymes, whose concentration is often measured in various applications. Tannic acid, a polyphenol, acts as a reducing agent. It interacts with enzymes such as urease, potentially inhibiting their activity, and is also used to produce silver nanoparticles [7]. Silver nitrate is a source of silver ions, and in the presence of tannic acid, a reducing agent, the silver ions are reduced to silver nanoparticles (AgNPs). Color change shows the presence or concentration of the target substances. Hence, these AgNPs can be used in colorimetric assays [8].

Even though colorimetric assays based on silver tannic acid complexation have proven extremely common for determining urease activity, little is known about the effects of substrate concentration on assay accuracy and signal linearity. Specifically, the impact of urea concentration on absorbance response, SPR peak behavior, and signal distortion that might have been a result of pH- or kinetics-induced changes has not been systematically considered. Such inefficiency can be the cause of under- or overestimating urease activity, which shows the necessity of well-defined operating conditions to perform an accurate enzymatic measurement.

Colorimetric urea sensing involves measuring urea content based on a visible color change, usually through an enzyme or chemical reaction. The enzyme urease, responsible for the hydrolysis of urea into ammonia and carbon dioxide, forms the basis for a highly sought-after colorimetric urea sensing method. The pH indicator can, as ammonia produced changes the pH of the solution, change color. Urease-mediated colorimetric sensing: In one investigation, it was demonstrated that urease was used to catalyze the hydrolysis of urea. The presence of urea was signaled by a yellow-to-red color change when a pH-sensitive dye, i.e., phenol red, was used. This method provides a rapid and effective method to detect urea in environmental samples and biofluids.

With the help of a pH indicator, the presence of urea can lead to a pH change when it reacts with urease and alters the color. Phenol red is a common pH indicator used in this way; its color shifts depending on the basicity or acidity of the solution. Phenol red-based colorimetric sensor: This system employs phenol red that changes from yellow (acidic) to red (basic) in the presence of released ammonia through urea hydrolysis. The intensity of the color change varies directly with the concentration of urea.

Surface Plasma Resonance (SPR) is based on the collective oscillation of conduction electrons at the surface of metallic nanoparticles (like silver) when excited by light. This SPR peak appears in the UV/Vis spectrum and is highly sensitive to the following factors: shape and particle size, interparticle spacing, and Dielectric environment (such as pH and solvent) [9].

Nanoparticles with a smaller size, SPR normally happens at blue-shift (shorter wavelength) due to stronger absorption and less scattering. For particles with a larger size, SPR shifts to longer wavelengths (red-shift) and also shows a broader SPR peak, due to greater scattering and multipolar modes. It may also display multiple resonance modes (e.g., dipolar, quadrupolar). The widening and broadening of the SPR peak are symbols of clustering or polydispersity in the size of nanoparticles, aggregation, which is due to pH-induced instability and complex shapes or large particle dimensions (e.g., rods, stars) [9]. This study aimed to examine the evaluation of colorimetric sensing of urea concentrations via the tannic acid-silver nitrate method.

© 2026 Authors. The authors retain copyright and full publishing rights under a CC BY 4.0 International License.

2. Experimental

2.1. Materials

Analytical-grade reagents were used in this study. Urease (AR grade), urea (99% AR grade), phosphate buffer (AR grade pH 7.0), tannic acid AR (gallotannic acid), $AgNO_3$ (AR grade) were used as synthesis starting materials.

2.2. Measurements

Urease Incubation: Urease enzyme (50 µL, 5 µ/mL) in 0.5 mM of PB (phosphate buffer) solution is incubated with 50 µL of various urea concentrations (0.00, 1.00, 2.00, 3.00, 4.00, 5.00, and 10.00 mM) individually for 10 min at 37 ± 1 °C in a water bath/ incubator [10-12].

Sensing Solution Addition: Subsequently, the sensing solution consisting of 800 µL of tannic acid (0.025 mg/mL) and 100 µL of $AgNO_3$ (15 mM) was added to the aforementioned solution and incubated for another 20 mins [10-12].

Spectrophotometric Measurement: The intensity of the color change is measured spectrophotometrically in a wavelength range of 300 – 600 nM. UV-Vis Spectroscopy, this technique is used to confirm the formation of AgNPs by detecting the surface plasmon resonance (SPR) peak, typically in the range of 400-450 nm [10-12].

3. Results and discussion

In Table 1, as the concentration of urea increases from 1.00 mM, 2.00 mM, and 3.00 mM, the absorbances are 0.902, 0.877, and 0.949, respectively. Optimal urea concentration, 3.00 mM (typically saturating). 3.00 mM has the highest absorbance of 0.949, which is the optimal urea concentration (typically saturating). This means its maximum capacity, which the enzyme is working, hence allowing for an accurate measurement of its activity (V_{max}).

In Figure 1, the too low urea concentration, 1.00 mM, leads to substrate limitation where the measured activity reflects the availability of urea rather than the enzyme's intrinsic activity. It may also result in color development that is too faint to be accurately quantified.

In Figure 1, the high urea concentrations of 4.00 mM, 5.00 mM, and 10.00 mM prolonged reaction may lead to important product inhibition by ammonia, altering the reaction kinetics and potentially imparting the colorimetric signal. It may also cause large pH shifts that can move the enzyme out of its optimal activity range. A

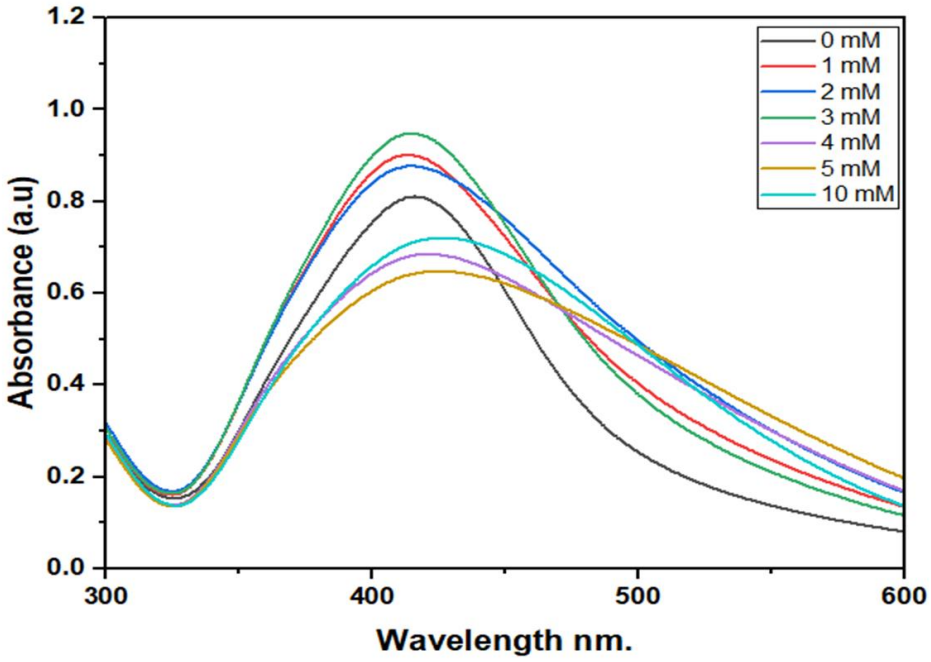

Figure 1. Graph of different urea concentrations wavelength (nM) against absorbance.

© 2026 Authors. The authors retain copyright and full publishing rights under a CC BY 4.0 International License.

Table 1. UV/Vis results of urea concentration (mM), absorbance, and wavelength (nM)

Urea Conc. (mM)	Absorbance	Wavelength (nM)	Remark
0.00	0.811	415.0	
1.00	0.902	414.0	Too low
2.00	0.877	414.0	Low
3.00	0.949	414.0	Optimal (TS)
4.00	0.684	424.0	High
5.00	0.648	423.0	High
10.0	0.721	425.0	excessively high

Note: TS = typically saturating

higher urea concentration will result in more ammonia production, leading to more tannic acid reduction and a greater number of silver nanoparticles, thus causing a more pronounced color change.

According to [13, 14], moderate, high, and very high urea concentrations of 4 M, greater than 6 M, and greater than 8 M, respectively. 4 M show a minor red-shift, slightly broadening SPR peaks, and a gradual increase in pH. With a minor increase in particle size with moderate aggregation, urea starts to change its hydration shell and surface interactions. High urea concentration greater than 6 M shows broadening SPR peaks, red-shift, and a major increase in pH through hydrolysis. Apparent increase in particle size with high aggregation, urease-catalyzed hydrolysis produces NH_3, promoting aggregation and altering pH. Very high urea concentration, greater than 8 M, shows a non-linear shift, strong broadening of the SPR peaks, and alkaline pH. Clustering of particle size, very high aggregation, urea self-aggregation, and strength effects dominate; destabilization of colloids.

Curves for 1.00 mM, 2.00 mM, and 3.00 mM exhibit sharp absorption peaks, generally located at approximately 414 nM, which agrees with the work of [10, 11] that says the surface plasmon resonance (SPR) peak of AgNPs formation is detected in the range of 400-450 nm. According to [10, 11, 15], the SPR peak is characteristic of Surface Plasmon Resonance (SPR) for silver nanoparticles, which range between 400 nM and 430 nM. Hence, the urea concentrations of 4.00 mM, 5.00 mM, and 10.00 mM curves exhibit broad absorption peaks [12].

The colorimetric assay method based on urease may be utilized in daily situations when it is necessary to quickly test urea levels in farm soils and fertilizers to control the appropriate amount of nitrogen, and when screening blood or food items, to quickly determine the presence of disproportional urea concentrations by using straightforward color responses. Maximization of urea concentration guarantees precise, inexpensive monitoring without advanced instrumentation; it is applicable in the field or in the laboratory in regular usage [16, 17].

Table 2 and Figure 2, The Lineweaver–Burk diagram illustrates the reciprocal link between the concentration of the substrate (1/[S]) and velocity of the reaction (1/V), resulting in a linear graph with a bracket system where the kinetic values for an enzyme can be assessed. This linear equation approximating the line shown in the plot can be expressed as: $1/V = - 0.405 (1/[S]) + 1.444$. The V_{max} (Maximum Reaction Velocity) is represented by the value of the y intercept: $1/V_{max} = 1.444$. Hence, Vmax = 0.693 a.u. The data imply a maximum catalysis of approximately 0.693 at saturation of enzyme active sites.

An enzyme's kinetic behavior is inversely proportional to concentration based on the slope of the Lineweaver-Burk Plot Curve, providing the distinguishing characteristic of enzyme kinetics. With a relatively low Vmax, the enzyme can likely operate at moderate catalytic efficiency.

Using the Lineweaver-Burk approach, the common approach of linearizing Michaelis-Menten kinetics was utilized, allowing us to determine important characteristics of the enzyme-catalyzed reaction. The behavior of the enzyme as it hydrolyses urea fits a normal saturation curve, where the amount of product produced is dependent on the amount of substrate available until all catalytic sites are filled with substrate [18]. The value of Vmax is an estimate of the maximum catalytic effectiveness of the enzyme, and since the Km

Table 2. Calculated reciprocal values for Lineweaver–Burk plot

[S] (mM)	V (Absorbance)	1/[S] (mM^{-1})	1/V
1.00	0.902	1.000	1.109
2.00	0.877	0.500	1.140
3.00	0.949	0.333	1.054
4.00	0.684	0.250	1.462
5.00	0.648	0.200	1.543
10.0	0.721	0.100	1.387

Note: V = Reaction velocity (represented by absorbance), [S] = Substrate concentration (urea, mM), Km = Michaelis constant, Vmax = Maximum reaction velocity. (The 0 mM concentration was excluded because reciprocal substrate concentration is undefined).

© 2026 Authors. The authors retain copyright and full publishing rights under a CC BY 4.0 International License.

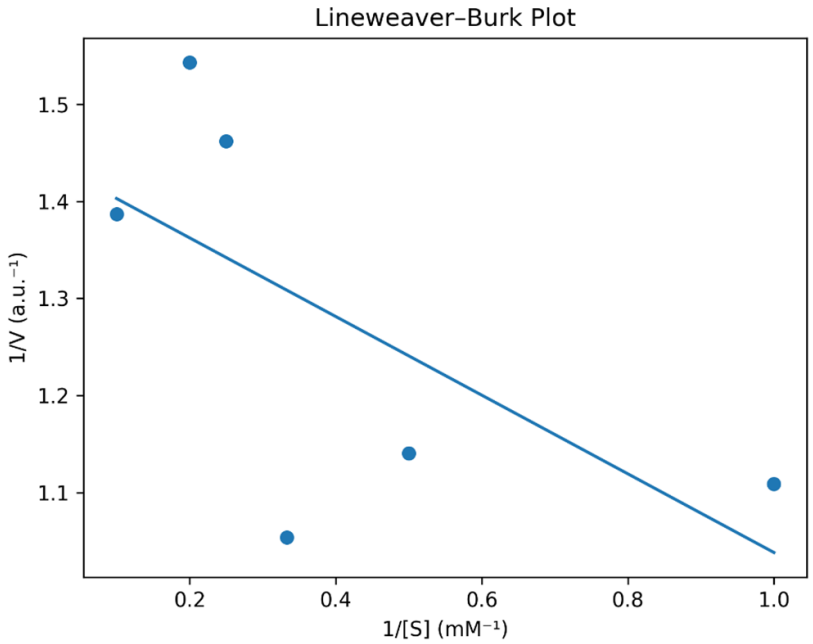

Figure 2. Lineweaver–Burk plot analysis for enzyme kinetics.

value (the amount of substrate needed for half-maximal activity at saturation) is low, it indicates a very high level of enzyme-substrate affinity and catalytic efficiency, making it a good candidate for use in analytical or biosensing applications. Additionally, reactions at higher levels of substrate are inhibited, inhibiting the rate of reaction at the very high levels (100 µM), indicating either inhibition by substrate or conformational changes of the enzyme. Moreover, upon addition of high substrate levels, a shift in the wavelength of the absorption spectrum is observed, suggesting that reactions may occur in an altered environment due to the use of the amplitude changes seen in the colorimetric sensing behavior of nanoparticle-based systems. Thus, the enzyme system exhibits good catalytic performance and high potential for the development of ultra-sensitive urea detection systems.

4. Conclusions

A yellow-brown complex is formed by the unhydrolyzed urea in the presence of silver nitrate and tannic acid. Urea concentrations of 1.00 mM, 2.00 mM, and 3.00 mM have absorbance values of 0.902, 0.877, and 0.949, respectively. Concentrations less than or equal to 1.00 mM may limit substrate availability, leading to underestimation of enzyme activity. The optimal concentration, 3.00 mM, has the highest absorbance, 0.949, indicating maximal urease activity (Vmax). High concentrations of 4.00 mM, 5.00 mM, and 10.00 mM have absorbance values of 0.684, 0.648, and 0.721, respectively. The concentrations, greater than or equal to 4.00 mM, resulted in lower absorbance, possibly due to pH shifts or altered reaction kinetics. Urea with low concentrations shows narrow or sharp SPR peaks around 414 nM, while higher concentrations display broader or wider peaks. The widening and broadening of the SPR peak are symbols of clustering or polydispersity in the size of nanoparticles, aggregation, which is due to pH-induced instability and complex shapes or large particle dimensions (e.g., rods, stars). A typically saturating (optimal) urea concentration is crucial for accurately assessing urease activity, which reflects its catalytic competence and falls within the linear range of the detection method. The Lineweaver-Burk graph was efficient for quantifying kinetic parameters. The enzyme had high substrate affinity (low Km) and a clear maximum reaction rate. This confirmed that the experimental assay was accurate for analytical enzyme activity studies and biosensing.

© 2026 Authors. The authors retain copyright and full publishing rights under a CC BY 4.0 International License.

Conflict of Interest

The authors declare no conflict of interest.

References

1. 1. F. Lasmi, et al. Silver Nanoparticles (AgNPs), Methods of Synthesis, Characterization, and Their Application: A Review. *Plasmonics*, **2025**, *20*, 9455.
2. A. Rónavári, et al. Green Silver and Gold Nanoparticles: Biological Synthesis Approaches and Potentials for Biomedical Applications. *Molecules*, **2021**, *26*, 844.
3. G.I. Likhtenshtein, *Methods of Analysis in Enzyme Processes*, in *Enzyme Catalysis Today and the Chemistry of the 21st Century*. **2025**, Springer Nature Switzerland. p. 43.
4. T.S.M. Taha, et al., *Urease Nickel Metallocenter: Structure and Assembly*, in *Transition Metals in Microbial Metabolism*. **2022**, CRC Press. p. 391.
5. M.-J. Cui, et al. A quantitative, high-throughput urease activity assay for comparison and rapid screening of ureolytic bacteria. *Environmental Research*, **2022**, *208*, 112738.
6. S. Rai, et al. Ameliorating enzyme functionality with temperature and pH responsive polymer interface. *Journal of Polymer Research*, **2024**, *32*, 1.
7. A.M. Michael and M.N. Malash. A Validated Assay of Urease Enzyme in Different Sources Using Silver Nanoparticles. *Food Analytical Methods*, **2015**, *8*, 2482.
8. T.T. Bezuneh, et al. Tannic Acid-Functionalized Silver Nanoparticles as Colorimetric Probe for the Simultaneous and Sensitive Detection of Aluminum(III) and Fluoride Ions. *ACS Omega*, **2023**, *8*, 37293.
9. P.A. Van Der Merwe, *Surface plasmon resonance*, in *Protein-Ligand Interactions: hydrodynamics and calorimetry*. **2000**, Oxford University PressOxford. p. 137.
10. P. Dayma, et al. Exploring the Potential of Halotolerant Actinomycetes from Rann of Kutch, India: A Study on the Synthesis, Characterization, and Biomedical Applications of Silver Nanoparticles. *Pharmaceuticals*, **2024**, *17*, 743.
11. E. Abada, et al. Review green synthesis of silver nanoparticles by using plant extracts and their antimicrobial activity. *Saudi Journal of Biological Sciences*, **2024**, *31*, 103877.
12. M. Ismail. Spectrophotometric and Spectrofluorimetric Quantification of Urea via Silver Nanoparticles Prepared by Wet Chemical Method. *Catalysis Research*, **2023**, *03*, 1.
13. M.C. Stumpe and H. Grubmüller. Aqueous Urea Solutions: Structure, Energetics, and Urea Aggregation. *The Journal of Physical Chemistry B*, **2007**, *111*, 6220.
14. P. Nalini and R.S. Prakasham. Novel, Effective and Sensitive Plate Assay Method for Detection and Screening of Urease Producing Microorganisms. *International Journal of Current Microbiology and Applied Sciences*, **2022**, *11*, 81.
15. A. Liang, et al. A novel and sensitive resonance scattering assay for detection of urea in serum coupled urease catalytic reaction and NH4 + associated particle reaction. *Bioprocess and Biosystems Engineering*, **2011**, *34*, 639.
16. R. Abbas, et al. Silver Nanoparticles: Synthesis, Structure, Properties and Applications. *Nanomaterials*, **2024**, *14*, 1425.
17. J. Bzura, D. Korsak, and R. Koncki. Bioanalytical insight into the life of microbial populations: A chemical monitoring of ureolytic bacteria growth. *Enzyme and Microbial Technology*, **2022**, *153*, 109899.
18. A. Cornish-Bowden, *Introduction to enzyme kinetics*, in *Fundamentals of Enzyme Kinetics*. **1979**, Elsevier. p. 16.

© 2026 Authors. The authors retain the copyright and full publishing rights. This article is licensed under a Creative Commons Attribution 4.0 BY International License.

© 2026 Authors. The authors retain copyright and full publishing rights under a CC BY 4.0 International License.